Studies Of Post-AGB Stars And Proto-planetary Nebulae

A Thesis
submitted for the degree of
DOCTOR OF PHILOSOPHY

In
The Faculty Of Science

Bangalore University
Bangalore

By
ESWAR REDDY B

Indian Institute Of Astrophysics
Bangalore 560 034, India

August 1996

Declaration

I hearby declare that the matter contained in this thesis is the result of the investigations carried out by me at the Indian Institute of Astrophysics, Bangalore, under the supervision of Prof. M. Parthasarathy. This work has not been submitted for the award of any degree, diploma, associateship, fellowship, etc, of any university or institute.
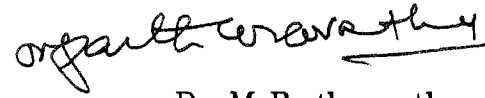
B.Eswar Reddy

(Ph.D candidate)

Bangalore - 560034
1996 August 08

Certificate

This is to certify that the thesis entitled 'Studies of Post-AGB stars and Proto-Planetary nebulae' submitted to the Bangalore University by Mr. B. Eswar Reddy for the award of the degree of Doctor of Philosophy in the faculty of Science, is based on the results of the investigations carried out by him under my supervision and guidance, at the Indian Institute of Astrophysics. This thesis has not been submitted for the award of any degree, diploma, associate-ship, fellowship, etc. of any university or institute.

Dr. M. Parthasarathy

(Supervisor)

Bangalore 560034
1996 August

ACKNOWLEDGMENTS

Summary

The stellar evolutionary phase between AGB and PN (Post-AGB/PPN phase) is not well understood. Only recently it is becoming possible through IRAS data to recognize stars which may be in the post-AGB phase. In this thesis, we study post-AGB stars in two folds: one is identifying new post-AGB stars based on their spectral energy distribution and other is study of photospheric chemical composition of few newly identified post-AGB candidates to confirm their evolutionary status. Our chemical abundance analysis is based on high resolution spectra obtained with 2.1 m telescope at McDonald Observatory and Issac Newton Telescope (INT) at La Palma. We also use medium resolution spectra obtained from Vainu Bappu Telescope (VBT), at Vainu Bappu Observatory (VBO). The chemical abundance analysis presented in this thesis will help in further understanding of stellar structure and evolution and in particular chemical evolution in the late stages of stellar evolution.

In chapter 1, we give a general introduction to the subject. The evolution of low- and intermediate- mass stars is briefly outlined. We also present the chemical abundance patterns at different phases of stellar evolution. We discuss observational properties of post-AGB stars and various groups of post-AGB stars. We give an overview of the available chemical composition of post-AGB stars.

In chapter 2, we investigate a sample of IRAS sources which have far-IR colours similar to PNe and post-AGB stars. We present CCD imaging and BVRI photometry. We discuss the observed flux distribution of these sources from 0.4 μm to 100 μm. From their spectral energy distribution, we find stars which have only cold dust component and stars which have both cold and hot dust components. We also present the results of low resolution optical and near-IR spectra of these sources. Stellar and

i

dust envelope parameters are derived using simple model. These results suggest that most of the IRAS sources considered here are associated with post-AGB supergiants.

High resolution optical spectroscopic observations program is outlined in chapter 3. This chapter contains a brief description of spectroscopic reduction procedure using Image Reduction and Analysis Facility (IRAF). We also discuss in brief the computer CODES and stellar model atmospheres involved in chemical composition analysis. We discuss in general the various methods involved in determining atmospheric parameters: effective temperature (T_{eff}), surface gravity (log g), microturbulence (ξ_t) and metallicity. This chapter also contains, a brief description of post-AGB candidates which are chosen for chemical composition analysis.

In chapter 4, for the first time we present the chemical composition analysis of a post-AGB candidate IRAS 05341+0852 based on high resolution spectra. This star shows 3.3 μm and 21 μm emission features which are attributed to carbon-rich molecules such as PAH and Fullerenes, indicating that the circumstellar dust is carbon-rich. Our abundance analysis shows that the star is metal-poor ([Fe/H]=-1.0) and carbon-rich (C/O$\approx$2.2). The light element Li is found to be overabundant which is about 100 times (log ϵ Li=2.5) more than that observed Li in normal giants and supergiants. Carbon, nitrogen, oxygen, aluminum and silicon are found to be overabundant. More importantly this star has large overabundance of s- process elements. So far IRAS 05341+0852 is the only post-AGB star showing overabundance of Li, C, Al and s-process elements which are all in general agreement with the predictions of the third dredge-up and Hot Bottom Burning AGB evolutionary models. However these theoretical models suggest that Li and Al are produced in significant amounts during the HBB in massive AGB stars. The [S/Fe]=0.07 indicates that the low Fe abundance is intrinsic and it is not due to fractionation in this case. We compared the high-resolution spectra and results of a well known post-AGB star HD 56126 with that of IRAS 05341+0852. We found the spectra of IRAS 05341+0852 is more dominated by s-process elements than that of HD 56126 and Li is not found in HD 56126. The low Fe abundance ([Fe/H]=-1.0) of IRAS 05341+0852 indicates that it is a low-mass post-AGB star. The overabundance of Li and Al suggest that HBB may take place in the low-mass AGB stars also.

In chapter 5, we study the chemical composition of few bright post-AGB stars selected based on their infrared, optical and kinematical properties. The stars studied in this chapter are: HD 179821, HD 70379 (chapter 2) and IRAS 18095+2704. In this chapter we try to understand the possible nature of an unusual object HD 179821. This object has been classified as either a run away O- type supergiant, or a post-AGB star mimicking population I supergiant or a massive yellow supergiant evolving from massive red giant branch to Wolf-Rayet phase. The low Fe abundance and overabundance of s-process elements and carbon and also the high radial velocity indicate that HD 179821 is a low-mass post-AGB supergiant and not a massive red supergiant. We find HD 70379 is slightly metal-poor with overabundance of C,O and s-process elements. We thoroughly discuss the results of chemical composition and compared with theoretical predictions. These results combined with its kinematical properties suggest that HD 70379 is a post-AGB star. The chemical analysis of IRAS 18095+2704 suggests that star is oxygen-rich. This result is consistent with the oxygen-rich dust envelope of this object.

In Chapter 6, we study HD 105262 which has high C1-index and large proper motion ($0''.057$ year^{-1}). The large proper motion post-AGB supergiant stars are very rare. HD 105262 is a high galactic latitude ($+72°$) A-type star. Earlier, it was classified as a Field Horizontal Branch (FHB) star. Recently, Abt (1993) suggested that it may be a star similar to HR 4049. We analyze the optical medium and high resolution spectra. The results of spectroscopic analysis of HD 105262 indicate that it has gone through the AGB nucleosynthesis. The chemical composition, absolute magnitude, high galactic latitude and kinematics indicate that HD 105262 is a halo metal-poor post-AGB A supergiant and not a Field Horizontal Branch Star.

Contents

Chapter 1

Introduction

1.1 General introduction

Stars, like people and the Universe, grow old and die, but they do not go gentle into the good night—the raging of a supernova is approached in luminosity only by that of gas about to be devoured by a massive black hole. Low and intermediate-mass stars die much less spectacularly, but their deaths are far from insignificant. In the course of prodigal consumption of nuclear fuel which occurs after the main sequence phase, evolving stars increase their luminosity by factor of 10^4 or more and expand to great sizes. The cool outer layers of the star are weakly bound to it at this stage, and they are ejected by the star in the form of a wind. During the second ascent of the giant branch (the asymptotic giant branch phase or AGB) a ferocious struggle occurs in the interior of the star—can the star shed its outer envelope before the core mass grows above the Chandrashekar mass limit of 1.4 $M_\odot$ and the star explodes as supernova? If so, the central degenerate remnant evolves to its final white dwarf stage, ionizing the circumstellar material to form a planetary nebula. The circumstellar gas then moves away from the star and is returned to the interstellar medium.

—Knapp (1991)

In this thesis, we study these less spectacular, but more significant low and intermediate-mass evolved stars which contribute $\approx 70\%$ of chemically enriched dust material to the interstellar medium. The dust contribution by various group of stars

1
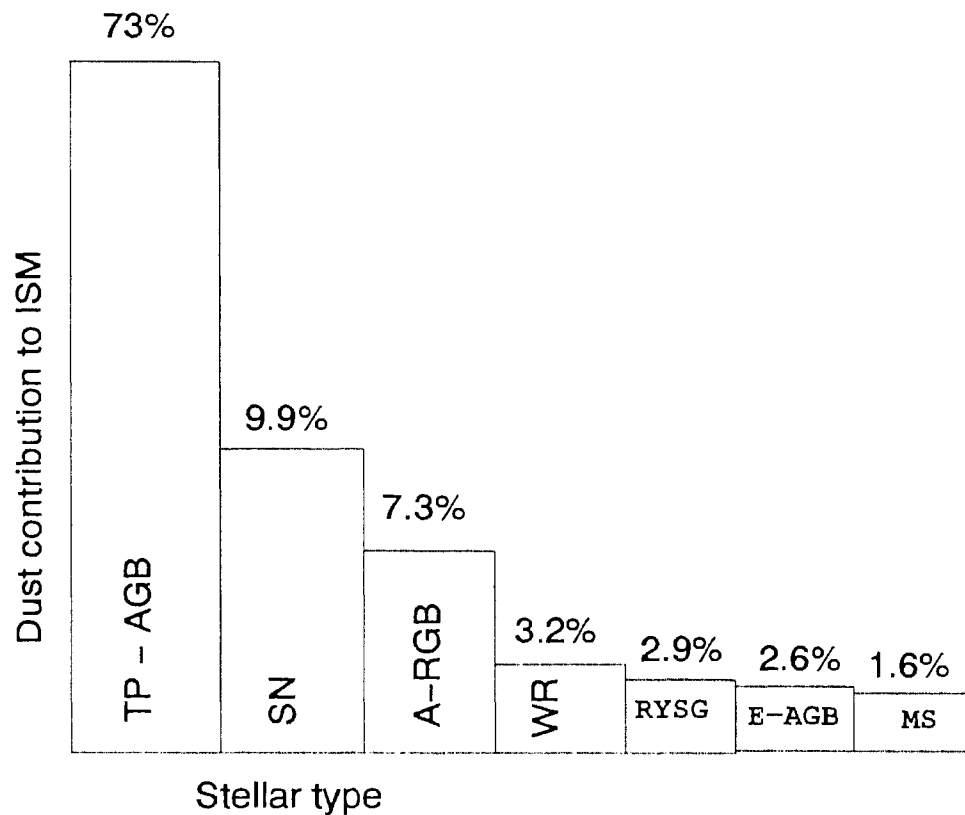
Figure 1.1: *Dust contribution to the ISM by various groups of stellar objects. TP-AGB: thermally pulsing AGB stars, SN: suprenovae, A-RGB: Asymptotic red giant branch stars, WR: Wolf-Rayet stars, RYSG: red and yellow supergiants, E-AGB: early AGB stars, MS: main sequence stars. (After Sedlmayr 1994)*

is shown in Fig.1.1. Stars form in the interstellar gas which is contaminated by dust thrown by evolved stars. Thus the newly formed stars have metal enriched chemical composition. The schematic diagram shown illustrates the role of these objects in the chemical evolution of galaxies. Today there is a general understanding of stellar evolution from star birth in the interstellar clouds to star death as either a white dwarf (low and intermediate-mass stars) or a neutron star or a black hole (massive stars $M \geq 9 M_{\odot}$). However the late stages of stellar evolution are not well understood, both theoretically and in particular, observationally. The stellar evolutionary phase between the AGB and Planetary Nebulae (PNe) was a missing link in stellar evolution

for a long time. The Infrared Astronomical Satellite (IRAS) mission in 1983 made it possible to understand this transition phase considerably. Now it is believed that post-AGB stars are the immediate precursors of PNe. To date, many sources from the IRAS database have been proposed as post-AGB candidates but very few of them have been studied in detail. It is highly important to discover more post-AGB stars and study them in detail, especially in terms of their chemical composition. After a brief introduction to the evolution of low and intermediate-mass stars (section 1.2) and their chemical composition in various stages of stellar evolution (section 1.3), we give a brief introduction to the post-AGB stars, various groups of post-AGB stars and their observational properties in section 1.4 .

1.2   Evolution of low and intermediate-mass stars

In this section we present a brief qualitative picture of evolution of low (M$\leq 2.3 M_\odot$) and intermediate (M$\leq 8 M_\odot$) mass stars. It is believed that stars form in gravitationally unstable interstellar clouds. Initially, a cool cloud of interstellar gas contracts gravitationally, giving off radiation in the far infrared (far-IR). As the contraction proceeds, the cloud temperature rises. The surface temperature remains constant for a long period as the proto star becomes smaller and smaller. Thus the luminosity of the star decreases during this stage but the colour remains constant. The Hayashi track of the star on a Hertzsprung-Russel (H-R) diagram is therefore represented by a nearly vertical line. Iben (1965) suggested that this stage is followed by a nearly horizontal track towards the main sequence. During this phase, the star reaches a central temperature of around 10^6 K. As light elements like lithium and deuterium are burnt, the track may undergo some short-lived changes. When the track of this gravitationally contracting star intersects the main sequence, the star has reached a point where it will be stable for the longest period of its life consuming the energy liberated from the nuclear fusion of hydrogen into helium. The onset of nuclear burning on the main sequence makes the details of prior evolution largely irrelevant to subsequent evolution.

Further stellar evolution off the main sequence largely depends on the initial mass

of the star on the main sequence. After exhaustion of core hydrogen, low and intermediate stars move towards the right in the H-R diagram, burning hydrogen in the shell and dumping the resultant helium on the core. This central helium core contracts gravitationally to support the outer envelope of the star. As the mass of the central core continues to increase, the core slowly contracts and its temperature rises. The increase in the core temperature causes an increase in luminosity. The increased luminosity in turn causes the outer envelope of the star to expand, decreasing the temperature gradient. The result is that the star moves upward and a little to the right in the H-R diagram. Stellar evolutionary tracks of 1 $M_\odot$ and 5 $M_\odot$ in the H-R diagram are shown in Fig. 1.2. The process continues until the temperature gradient exceeds the adiabatic gradient. Then the entire outer envelope becomes convective. Convection occurs over a greater depth for more massive stars. The stars now follow approximately the track of a fully convective star (Hayashi track), but in reverse. This phase in stellar evolution is known as *Red Giant Branch (RGB)* of evolution.

Further evolution of low-mass stars differs significantly from that of intermediate mass stars. A massive star has a convective core and does not have a helium degenerate core. In the massive star, central temperature reaches 10^8 K faster than in the low-mass stars and burning of the central helium sets in earlier. In the central cores of a massive star, helium burning terminates when He is completely processed into carbon and oxygen. During this phase the star loops back and forth near the Hayashi line. While the helium shell burns outwards, the C-O core increases in mass and contracts. This is similar to the situation before helium burning. But now the star has central C-O core, surrounded by helium and hydrogen burning shells. The star now moves upward on the *Asymptotic Giant Branch (AGB)* in the H-R diagram.

The situation of low-mass star is different, because a low-mass star has a radiative core and degeneracy of the core plays an important role in the evolution. As the temperature of the hydrogen burning shell increases and the degenerate core builds in mass, the core temperature ultimately reaches 10^8 K. This triggers the He ignition via the triple-α (3-α) process. Under normal conditions, the burning of helium could begin in a measured way as in massive stars. However, the core is degenerate, so the electron pressure is only weakly dependent on temperature. A further increase
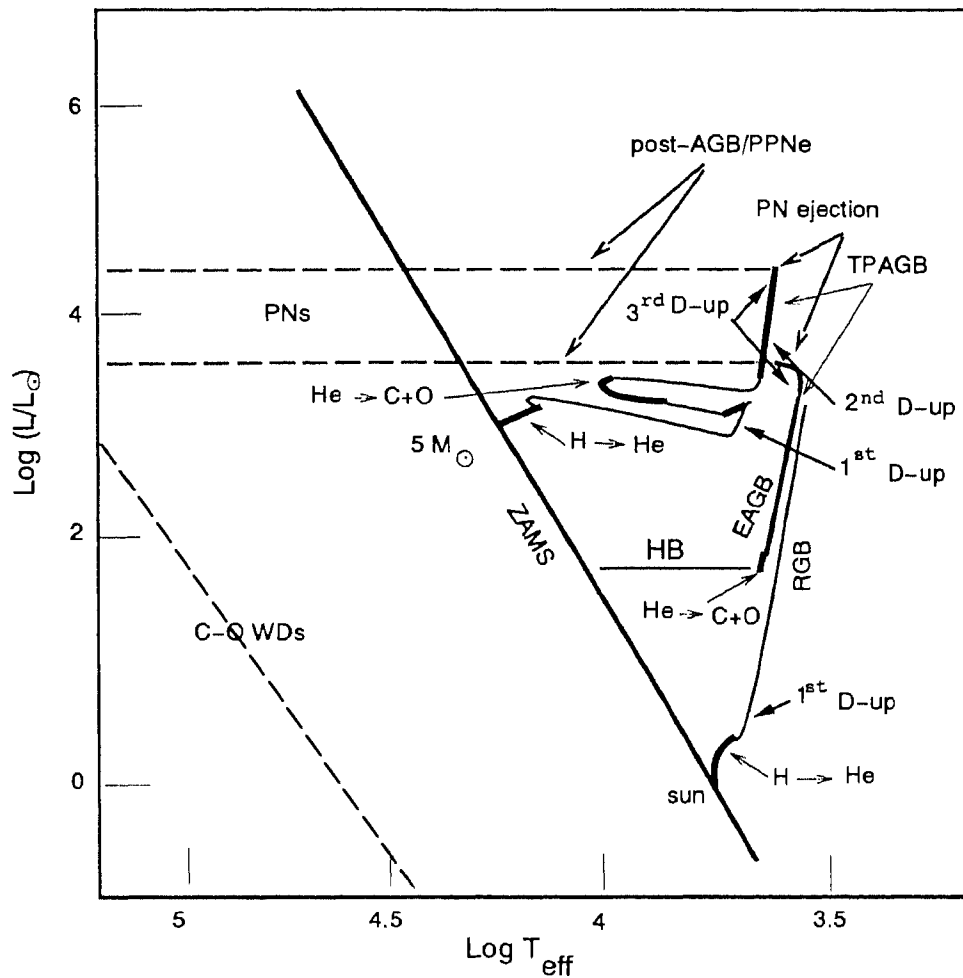
Figure 1.2: *The evolutionary tracks in the H-R diagram for stars of 1.0 $M_\odot$ and 5.0 $M_\odot$. The heavy portions of each curve indicate where major nuclear burning stages occur in the core. The label ZAMS refers to the Zero Age Main Sequence, RGB to the Red Giant Branch, HB to the Horizontal Branch, AGB to the Asymptotic Giant Branch, EAGB to the Early-AGB, TPAGB to the Thermally Pulsing-AGB and PPNe to the proto-planetary nebulae. The main episodes of mixing (1st, 2nd and 3rd dredge-up) are indicated by 1stD-up, 2ndD-up and 3rdD-up, respectively (after Chiosi 1992).*

in temperature, therefore, increases the nuclear reaction rates and leads to thermal runaway and an enormous over-production of nuclear energy. The local luminosity at maximum reaches $10^{11} L_\odot$, about that of a whole galaxy for a very short duration of time. However, these effects are not seen at the surface of the star, as the radiation is absorbed by the expansion of the outer non-degenerate layers. After the violent helium flash, there follows a phase of quiet burning of helium in non-degenerate matter, called *Horizontal Branch (HB)* in the H-R diagram. This is also known as helium main sequence since helium is being burnt in the core. In this phase, hydrogen burns in a shell. The mass of the helium core grows as a result of hydrogen shell burning and the core helium is converted to carbon and oxygen. When the helium in the core is exhausted the star's evolution on the HB terminates, and it evolves along the AGB.

A star massive enough to evolve off the main sequence and less massive than 8 $M_\odot$ evolves into an AGB star with an electron-degenerate core composed of carbon and oxygen. All stars in this phase are confined to a very small region of the H-R diagram, with surface temperature in the range 2500-5000 K. During the AGB phase, a low-mass star follows a path very close to the RGB which is defined by shell hydrogen burning stars with electron-degenerate helium core.

The evolution of low and intermediate stars on the AGB phase can be separated into two parts: the early AGB phase (E-AGB) which lasts until the H-burning shell is reignited and the thermally pulsing AGB phase (TP-AGB) which lasts until the H-rich envelope is lost via mass-loss. As helium in central regions is completely exhausted, C-O core contracts and heats up while the H-rich envelope expands and cools. Cooling in the layers external to the C-O core is so effective that the H-burning shell is extinguished. In the H-R diagram (Fig.1.2) the AGB stars evolve almost parallel to the RGB. Eventually the expansion of the envelope is halted by its own cooling and the envelope recontracts and the material at the base of the convective envelope heats up. Ultimately, the H-burning shell is reignited. This terminates E-AGB. Meanwhile the matter in the C-O core reaches such high densities that the electrons there become degenerate. Following the reignition of the shell H-burning, nuclear burning in the He-shell becomes thermally unstable (Iben and Renzini 1983,
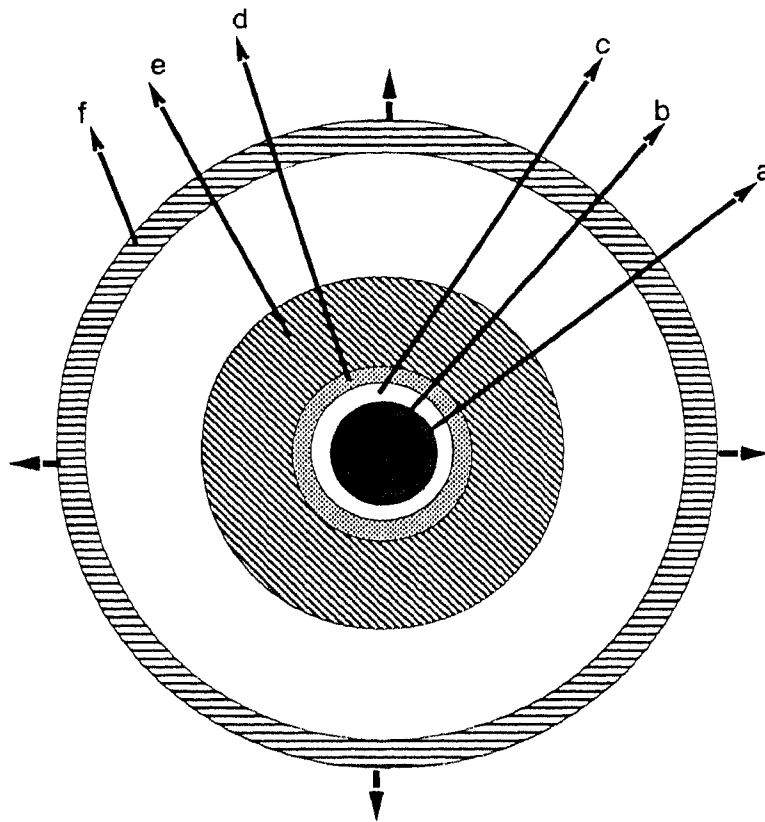
Figure 1.3: *A schematic diagram showing the structure of a (post)-AGB star. a:* *C+O degenerate core, b: He—burning shell, c: a thin intershell mostly composed of* *He., d: H—burning shell, e: deep convective envelope, f: detached expanding dust* *envelope.*

1984; Iben 1991) and leads to thermal pulsation. A typical AGB star has the following structure: (1) a degenerate core composed of a mixture of ^{12}C and ^{16}O, (2) a narrow helium-burning shell source, (3) a thin intershell layer composed of mostly He, (4) a narrow hydrogen-burning shell source and (5) an extended outer envelope (Fig. 1.3). The dominant energy source for thermal pulses to occur is the 3-α reaction similar to helium-core flash on the RGB. Here burning occurs in a non-degenerate region between the C-O degenerate core and the He and H discontinuity. The energy released by 3-α reaction, goes to expand the outer layers due to which cooling sets in and helium burning begins to die down. The matter expelled by expansion reaches

out to such low temperatures and densities that the hydrogen burning is effectively shut off. Ultimately, when the helium burning luminosity falls below the surface luminosity, the propelled matter falls back and gets heated until hydrogen burning sets in. The alternate burning of He and H shells generates *thermal pulses* (Iben 1983; Renzini 1981). During this phase, processed material in the intershell region can be brought up to the outer convective envelope and exposed to the surface. This is known as *third dredge-up*.

The evolution along the AGB is greatly influenced by the mass-loss. As the stars ascend the AGB, thermal pulses increase and hence the mass-loss also increases. Stars on the AGB grow in size ($R_* = 250\text{-}500\ R_\odot$), and as result their surface gravity decreases enormously. Stars on the AGB are cool ($T_{eff} \leq 5000$ K), highly luminous ($L_{bol} \approx 10^4$), and lose mass at rates of 10^{-8} to $10^{-4} M_\odot yr^{-1}$ (Knapp et al 1982). The matter propelled by mass-loss forms dust around the star. At the tip of the AGB many stars are hidden by thick dust shells and emit most of their energy in the infrared regions. Typical AGB stars are Mira variables and OH/IR stars. The stars on the AGB are classified as oxygen-rich and carbon-rich stars based on their infrared spectral features.

The spectra of oxygen-rich stars are characterized by 9.7 μm and 18 μm circumstellar silicate features and carbon-rich stars by 11.3 μm emission feature of SiC. Evolution of the emission feature at 9.7 μ in the E-AGB stars (Mira variables) to self-absorption in the evolved AGB stars (OH/IR stars) confirms the increasing mass-loss as the star ascends on the AGB (Kwok 1993). When the mass of the hydrogen burning envelope drops below a certain limit ($10^{-2} M_\odot$) the AGB evolution is terminated and the star starts to move blueward in the H-R diagram. Now the star evolves in the post-AGB phase of evolution. During this phase the optically thick dust shell gets diluted due to its continuous expansion and decreasing mass-loss, and the star becomes optically visible again. IRAS observations have detected several objects with spectral types FI and GI which are surrounded by cool and detached dust shells (Parthasarathy and Pottasch 1986; Likkel et al 1987; Pottasch and Parthasarathy 1988). Typical members of this stage are also the non-variable OH/IR stars (Bedijn 1987). During this phase central stars evolve, with increasing temperature, towards

planetary nebula

and when the nebula dissipates into the ISM, the star evolves to its final stage as a white dwarf.

1.3 Chemical evolution

The determination of chemical composition is an important aspect in stellar structure and evolutionary studies. The chemical composition analysis of AGB and post-AGB stars would provide clues to understand the nucleosynthesis, mixing and mass-loss in the advanced stages of evolution of low and intermediate-mass stars. In the following sections we discuss briefly the chemical composition and dredge-up process in the major stellar evolutionary phases. We use a standard notation: $[X] = log_{10}(X)_{star} - log_{10}(X)_{sun}$ to represent any quantity X (e.g Fe/H, C/Fe etc.) in the stellar atmospheres.

1.3.1 Main Sequence

The burning of hydrogen into helium in the main sequence takes place in low-mass main sequence stars, through mainly the reaction called PP chain, and in the upper main sequence stars through the CNO cycle. The final result of these two types of reactions is to convert four ^{1}H nuclei into one ^{4}He nucleus. In low-mass stars hydrogen burns through the following PP chain reaction.

$$^1H + {}^1H \rightarrow {}^2H + e^+ + \nu$$
$$^2H + {}^1H \rightarrow {}^3He + e^+ + \gamma$$

$$^3He + {}^3He \rightarrow {}^4He + 2{}^1H$$
(pp1)

$$^3He + {}^4He \rightarrow {}^7Be + \gamma$$

$$^7Be + e^- \rightarrow {}^7Li + \nu$$
$$^7Li + {}^1H \rightarrow {}^4He + {}^4He$$
(pp2)

$$^7Be + {}^1H \rightarrow {}^8B + \gamma$$
$$^8B \rightarrow {}^8Be + e^+ + \nu$$
$$^8Be \rightarrow {}^4He + {}^4He$$
(pp3)
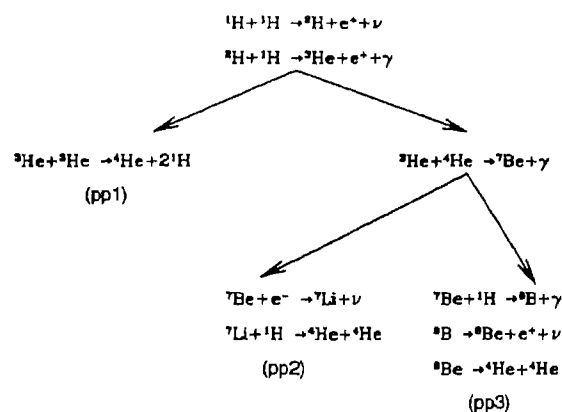
The CNO cycle is the other main series of reactions through which hydrogen burns on the main sequence in the intermediate-mass and more massive stars. It requires the presence of some isotopes of CNO to act in a manner similar to catalysts in chemical reactions. The sequence of reactions can be represented as follows:

$$^{12}C + {^1}H \rightarrow {^{13}}N + \gamma$$
$$^{13}N \rightarrow {^{13}}C + e^+ + \nu$$
$$^{13}C + {^1}H \rightarrow {^{14}}N + \gamma$$
$$^{14}N + {^1}H \rightarrow {^{15}}O + \gamma$$
$$^{15}O \rightarrow {^{15}}N + e^+ + \nu$$
$$^{15}N + {^1}H \rightarrow {^{12}}C + {^4}He$$

$$\rightarrow {^{16}}O + \gamma$$
$$^{16}O + {^1}H \rightarrow {^{17}}F + \gamma$$
$$^{17}F \rightarrow {^{17}}O + e^+ + \nu$$
$$^{17}O + {^1}H \rightarrow {^{14}}N + {^4}He$$
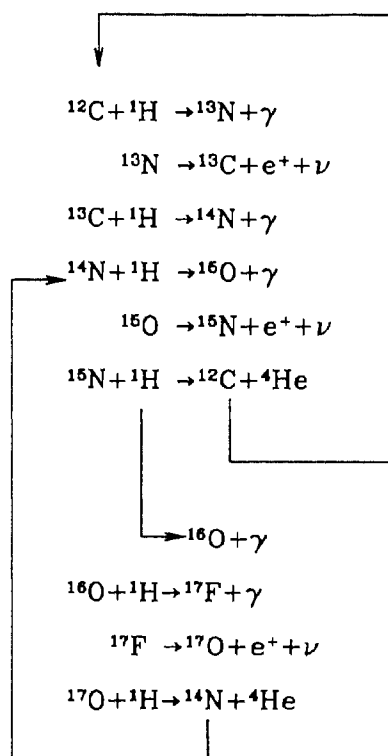
1.3.2 Red Giant Branch

Theoretically it is known that during the main sequence lifetime of a star there is a gradual conversion of ^{12}C into ^{13}C and ^{14}C through the CNO cycle hydrogen fusion reactions. As the star becomes a red giant, its deepening convective envelope serves to mix its altered interior element isotopes with the outer envelope layers. This is the first indication of interior nucleosynthesis that becomes visible at the stellar surface. This mixing process in the RGB stars is called *first dredge up*. The quantitative estimates for the changes in surface C and N contents in Population I solar metallicity stars during the RGB suggest that: (a) the C/N value in giants drops to ≈ 1 from

the main sequence value of $\approx$ 5, (b) the $^{12}C/^{13}C$ ratio would decrease from $\approx$ 90 to about 20-30 (c) the ^{16}O abundance would not be altered because the ON portion of the CNO cycle would not be effective in the relatively low temperatures of the stellar core regions reached by convective envelope (Iben and Renzini 1984; Wheeler and Sneden 1989). These predicted changes in abundances have been confirmed by observations of RGB stars (Lambert and Ries 1981). Recent determination of carbon isotope ratio in giants of open clusters (Gilroy 1989) also supports the theoretical predictions. However the studies of chemical composition of old disc and population II RGB stars suggest that the theoretical description of first dredge-up may not be able to explain the observed chemical composition (Langer and Kraft 1984; Sneden et al 1986).

1.3.3   Asymptotic Giant Branch

Observations reveal that CNO and the s-process elements like Sr,Y,Ba are synthesized in the low and intermediate-mass stars on the AGB and brought to the surface. The 3-α reactions which contribute large overabundance in carbon, occur at central temperatures $\geq 10^8$ K. This is accomplished via two steps:

$$^4He +^4 He \rightarrow^8 Be$$

$$^8Be +^4 He \rightarrow^{12} C + \gamma$$
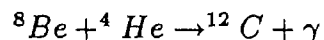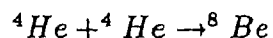
Once sufficient ^{12}C has been produced by 3-α reaction, further α particle captures on carbon yield oxygen via the reaction $^{12}C +^4 He \rightarrow^{16} O + \gamma$. This reaction destroys carbon, but the destruction of carbon is negligible compared to the production of carbon in the helium shell flashes on the AGB. To bring by-products of these nuclear reactions from the interior of the AGB star to the photosphere, two transport mechanisms operate. One is the second dredge-up in the E-AGB star and the other is third dredge-up in the TP-AGB star due to the deep convective envelopes. The second dredge-up results in further decrease in carbon and increase in nitrogen and almost no changes in the oxygen abundance.

For the stars of initial mass $\geq 2M_\odot$, because of the intensive thermal pulses the base of the convective envelope reaches the region containing highly processed material (Iben and Renzini 1983 and refs therein) which brings freshly synthesized ^{12}C and neutron-rich isotopes to the surface. This is the result of third dredge-up. The severity of third dredge-up depends on the number of pulses on the AGB. Presence of carbon stars (C/O $\geq$1.0) and s-process element rich stars confirm the third dredge-up predictions. We discuss these aspects in detail later in this study.

1.4 Post-AGB stars

It is understood from section 1.2 that only low and intermediate stars go through the AGB phase of stellar evolution. In this section we discuss post-AGB phase, various groups of post-AGB stars and their observational properties.

After the termination of AGB the star evolves towards higher temperature, but with constant luminosity, ionizing its circumstellar material to form a Planetary Nebula (PN). Recombination lines of hydrogen and forbidden lines of metals will make the nebula easily observable in the visible. The stellar evolutionary phase (low and intermediate-mass stars) between the end of the AGB and PN is known as Post-AGB/Proto-planetary Nebula (PPN) phase.

We investigate in this thesis, this late stage of stellar evolution in between AGB and PN phases. The post-AGB/PPNe stars are those that have stopped large scale mass-loss on the AGB (Habing et al 1987; Kwok 1993), but have not evolved to be hot enough to emit a sufficient quantity of Lyman-continuum photons to ionize the surrounding remnants of the AGB envelope. Recent, multi-wavelength studies of these transition objects suggest that the following types of stars are most likely post-AGB stars: i)luminous high latitude supergiants ii) IRAS sources having far-IR colours similar to planetary nebulae, iii) RV Tau stars, iV) UU Her stars and UV bright stars in globular clusters.

1.4.1 Luminous high latitude stars

Ever since Bidelman (1951) noticed A and F supergiants (HR 6144, 89 Her and HD 161796) at high Galactic latitudes, the question of their origin evoked much debate in the literature (Luck and Bond 1984; Lamers et al 1986; Hrivnak and Kwok 1991; Sasselov 1984). Parthasarathy and Pottasch (1986) for the first time discovered the fact that the far-IR colours of some bright high galactic latitude supergiants, are similar to PNe colours. They concluded that the detached cold circumstellar dust shells around the high latitude supergiants is the result of severe mass-loss experienced by these stars in the recent past during their AGB phase of evolution. The superwind type of mass-loss has terminated their AGB phase of evolution. Based on the available data Parthasarathy and Pottasch (1986) concluded that the high latitude supergiants are low-mass stars in post-AGB stage of evolution.

Recent studies show that several high latitude A and F supergiants have high space velocities, low metal abundances (Bond and Luck 1987), circumstellar dust shells
(Parthasarathy and Pottasch 1986), and molecular envelopes (Likkel et al 1987) which indicate that these are low-mass evolved stars. The supergiant like spectra of these stars indicate an extended atmosphere around the low-mass $(0.6M_\odot)$ C-O core.

Examples of high latitude supergiant stars which are thought to be post-AGB objects, based on their IR excess and spectroscopic studies, include HD 161796, HD 56126, HD 101584 (Parthasarathy and Pottasch 1986; Parthasarathy et al 1992) HD 52961, HR 4049 (Waelkens et al 1991), HR 4912, HR 7671, HR 6144, HD 161796
(Luck et al 1990), IRAS 18095+2704 (Hrivnak et al 1988) and HD 105262 (Reddy et al 1996). There may be many more objects among the luminous high latitude stars, which are infact low-mass post-AGB stars. A systematic spectroscopic study of these stars is highly important.

1.4.2 IRAS sources

Before the IRAS mission in 1983 only two transition objects were known , AFGL 618 which is a bi-polar PPN (Westbrook et al 1975) and AFGL 2688 (Ney et al 1975).

The IRAS mission surveyed 95% of the sky in four broad band far-IR filters at 12 μm, 25 μm, 60 μm and 100 μm. The IRAS fluxes of several thousand point sources have been listed in a catalogue called Point Source Catalogue (PSC). Classification of IRAS sources in PSC based on IRAS colour-colour diagram (Pottasch et al 1988; van der Veen and Habing 1988) led to the idea that the sources in between OH/IR sources and PNe in the diagram are possibly post-AGB or young planetary nebulae. In this diagram PNe region is well separated from H II regions, galaxies and main sequence stars.

By assuming that the infrared properties of PNe are inherited from post-AGB or AGB stars, many unidentified IRAS sources having far-IR colours similar to PNe have been suggested as possible post-AGB candidates (Prete- Martinez 1988; Manchado et al 1989; Garcia-Lario et al 1990). Through studies of dust envelope evolution (Habing et al 1987), OH and CO millimeter properties (Hu et al 1993a) and optical spectral properties (Hrivnak 1995; Hu et al 1993b) many IRAS sources have been identified as potential candidates for post-AGB stars. For example IRAS 18095+2704 (Hrivnak et al 1988), IRAS 17514-1555 which is bi-polar proto-planetary nebula (Hu and Bibo 1990), IRAS 04296+3429, IRAS 05113+1347,IRAS 2000+3239 and IRAS 23304+6147 (Hrivnak 1995 and refs therein) are recognized as post-AGB stars based on the above studies. There are probably many more IRAS objects in the transition region between AGB and PNe, which are still embedded in optically thick dust shells which are inaccessible to the optical studies.

It is also realized that the bright stars in SAO and HD catalogues having dust properties similar to PNe may be post-AGB stars. From an analysis of IRAS PSC a new class of stars was detected. These stars have circumstellar dust shells with far-IR colours and flux distribution similar to the dust shells of PNe and most of them show A, F, G and K supergiant like spectra in the optical region (Parthasarathy and Pottasch 1986; Lamers et al 1986; Pottasch and Parthasarathy 1988; Hrivnak et al 1989; Waelkens et al 1989; Trams et al 1991; Oudmaijer et al 1992). Parthasarathy and Pottasch (1986) interpreted that the dust shells around these stars are the result of mass-loss during the AGB phase of evolution. It is likely that these objects are in a hitherto unseen post-AGB stage of stellar evolution. Some of these stars are at high

Galactic latitudes, have high space velocities and are metal-poor, indicating that they have evolved from low-mass stars and are now in the post-AGB stage of evolution.

RV Tauri stars:

RV Tau stars are variables located just above the horizontal branch and to the left side of the AGB, in the H-R diagram. Preston et al (1963) have described the basic properties of RV Tau stars: they are luminous pulsators of spectral class F, G and K. From their optical classification , they estimate that $M_v \approx -3$ which corresponds to a luminosity of $\approx 10^3$ $L_\odot$. Recent studies by Jura (1986) and Wahlgren (1993) reveal that all the observed RV Tau stars have infrared excess ranging from 1.2 to 4.9 mag. The dust around these stars can probably be attributed to the mass-loss phenomenon on the AGB. From the infrared and statistical properties of these stars Jura (1986) suggested that the RV Tau stars are in post-AGB stage of evolution.

The key test for the post-AGB nature of RV Tau stars lies in chemical composition studies. Luck and Bond (1989) have analyzed the high resolution spectra of few RV Tau stars. The RV Tau star RU Cen is metal-poor ([Fe/H]=−1.4) and displays slight overabundance of carbon and s-process elements. Other stars such as AC Her ([Fe/H]=−1.2), U Mon [Fe/H]=−0.8) and R Sct ([Fe/H]=−0.9) display the s-process element deficiency. The location of RV Tau stars at high latitudes, their metal deficiency, the spectral characteristics and the presence of circumstellar dust around them suggest that these are low-mass post-AGB supergiants. The detailed chemical composition studies of RV Tau stars are hampered by the large variation in effective temperatures of its photosphere and line doubling and emission due to the presence of a shock-front in the outer layers of the photosphere (Wahlgren 1993).

Hot-post-AGB stars:

Previously all high latitude B-type supergiants were thought to be massive young stars based on their low resolution spectra. Recent studies of these objects (Conlon et al 1991) suggest that some of these stars are in fact post-AGB supergiants. These include LB 3193, LB 3116 and LS IV -12 111 . Chemical composition studies of few high latitude B-type supergiants (McCausland et al 1992) indicate low metallicity, carbon deficiency and over abundance of He which are highly incompatible with the interpretation of their being massive Pop I stars. The studies also confirm that these

stars have experienced first and second dredge-up process. LS IV -12 111 and LS II +34 26 have been found to be IRAS sources, having IRAS excess similar to post-AGB stars (Parthasarathy 1993). The spectra of LS IV -12 111 and LS II +34 26 show nebular emission features indicating that they are hot post-AGB stars. Parthasarathy (1993) discovered detached dust shell around the B-type high latitude supergiant LS II +34 26, and concluded that it is hot post-AGB star and not a massive B star in the outer edge of the Galaxy.

UU Her stars:

These are semi-regularly varying F and G type supergiants, located high above the galactic plane. The amplitude of the variations is about 0.5 mag with a characteristic timescale between 40 and 100 days (Sasselov 1984). Their chemical composition and pulsation characteristics suggest they are low-mass stars in post-AGB stage of evolution (Sasselov 1984)

1.4.3   Properties of post-AGB stars

In this section we briefly outline the observed properties of these transition objects between the tip of AGB and PN phase.

infrared excess:

This is a common characteristic of all transition objects, which is due to the emission by cool dust. Infrared excess in post-AGB stars suggests that they have gone through the mass-loss episodes during their life time on the AGB phase of evolution. However a few high latitude post-AGB stars are not IRAS sources (HD 105262, BD +39° 4926). It may be possible, in the case of low mass post-AGB stars, that the transition time is so long, all the material ejected during the AGB phase might have been dispersed into the ISM by now. Such non-IRAS post-AGB stars may become white dwarfs, without going through the planetary nebula phase.

dust temperatures:

The evolutionary sequence of IRAS sources in the colour-colour diagram (Habing et al 1987) suggest that the expected dust temperatures of post-AGB stars are between 100-300 K. It is found that the typical dust temperature of PNe is around 100 K
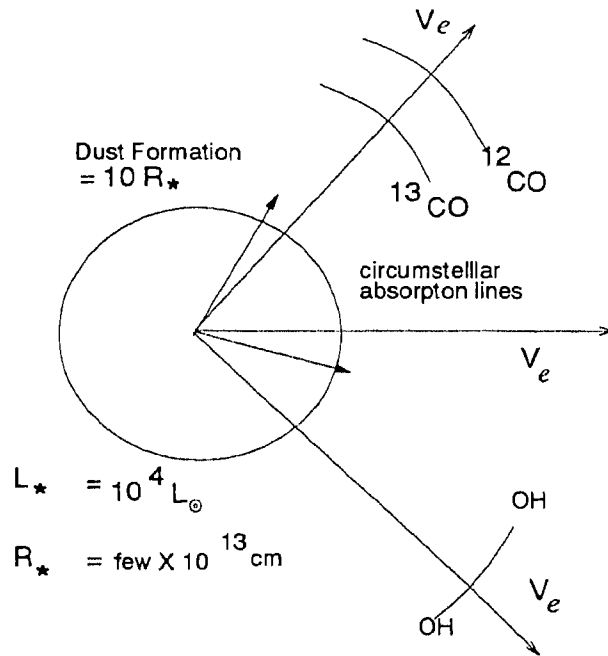
Figure 1.4:   *Circumstellar environment of cool mass-loosing AGB star. The OH and CO molecular features are marked. Dust is formed at few R_* (After Knapp 1991)*

and for the AGB stars it is around 300 K. This is consistent with the dust envelope evolution from AGB to PN, with increasing envelope radii and decreasing dust temperature (Pottasch et al 1984; Iyenger 1986).

molecular features:

Detection of OH, CO and HCN emissions in the post-AGB stars shows the presence of molecular envelopes around these stars. A sketch of the circumstellar environment is shown in Fig. 1.4.   These detections show that there are both carbon rich and oxygen-rich post-AGB stars. OH and CO originate from the molecular envelope far away from the central sources. The expansion velocities and mass-loss rates derived from the CO millimeter observations also clearly indicate that these are evolved stars.

1.4.4 Chemical composition

Generally one expects that the post-AGB stars should show over abundance of Li, CNO and s-process elements. But the available chemical composition studies of post-AGB stars present a very diverse chemical composition pattern. Here we give a brief overview of the observed abundance patterns of these stars.

Several of the post-AGB stars are high latitude supergiants which are generally metal-deficient indicating that they may belong to old disk or halo. The elemental abundances of the extremely metal-poor post-AGB stars (HD 52961, HR 4049, HD 44179, BD $+39°$ 4926 and HD 46703, HD 105262) are hard to explain. None of these stars satisfy the expected chemical properties of the post-AGB stars. Only two sources HD 52961 and HD 44179 (Waelkens et al 1992) show a mild over abundance ([hs/Fe]=0.6) of s-process elements and rest of the sources (Waelkens et al 1991; Luck et al 1983; Kodaira 1973) are found to be deficient in s-process elements. Surprisingly, for all the sources CNO and S abundances are nearly solar irrespective of their metallicity. Van Winckel et al (1992) found that the observed chemical composition of very metal-poor post-AGB stars are similar to that of the gas phase abundances of the interstellar medium (ISM). They suggested that this peculiar chemical composition may be due to the selective fractionation of refractory elements into circumstellar dust (see for details Bond 1991; Lambert 1991; Parthasarathy et al 1992). Recently Van Winckel et al (1995) found that many of these stars are binaries. They concluded that these stars are more likely represent a particular stage of binary evolution rather than being typical post-AGB stars.

Luck et al (1990) discussed the chemical composition of four A- and F- type high latitude supergiants, HR 6144, HD 161796, 89 Her and HR 7671. The abundance results of these stars suggest that these are not pop-I supergiants. The first three stars are slightly metal-deficient ([Fe/H]=-0.4) and show over abundance both in carbon and nitrogen, however oxygen is over abundant only in the first two stars. Their location in the H-R diagram, circumstellar dust and molecular envelopes suggest that these are low-mass stars in the post-AGB stage of evolution. However, HR 6144, HD 161796 and 89 Her do not reveal the enhancements of s-process elements seen in

highly evolved AGB stars.

There are two post-AGB stars HD 56126 (Parthasarathy et al 1992; Klochkova 1995), HD 187885 (Van Winckel et al 1996) for which the chemical composition supports the post-AGB nature of these objects. HD 56126 and HD 187885 are high latitude moderate metal-poor supergiants. The significant overabundance of CNO and s-process elements confirms the post-AGB nature of these objects.

Chapter 2

IRAS post-AGB candidates

2.1 Introduction

Planetary nebulae are strong infrared emitters. The IRAS fluxes of planetary nebulae show flux maximum around 25 μm or 60 μm indicating the presence of detached cold dust shells having temperatures 100 K to 300 K. At present 1200 to 1500 planetary nebulae are known. The IRAS data may contain a few thousand of these objects which have not yet been identified and studied. Since the evolutionary time from the Asymptotic Giant Branch (AGB) to Planetary Nebula (PN) phase is short, we expect that the remnant of the circumstellar envelope created during the AGB should still be present in a PN. In fact all the transition region objects which are in between the tip of the AGB and PNe are expected to have circumstellar dust shells with far-IR colours similar to planetary nebulae. Applying the above mentioned concept many young PNe and post-AGB candidates have been discovered (Parthasarathy and Pottasch 1986, 1989; Habing et al 1987; Pottasch and Parthasarathy 1988; Manchado et al 1989; Preite-Martinez 1988; Garcia Lario et al 1990; Hu et al 1993a).

In fact Parthasarathy and Pottasch (1986) discovered that some of the high latitude bright F supergiants have dust shells similar to PNe and they concluded that they are low-mass stars in post-AGB stage of evolution. Since then several post-AGB objects have been detected from an analysis of IRAS data (Parthasarathy and Pottasch 1989; Lamers et al 1986; Waelkens et al 1987; Pottasch and Parthasarathy 1988;

Hrivnak et al 1988; Parthasarathy 1993; van der Veen et al 1994). CO observations have also shown that these stars have molecular envelopes with characteristics similar to post-AGB stars (Likkel et al 1987).

In order to ascertain whether an individual IRAS source is a post-AGB star or proto-planetary nebula, additional observations are necessary. Optical observations would be useful especially to know their spectral and luminosity class and hence to fix their position in the H-R diagram. As a part of a program to study post-AGB stars and proto-planetary nebulae, we have obtained CCD photometry and low resolution spectra of several IRAS sources with far-IR colours similar to PNe. In this paper we present BVRI CCD photometry and spectroscopy of 14 IRAS sources which are most likely associated with post-AGB stars and proto-planetary nebulae.

2.2 Sample selection

We have selected the post-AGB stars on the basis of the following criteria:
(a) We have chosen the IRAS sources having colours $F_{12}/F_{25} \leq 0.50$ and $F_{25}/F_{60} \geq$ 0.35 which are typical of PNe from IRAS colour-colour diagram of Pottasch et al. (1990) and objects which have IRAS properties in between AGB and PNe in the van der Veen and Habing (1988) IRAS evolutionary colour-colour diagram (VH diagram). The positions of these sources are shown in Fig. 2.1. Three sources are in box IIIb , two are in box IV, five are in box V and one is in box VIII of the VH diagram. Three sources have very cold dust shells and they fall outside the boundary line ([12]-[25]=2.0) of the VH diagram (Fig. 2.1). IRAS sources in the boxes IIIb, IV and V in the VH diagram are mostly evolved stars with dust around them. The sources which fall in these boxes are most likely post-AGB stars and planetary nebulae (van der Veen and Habing 1988). The sources in our sample and their corresponding positions in the VH diagram are given in Table 2.1. (b) We have selected the objects which have good quality IRAS fluxes in at least three bands. The 100 μm fluxes which carry ' L ' flag (Table 2.1) are upper limits and are affected by infrared cirrus (emission from interstellar dust). (c) AGB evolution of low and intermediate-mass stars is terminated by loss of the outer hydrogen-rich envelope due to severe mass-loss. Severe mass loss

Table 2.1: IRAS data of program candidates. VAR is the IRAS variability index as given in IRAS PSC.

IRAS Name	Association	IRAS fluxes (Janskys)				l	b	VAR
		12μ	25μ	60μ	100μ			
04296+3429		12.77	45.90	15.12	8.92L	166	−09	1
05113+1347		3.79	15.35	5.44	1.62L	189	−14	1
05238−0626	BD−06 1178	0.73	1.76	1.26	1.81L	209	−22	0
05341+0852		4.52	9.89	3.87	7.77L	196	−12	0
06530−0213		6.14	27.45	14.83	03.9	215	−0	0
07253−2001		6.33	15.23	05.95	7.82	235	−01	0
08143−4406		0.61	9.31	5.96	3.64L	261	−05	0
08187−1905	HD 70379	0.72	17.69	12.09	3.53	241	10	0
14429−4539		14.68	33.24	13.43	2.81	323	12	1
17086−2403	CD−23 13192	1.61	11.82	2.13	14.89L	360	09	0
17150−3224		58.04	321.42	268.29	81.41	354	03	0
17291−2402		2.11	19.33	22.73	11.58	03	05	0
17441−2411	RAFGL 5385	42.86	191.13	106.09	27.54L	04	02	0
23304+6147		11.39	59.03	26.38	30.47L	114	01	0

will cease when the mass of the hydrogen-rich envelope becomes so small ($\approx 10^{-3}$ M$_\odot$) that the pulsational amplitude decreases or the pulsation stops altogether (Habing 1990; Schönberner 1990). The average variability of OH/IR stars is around 64% (Likkel 1989). From a study of non-variable OH/IR stars Bedijn (1987) concluded that they are in the very early post-AGB (transition stage) evolutionary stage. In order to find transition objects, we selected IRAS sources with far-IR colours similar to PNe and with very low IRAS VAR indices (0 and 1 Ref. IRAS PSC and Expl. Suppl 1985). In the IRAS PSC the VAR index = (percentage probability source is variable)/10. In the printed version of the IRAS PSC the VAR = 0 indicates that the percentage probability source is variable is between 0 and 10% and VAR = 1 indicates

that the percentage probability source is variable is between 10 and 20%. The IRAS fluxes and the VAR indices of the selected IRAS sources are given in Table 2.1.   (d) We searched for optical associations for the IRAS sources having the above criteria on the POSS/ESO optical sky survey plates. We have chosen the objects which have definite optical counterparts .

The optical identifications for the sources in our sample are given in Fig.2.2. All the sources marked on the CCD frame of V filter are stellar in appearance except IRAS17150−3224 which is a known bi-polar PPNe (Hu et al 1993b). In this study we eliminated IRAS sources which have spectral features typical of main sequence stars. (e) In order for the sources to be observable from the VBO, Kavalur Observatory we restricted our sample to sources in the declination range +62° to −46° and with optical counterparts brighter than $16^m.5$.

2.3   Observations

2.3.1   Photometry

We identified the optical counterparts of 14 IRAS sources on the POSS and ESO optical sky survey plates. We have obtained BVRI, CCD imaging of all these sources using 1.0 m and 2.3 m (VBT) telescopes at Vainu Bappu Observatory (VBO), Kavalur in January 1993. The photometry (imaging) has been done with 1 m telescope at Cassigran mode at focal ratio F/13 equipped with Thomson CSF TH 7882 CCD chip. The image scale at this focus is 15.6 arcsec/mm. Imaging of these sources also has been done with 2.3 m VBT telescope at prime focus with focal ratio F/3 and Astromed CCD detector. This gives image scale of 24.2 arcsec/mm. Since VBO is located at an altitude of 2340 ft above the sea level,which makes the site not ideal for observation in the ultraviolet U passband. Moreover the CCD response in the ultraviolet is very poor unless they are ultraviolet coated. For calibration, we observed standard stars in the dipper asterism region of M67. The usefulness of this region in M67 (NGC 2682) in calibrating CCDs is discussed by several authors (Mayya 1991, and references therein). We also observed the standards chosen from the Landolt (1983) in the
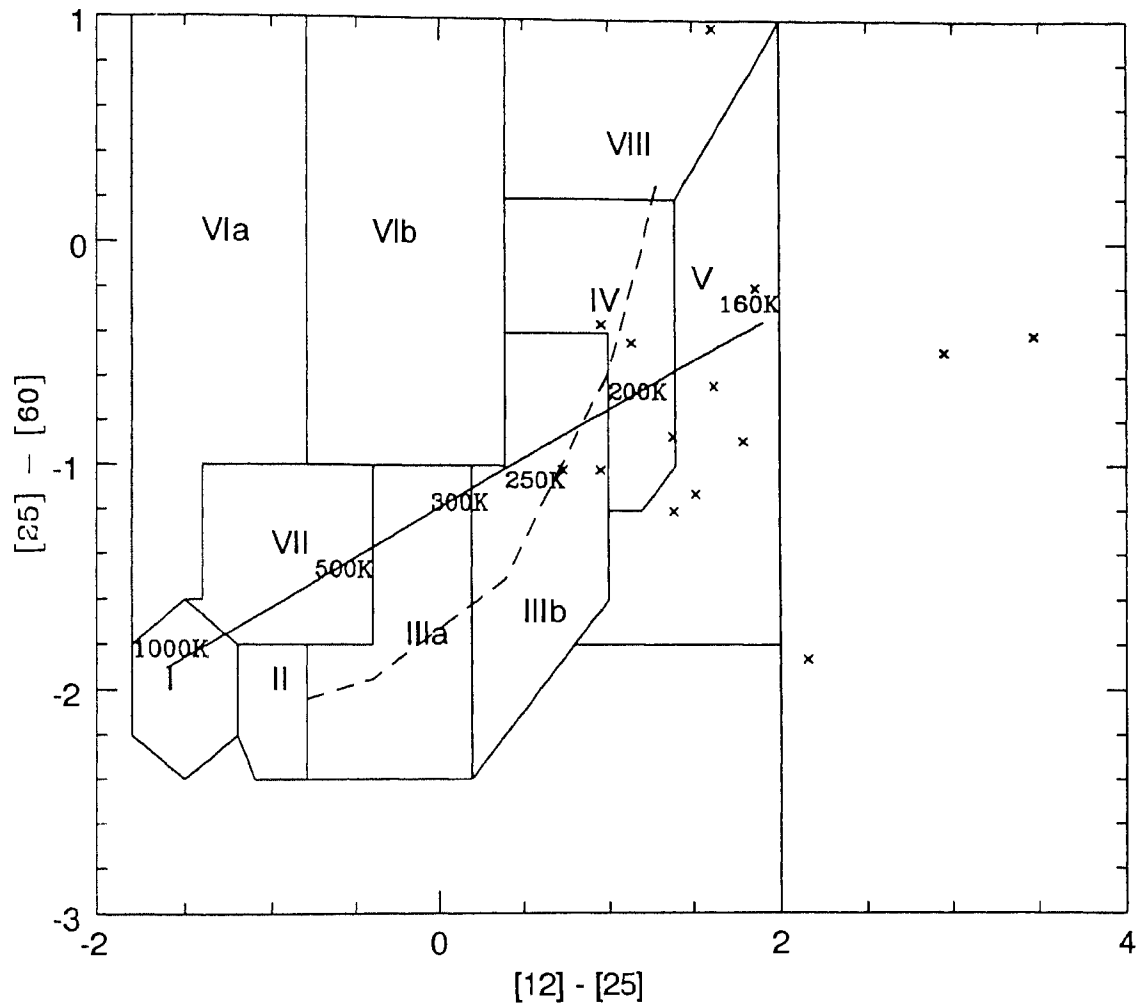
Figure 2.1: *The positions of program IRAS sources in the van der Veen and Habing (1988) IRAS colour-colour diagram. The evolutionary track from MIRAS to OH/IR stars is indicated by dashed line. The vertical line at [12]-[25]=2 is the boundary line of VH diagram (see text). The sources and their corresponding positions in the VH diagram are given in Table 2.6.*

IRAS0426+3429   IRAS05113+1347   IRAS05238-0626   IRAS05341+0852

IRAS06530-0213   IRAS07253-2001   IRAS08143-4406   IRAS08187-1905

IRAS14429-4539   IRAS17086-2403   IRAS17150-3224   IRAS17291-2402

IRAS17441-2411   IRAS23304+6147
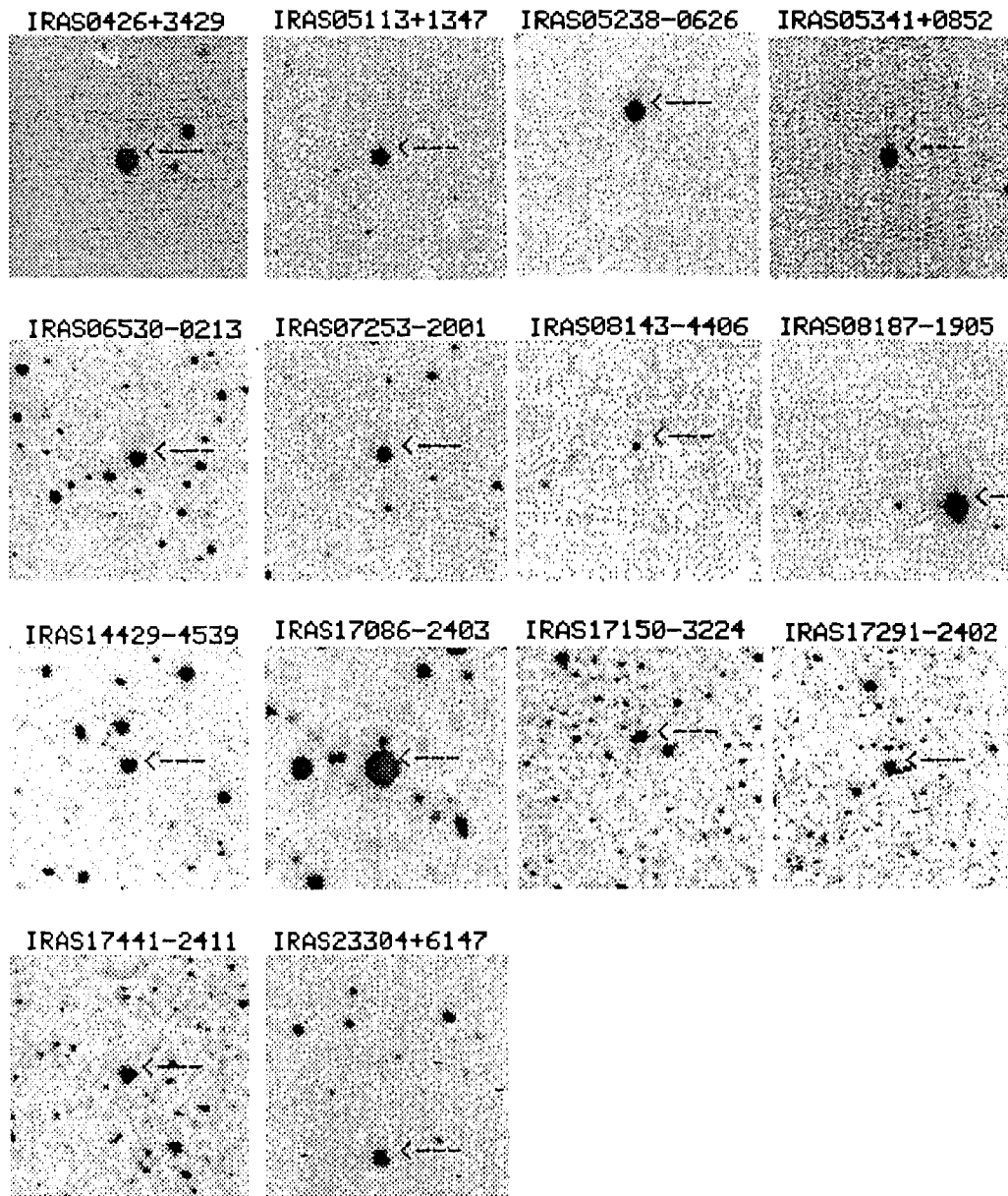
Figure 2.2: Optical identification charts of the IRAS sources. Identifications are marked on CCD frames of V band. The scale of the each figure is $1.5' \times 1.5'$. For all images North is up and East is left.

direction of program stars. We observed one or two standards in all filters every night at different airmass to get the atmospheric extinction coefficients. Flat field images were obtained by exposing CCD to a twilight sky. This was done every night before and after the observations.

These CCD images have been processed using IRAF (Image Reduction and Analysis Facility). The reduction procedure of the images consists of three steps: instrumental calibration, deriving instrumental magnitudes and transforming the derived magnitudes into some standard system.

Instrumental calibration of the images includes, bias subtraction, dark counts removal, fixing the bad pixels on the CCD chip and flat field corrections to the images. This whole image processing is done using single task in IRAF called CCDPROC. Several well exposed twilight flat field images obtained during a single night in each filter are individually debiased and stacked. The resultant flat field image is used in CCDPROC image calibration. The relative detector pixel response is calibrated by dividing by a scaled flat field calibration image. The result of CCDPROC run is the bias subtracted, dark subtracted, flat field corrected and bad pixels free CCD image frame which is linear in pixels.

Instrumental magnitudes are derived from the APPHOT package in IRAF. APPHOT package is a set of tasks for performing aperture photometry on uncrowded or moderately crowded fields. Aperture photometry on the stars, requires the size of the aperture and sky parameters. The size of the aperture has been determined for each star by aperture synthesis method. This involves, computing the magnitudes for a series of smaller apertures (8,10,12,16,18) for each filter and then seeing for which radius the difference in magnitudes is constant. We have taken the width of the sky annulus as 5 pixels throughout out our photometric analysis. We derived instrumental magnitudes for both program stars and standard stars by using the task *phot* in APPHOT package.

The measured magnitudes are corrected for atmospheric extinction using a standard formula

$$m_{\lambda 0} = m_\lambda - (k'_\lambda + k''_\lambda c)X$$

where m_λ is measured magnitude, $m_{\lambda 0}$ is corrected magnitude k'_λ is principal extinction coeffient and k''_λ is the second order coefficient, c is the observed colour index and X is the air mass. The coefficients have been determined using the magnitudes of standard star(s) observed at different air masses. The air mass X in the above equation is determined by a most common polynomial approximation (Hardie 1962)

$$X = secz - 0.0018167(secz - 1) - 0.002875(secz - 1)^2 - 0.0008083(secz - 1)^3 \text{ where}$$

z is the zenith distance.

The extinction corrected magnitudes are transformed to BVRI standard system through the following transformation equations:

$$V = v_0 + \beta_v(B - V) + \alpha_v$$

$$B - V = \beta_{bv}(b - v)_0 + \alpha_{bv}$$

$$V - R = \beta_{vr}(v - r)_0 + \alpha_{vr}$$

$$R - I = \beta_{ri}(r - i)_0 + \alpha_{ri}$$

where, V, B$-$V,... are the magnitudes of standard stars v_0, $(b-v)_0$, ... are extinction corrected measured magnitudes α_v, α_{bv}, ... are the zero-point constants β_v, β_{bv}, ... are the colour coefficients.

The derived BVRI magnitudes of 14 IRAS sources are tabulated in Table 2.2. Near-IR photometric data has been taken from the literature and far-IR fluxes have been taken from IRAS point source catalogue.

2.3.2 Spectroscopy

Low resolution optical spectra of a few bright sources in the sample (Table 2.1) have been taken during observational runs in December 1992 and January 1993. We used the 1.0 m telescope at VBO equipped with a UAGS spectrograph and CCD. Spectra from 4000Å to 6500Å with a resolution of 5.7Å pixel^{-1} were obtained. Low resolution near-IR spectra of several of these sources have also been obtained with the 2.3 m telescope at VBO during November 1993. We have reduced the spectra using a locally developed software program called RESPECT at VBO Kavalur.

Table 2.2: Photometric observations of the program sources

IRAS Name	B	V	R	I	Date of observation.[a]
04296+3429	16.39	14.30	13.10		244,9064.5
	16.20	14.21		11.64	244,7452.5[1]
05113+1347	14.81	12.63	11.46	10.17	244,9006.5
05238−0626	11.04	10.56	10.27	9.91	244,9006.5
	11.01	10.54	10.26	9.97	No date[3]
05341+0852	12.50	11.89	11.47	11.00	244,9006.5
06530−0213	16.23	14.11	12.77	11.46	244,9076.5
	16.43	14.04	12.74	11.40	1989 March[2]
07253−2001	13.79	12.90		11.80	244,9006.5
08143−4406	14.14	12.37	11.65	10.61	244,9005.5
08187−1905	9.53	8.85	8.35	8.09	244,9005.5
14429−4539	14.28	13.49	12.89	12.10	244,9100.5
	14.45	13.39	12.64	12.18	244,9076.5
	14.39	13.54	12.92	12.17	1989 March[2]
17086−2403	12.67	11.80	11.40	11.00	244,9100.5
17150−3224	16.26	14.55	13.55	12.46	244,9064.5
	16.10	14.54	13.60	12.69	1989 March[2]
17291−2402	15.29	14.08	13.40	12.66	244,9076.5
17441−2411	15.06	13.35	12.26	11.21	244,9076.5
23304+6147	15.8	13.5	12.5	10.8	244,9005.5
	15.37	13.06		10.43	244,7452.5[1]
	15.52	13.15	11.79	10.50	244,7762.5[1]

Note: Errors in magnitudes: B:±0.1; V,R,I: ±0.05

1. Hrivnak and Kwok 1991, 2. Hu et al 1993

3. Torres et al 1995

a. in Julian date
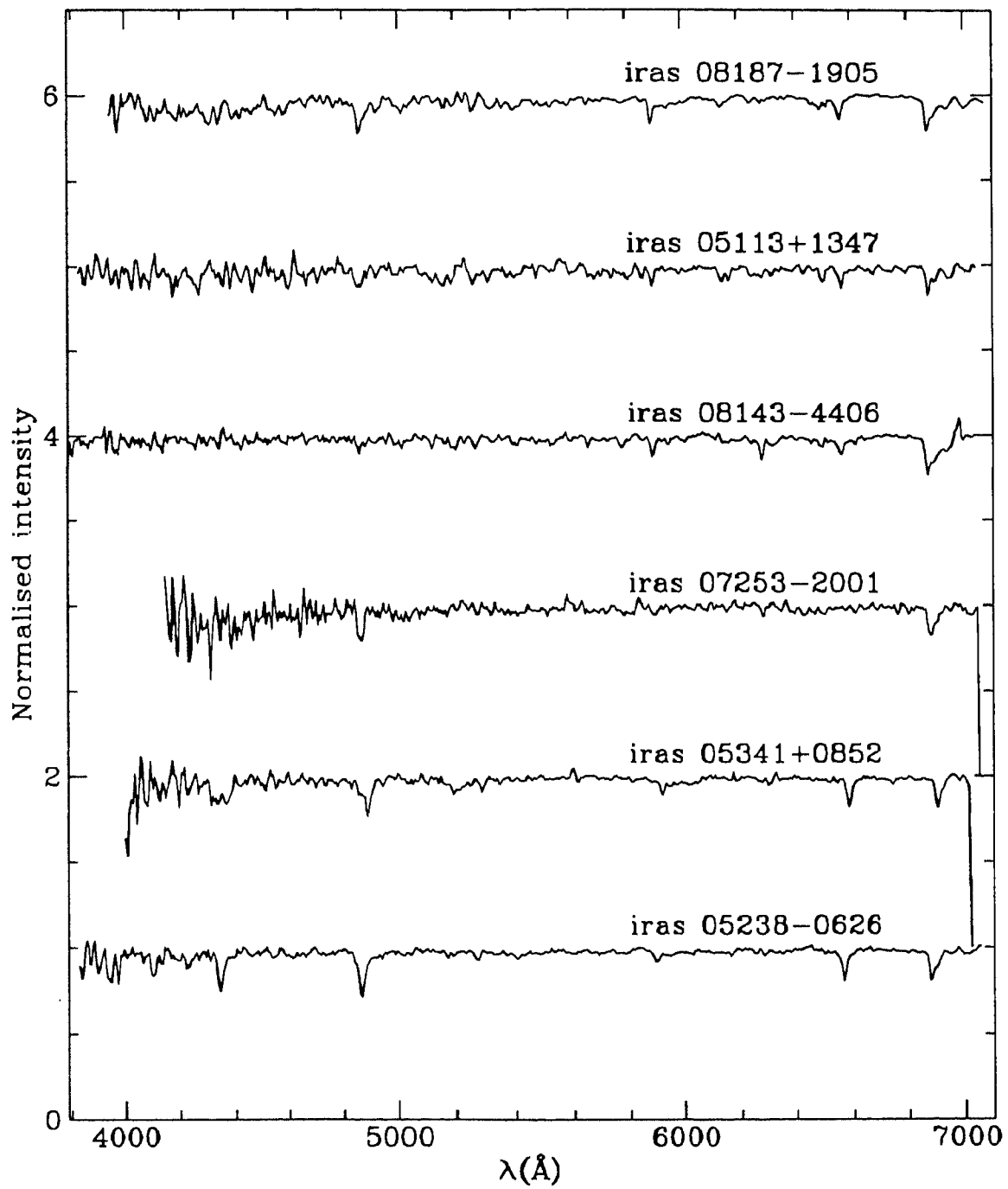
Figure 2.3: *Normalized low-resolution optical spectra of some of the sources*
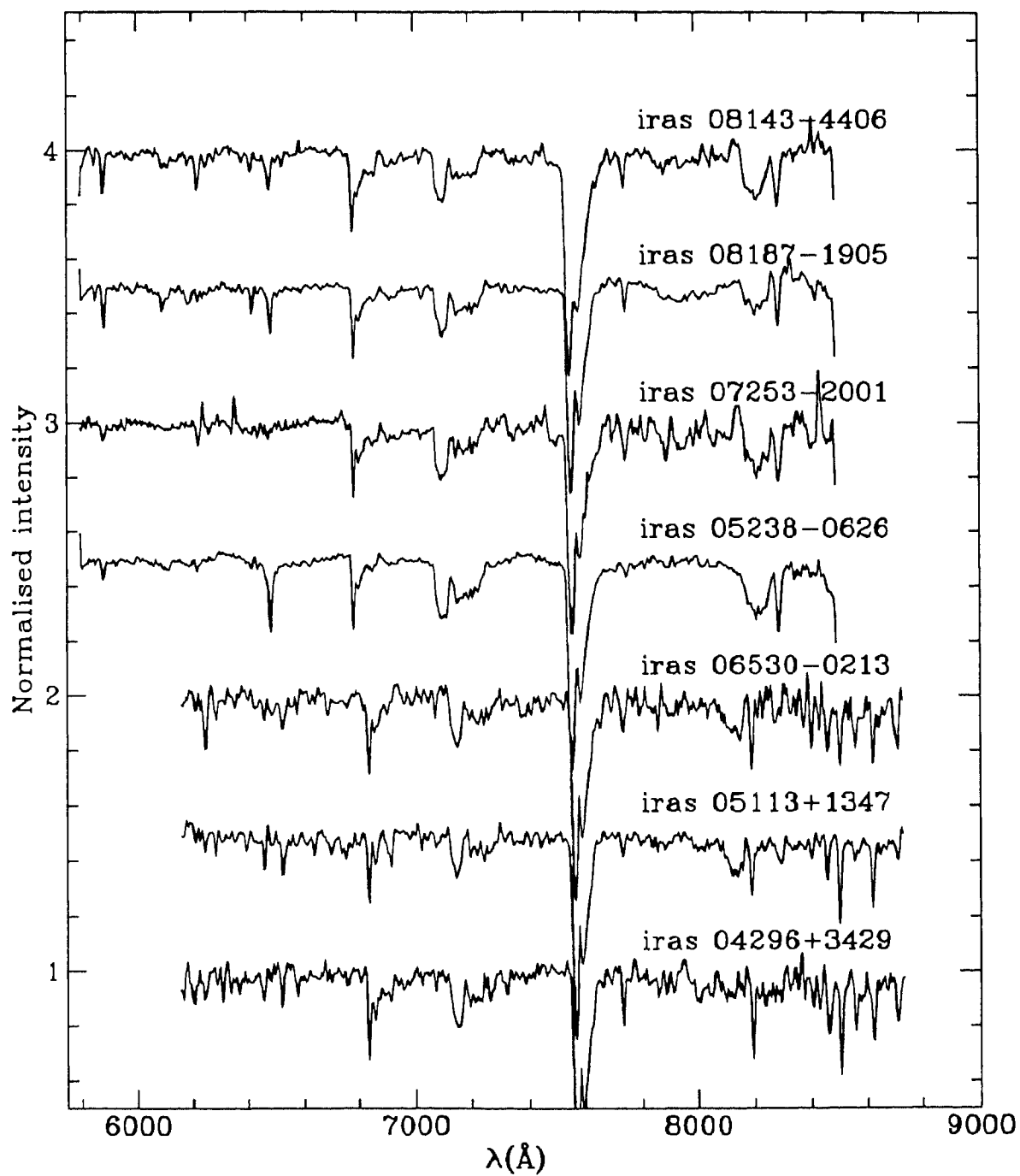
Figure 2.4: *Normalized low-resolution red spectra of few fainter sources*

Table 2.3: Spectral types and luminosity classes as derived from optical and near-IR spectra of few sources

IRAS Name	optical spectrum	NIR spectrum	Date of obs.
IRAS 04296+3429	-	F5I	244,9328.5
IRAS 05113+1347	G3I	G5I	244,8996.5
IRAS 05238−0626	F2II		244,9199.5
IRAS 05341+0852	F6I		244,9199.5
IRAS 06530−0213	-	F0I	244,9328.5
IRAS 07253−2001	-	F5I(e)	244,9199.5
IRAS 08143−4406	F8I	-	244,9199.5
IRAS 08187−1905	F6I	F5I	244,8995.5

2.4 Analysis

2.4.1 Spectral classification

We used both optical and near-IR spectra for spectral classification. In order to compare and classify the objects we obtained spectra of several bright standard stars with the same instrumental setup. We have also used the optical spectra of standard stars compiled by Jacoby et al (1984) for this purpose. The near-IR spectra of program stars have been compared with the spectra of bright standard stars obtained by us and also with the near-IR spectra of several stars given by Torres Dodgen and Bruce Weaver (1993). The near-IR spectral classification agrees well with the optical classification except for IRAS 04296+3429. We classified this star as an F5 supergiant based on the near-IR spectra; Hrivnak (1995) classified it as a G5 supergiant based on the spectrum in the blue region. It is to be noted here that we made use of spectra of normal population I stars to classify the spectra of program stars. Some of the sample stars may be slightly metal-poor and therefore spectral types assigned may be a bit earlier. The spectral types and luminosity classes of 8 stars have been

reliably estimated and are listed in Table 2.3. We could get spectra of only 8 stars within the allotted observing time. Several of our program stars are fainter than 13 th magnitude and the sky conditions during our observing run were not favorable and hence we ended up with spectra of eight program stars. The optical and NIR spectra of program stars have been displayed in Fig.2.3 and Fig.2.4 respectively.

2.4.2   Observed flux distribution

The observations of the sources in the various wavelength regions (0.4 μm to 100 μm) were combined to study their energy distributions (Fig.2.5). The near-IR photometry of the sample objects (Table 2.1) has been taken from the studies of Manchado et al (1989) and Garcia-Lario et al (1990). In order to compare the energy distribution of the program stars with model atmospheres we have to correct the observed fluxes for interstellar reddening. The optical and near-IR fluxes have been corrected for interstellar reddening.   We estimated the reddening in the direction of these objects from the work of Burstein and Heiles (1982) and Neckel and Klare (1980). We also estimated interstellar reddening from O- and B-type stars which are in the direction of program stars. We have used both the bright (nearby) and faint (distant) O and B stars, to minimize the effect of distance on the reddening. The estimated average extinction values A_V have been tabulated in Table 2.4. Using these values, the BVRI and near-IR magnitudes have been corrected for interstellar extinction using the average extinction law of Cardelli et al (1989). The flux distribution of stars are compared with the Kurucz (1979) atmospheric models which are shown in Fig.2.5. It is clear from Fig. 2.5 that all the stars have far-IR excess.

2.4.3   Stellar temperatures, gravities, luminosities and distances

The effective temperatures and gravities are estimated from the observed energy distribution fits with the Kurucz model atmospheres with solar metallicity. The models were fitted to three wavelength regions: optical, near-IR and far-IR. The model atmospheres of different metallicities differ considerably only in the UV part
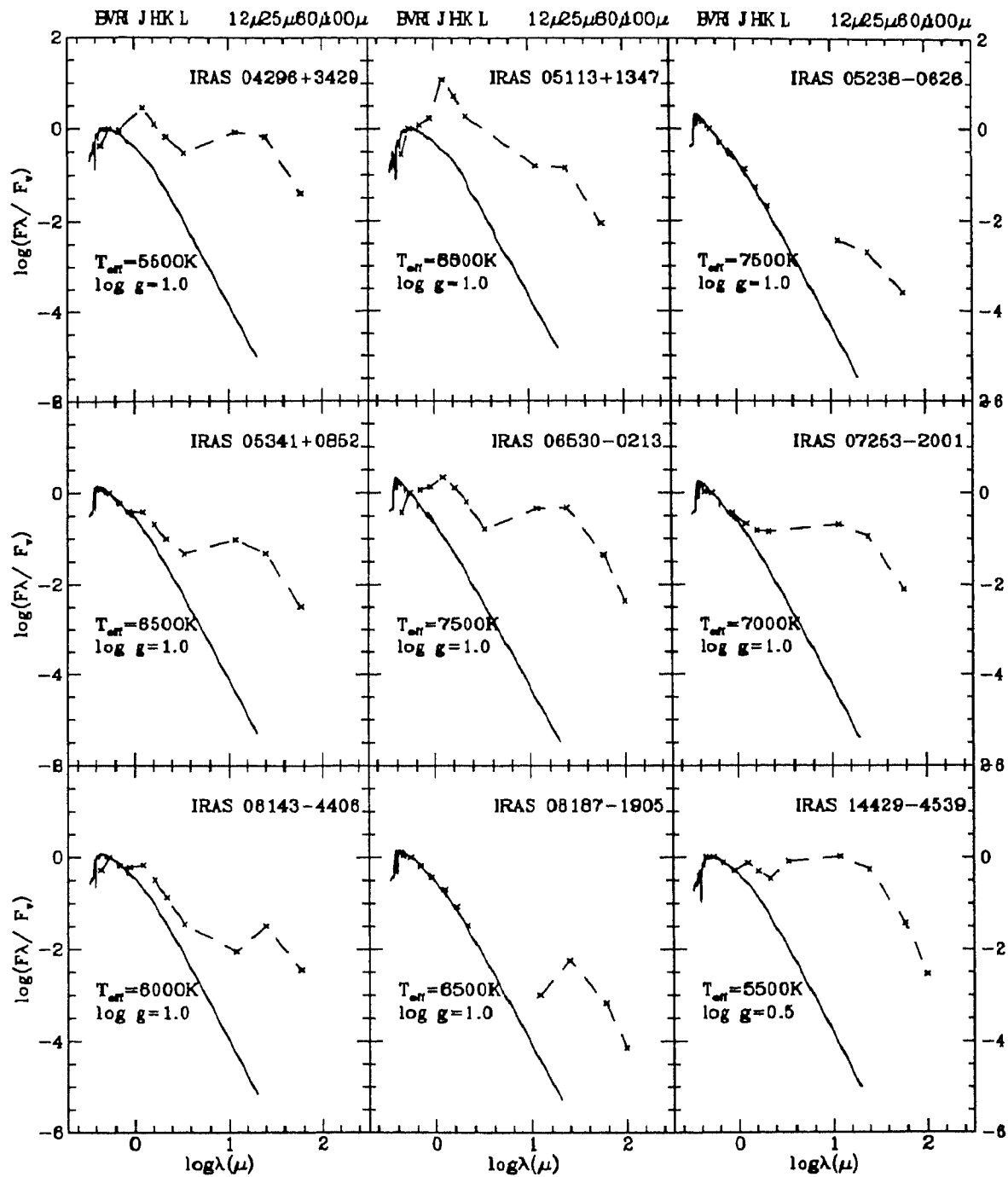
Figure 2.5: *Spectral enery distribution of program stars showing the presence of both hot and cold dust components. The sources IRAS 05233—0626, IRAS 17086—2403 and IRAS 08187—1905 have only cold dust. The full line indicates the Kurucz model with the parameter given in the figures.*

BVR J HK L   12μ25μ60μ100μ   BVR J HK L   12μ25μ60μ100μ   BVR J HK L   12μ25μ60μ100μ

IRAS 17086-2403

T_{eff}=9500K
log g=1.0

IRAS 17150-3224

T_{eff}=5000K
log g=1.0

IRAS 17291-2402

T_{eff}=6000K
log g=1.0

$\log \lambda (\mu)$

IRAS 17441-2411

T_{eff}=9000K
log g=1.0

IRAS 23304+6147

T_{eff}=5000K
log g=1.0

$\log(F\lambda / F_{\nu})$

$\log \lambda (\mu)$ $\log \lambda (\mu)$
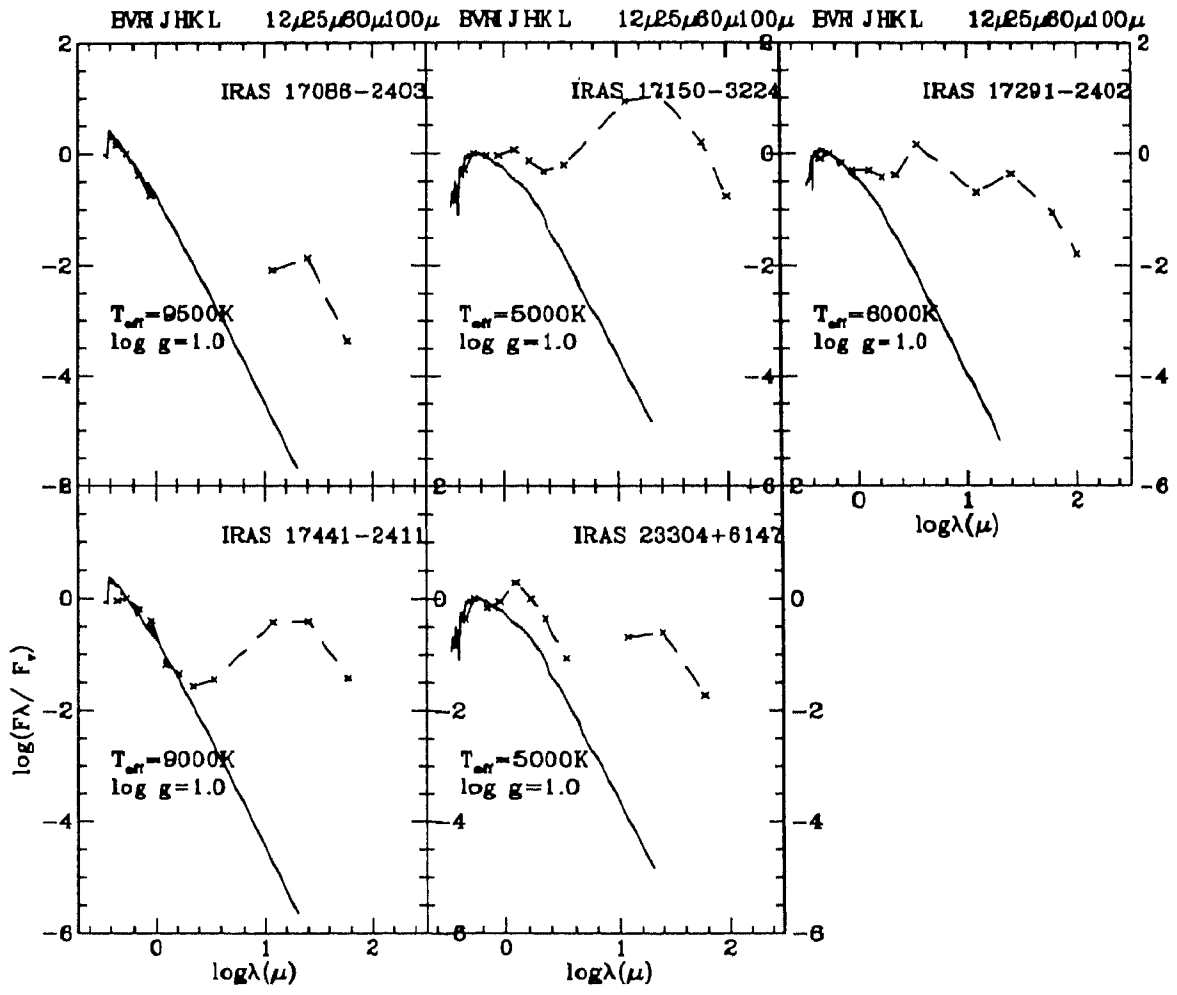
Fig 2.5 continued

Table 2.4: Temperatures and fluxes of stars and their dust envelopes

IRAS Name	T_{eff} (K)	log g	B-V	A_v	T_d (K)	f_{opt}	f_{fir} $\times 10^{-12}$ W m^{-2}	f_{ir}/f_{opt} $\times 10^{-12}$ W m^{-2}
04296+3429	5500	1.0	2.09	1.6	160	0.137	7.136	50.0
05113+1347	5000	1.0	2.18	0.4	145	0.188	2.36	12.5
05238−0626	7500	1.0	0.48	0.6	143	3.846	0.296	0.08
05341+0852	6500	0.5	0.61	0.4	200	0.804	1.643	2.04
06530−0213	7500	1.0	2.12	1.2	145	0.184	4.269	23.20
07253−2001	7000	1.0	0.89	0.9	210	0.563	2.495	4.43
08143−4406	6000	1.0	1.77	1.2	115	0.651	1.386	2.13
08187−1905	6500	1.0	0.68	0.3	110	11.374	2.614	0.23
14429−4539	5500		0.89	0.6	200	0.213	5.504	25.84
17086−2403	9500	1.0	0.87	1.9	140	3.907	1.701	0.44
17150−3224	5000	1.0	0.87	0.9	150	0.066	50.076	758.7
17291−2402	6000		1.21	0.9	140	0.132	3.076	23.30
17441−2411	9000		1.71	2.8	150	1.555	29.76	19.14
23304+6147	5000	1.0	2.3	2.8	135	0.485	8.99	18.54

of the spectral domain which is sensitive to the metallicity. Since the optical fluxes are from the broad band photometry, and the low dispersion spectra of some of these sources do not indicate significant underabundance of metals, we have used Kurucz model atmospheres with solar metallicity. The IR part of the energy distribution is not very sensitive to metallicity. From Fig.2.5 it is seen that for several stars, model fits are satisfactory atleast in the optical part of the energy distribution. In the case of a few stars (see Fig.2 5), large deviations of observed flux distribution from the models may be due to unaccounted interstellar and/or circumstellar reddening.

Since all the stars considered here are IRAS sources and have circumstellar envelopes, deducing stellar parameters T_{eff} and log g from the model fits are largely hampered by the reddening caused by both interstellar medium and circumstellar

envelopes. Determination of extinction due to the dust around the stars is difficult as there are no accurate extinction laws which satisfy the dust environment of individual stars. The probable errors T_{eff} and log g determinations are of the order of $\pm$ 500 K and $\pm$ 0.5 respectively.

For stars which have spectral types and luminosity classes (Table 2.3), we estimated temperatures from spectral type vs T_{eff} calibration for supergiants (Flower 1977). Stellar surface gravities are taken from luminosity vs gravity tables (Landolt and Börnstein 1982). Deriving gravities from the low resolution spectra is difficult, but the supergiant character of the spectra of the sources indicate that they have low-gravity atmospheres. The stellar T_{eff} and log g values derived from the spectra of IRAS 05238−0626, IRAS 05341+0852, IRAS 07253−2001, IRAS 08187−1905 and IRAS 17086−2403 are in good agreement with the values derived from the model fits. The derived T_{eff} and gravities are presented in Table 2.4.

Since the distances (d) to these sources are not known, it is difficult to determine the luminosities for these stars. The spectral class vs absolute magnitude tables (Landolt-Börnstein 1982) yield values of $M_V \approx$ −6.6 which is very large and valid for the population I supergiants. The stars considered here all have circumstellar envelopes with far-IR colours typical of post-AGB stars and proto-planetary nebulae. In most of the stars in our sample CO or OH molecular features have been detected which are normally found in the expanding envelopes of evolved low-mass stars such as post-AGB stars and proto-planetary nebulae. The summary of molecular observations of these stars is given in Table 2.6. Since all these sources are post-AGB stars, we assume that they may have a core mass of $M_c \approx 0.6$ $M_\odot$. The core mass M_c=0.6 $M_\odot$ is typical of observed white dwarfs and central stars of PNe.

The post-AGB stars evolve from the tip of the AGB to planetary nebulae with constant luminosity, but with increasing surface temperature and decreasing radii (Schönberner 1983; Blöcker 1995). The central stars are still burning hydrogen in a thin shell just outside the stellar core. The stellar envelope mass is still large enough ($M_e > 10^{-4} M_\odot$) to ensure that the evolution of the core and envelope are decoupled and the core mass-luminosity relation (Wood and Zaro 1981) is applicable. Using the core mass-luminosity relation, with core mass of 0.6 $M_\odot$ we get stellar luminosity

$L_* = 10^{3.79} L_\odot$. The post-AGB tracks calculated (Blöcker 1995) for the core mass $M_c = 0.6$ M$_\odot$ also gives approximately the same luminosity.

The luminosity $\log (L_*/L_\odot)$ =3.79 corresponds to an absolute magnitude $M_V = -4.75$. The distance estimates by distance modulus method demand knowledge of total extinction caused by dust and the interstellar medium (A_v). Using the A_v values given in Table 2.4 , we arrive at very large values for distances. The presence of dust around these sources makes the stars appear fainter and hence the large distances. To minimize the effect of dust in estimating the distances we proceeded as follows: we determined total excess E(B-V) using observed (B-V) and the intrinsic colours $(B-V)_o$ as derived from the spectra. Since the extinction law for dust shells are not known, we assumed the interstellar extinction law for dust shells also. We applied the extinction constant R=3.1 for both interstellar and dust shells. For stars having both hot and cold dust shells the values of d may be too large especially in the case of IRAS 14429−4539, IRAS 17150−3224 and IRAS 17291−2402. However for stars having cold detached dust shells, this approximation gives reasonable distance estimates. The total extinction values A_{vtot} used in the distance estimates and derived distances are given in Table 2.5. The stellar radii are estimated using the relation $L = 4\pi R_*^2 \sigma T^4$ and the values R_* are tabulated in Table 2.5. The uncertainties in the derived stellar radii are subject to the uncertainties in the T_{eff} and the assumed luminosity.

We estimated the total optical fluxes (f_{opt}) by integrating the fluxes from 0.34 μm to 0.9 μm and the total far-IR fluxes (f_{fir}) by integrating fluxes from 12 μm to 100 μm. The f_{opt} , f_{fir} and the ratio f_{fir}/f_{opt} are presented in Table 2.5. For most of the sources the ratio $f_{fir}/f_{opt} > 1$ suggesting that all these sources are emitting most of their energy in far-IR.

2.4.4 Dust envelope parameters

Temperatures, masses, radii, dynamical ages and mass-loss rates of dust envelopes are estimated as follows:

The dust temperatures (T_d) have been estimated assuming black body distribution using the IRAS fluxes. We accepted the dust temperature for which the deviation

Table 2.5: Derived stellar and dust envelope parameters IRAS sources .

IRAS Name	A_{vtot}	d	Z	$R_\star$	R_d	M_d	t_{dyn}	$\dot{M}\times10^{-7}$
		(kpc)	(pc)	($R_\odot$)	($\times10^5 R_\odot$)	($\times10^{-4}M_\odot$)	(yr)	$M_\odot yr^{-1}$
IRAS04296+3429	3.0	5	0.8	119	2.0	5.9	400	5.1
IRAS05113+1347	4.3	5	1.2	105	2.6	2.5	550	4.6
IRAS05233−0626	1.0	7	2.6	47	2.8	1.2	700	2.0
IRAS05341+0852	0.5	10	2	54	1.1	4.0	300	2.7
IRAS06530−0213	6.1	3	0.0	43	2.6	2.0	350	1.8
IRAS07253−2001	2.1	10	0.2	54	1.0	5.7	250	2.0
IRAS08143−4406	4.0	4	0.4	68	4.8	3.0	1100	3.0
IRAS08187−1905	1.1	3	0.5	54	5.5	3.9	1300	2.3
IRAS14429−4539	0.1	6	1.2	87	1.09	5.0	252	3.8
IRAS17086−2403	3.6	6	1	29	4.1	1.6	800	1.2
IRAS17150−3224	3.0	<18	0.9	105	2.4	<1545	490	4.6
IRAS17291−2402	2.0	< 23	0.9	73	2.9	<246	642	3.2
IRAS17441−2411	6.0	2.5	0.1	32	2.4	11	660	1.2
IRAS23304+6147	4.4	5	87	105	4.9	21	1900	4.5

between the observed and calculated fluxes are minimum as judged by χ^2 test. The derived dust temperatures are given in Table 2.4. The radii of dust envelopes are estimated by equating grain heating by photon absorption with cooling by photon emission. The energy balance equation between the radiation from the star $(4\pi R_\star^2 \sigma T_\star^4)$ and dust envelope $(4\pi R_d^2 \sigma T^4 Q(a,T_d))$ is given by

$$R_\star^2 T_\star^4 = R_d^2 T_d^4 Q(a, T_d) \tag{2.1}$$

where $Q(a,T_d)$ is an average efficiency of dust emission for a given T_d and dust grain size, a=1 μm. The values of Q ($Q/a \approx 0.13 - 0.5 \ \mu m^{-1}$) are taken from the calculations of Drain and Lee (1984). Here dust absorption coefficient is taken as 1, with the assumption that total star light is intercepted by dust. However this assumption may not be true if the dust shell is in the form of a disk. Dust masses

are computed using the formulae given by Barlow (1983) and Hilderbrand (1983) and using the 60 μm flux and the derived T_d

$$M_d = \frac{4a\rho d^2 F_\nu}{3QB_\nu(T_d)} \tag{2.2}$$

where ρ is the grain density, d is distance to the source, F_ν is the observed IRAS flux and $B_\nu(T_d)$ is a black body function for given dust temperature. We have used $a\rho/Q=0.013$ gm cm^{-1} which is typical for interstellar dust grains (Drain and Lee 1984). This procedure provides only an estimation for the total mass, since a single temperature and of uniform chemical composition are assumed for grains. The estimated dust envelope masses (Table 2.5) are in the range 10^{-3} to $10^{-4}M_\odot$ except for IRAS 14429−4539 and IRAS 1715−3124 which have large dust masses of around 10^{-2} M$_\odot$.

We next determined the dynamical ages for the post-AGB stars considered here. The dynamical age is the travel time from the dust condensation radius (R_c) to the present radius. We used here the approximate solution of equation of motion for steady radial flow given by van der Veen et al (1989)

$$t_{dyn} = 1.73 \times 10^3 (\frac{L_\star}{5000L_\odot})^{0.5}(\frac{T_\star}{10^4K})^{0.5}(\frac{T_d}{100K})^{-2.5} \times (\frac{V_\infty}{15kms^{-1}})^{-1}yr \tag{2.3}$$

This relation assumes that only radiation pressure and gravity are important and $R_d/R_c > 100$ and $T_d < 200$ K. The expansion velocities V_∞ are either obtained from the CO or OH observations (see Table 2.6) or assumed to be equal to 15 km s^{-1}. The estimated values are given in Table 2.5. The derived results are subject to the uncertainties in the assumed luminosity and derived dust and stellar temperatures. The derived dynamical ages for our sample range from 250 years to 2000 years.

We estimated the present day mass-loss rates for the program stars, according to the Reimers (1975) approximated formula:

$$\dot{M}_R = 5 \times 10^{-8}\eta(\frac{L_\star}{5000L_\odot})^{1.5}(\frac{T_\star}{10^4})^{-2}(\frac{M_\star}{M_\odot})^{-1}M_\odot yr^{-1} \tag{2.4}$$

where η is taken equal to unity and $M_* = 0.6 M_\odot$. Though Reimers mass-loss formula cannot account for the large mass loss rates observed on the AGB ($\approx 10^{-4} M_\odot$ to $10^{-6} M_\odot$ yr^{-1}), it still gives reasonable mass-loss rates for low pulsational period stars (Blöcker 1995). The very low IRAS variability index (Table 2.1) for our program stars justifies the use of this simplified formula. The estimated mass-loss values are given in Table 2.5. All the stars have mass-loss rates of the order of $10^{-7} M_\odot yr^{-1}$. The uncertainties in the derived mass-loss rates are subjected to uncertainties in the assumed luminosity and stellar mass and in the estimated T_*.

2.5   Discussion

Based on the spectral energy distribution, the sample of program stars are put into two groups. The sources IRAS 08187−1905, IRAS 05238−0626 and IRAS 17086−2403 present similar flux distributions. All three sources have only cold dust components, detached from the central stars with dust radii $R_d \approx 1000$ R_*. The low infrared variability for all the three sources suggests that these stars have left the AGB. The association of these sources with bright optical candidates, may be due to the thining of the dust envelopes. It may be possible that as the dust shell expands and is diluted, it may lead to higher excitation temperature in the dust because of high effective temperature. At a certain stage the dust shell reaches a level when it cannot sustain the OH and CO molecular emission features. This is consistent with at least one source IRAS 17086−2403, in which OH and CO molecular features are not detected (te Lintel Hekkert et al 1991). Ratag et al (1991) detected 6 cm radio continuum emission in this source which is generally seen in planetary nebulae and proto-planetary nebulae shells. Radio continuum emission is due to thermal bremsstrahlung in a (partially) ionized gas. Radio continuum is detected in very low-excitation PNe (Pottasch 1987). Garcia-Lario and Parthasarathy (1996) obtained optical and ultraviolet spectrum of IRAS 17086−2403. They detected nebular emission lines in the optical spectrum indicating that it is a low excitation PN, which is in agreement with the detection of 6 cm radio emission by Ratag et al. All three sources are at high galactic latitude (l>9°) suggesting that these are old low-mass evolved stars (Parthasarathy and Pottasch

1986). The IRAS colours of these three objects indicate very cold dust shells and all these objects fall out of the range of van der Veen and Habing (VH) (1988) IRAS colour-colour diagram. However in the IRAS colour-colour diagram of Likkel et al (1991) these sources fall in the region where most of the stars are evolved stars and PNe but without CO detection. The far-IR excess, non-variability and high latitude of these objects suggest that these are post-AGB supergiants, slowly evolving towards planetary nebula phase.

The rest of the sources in the sample present a double peak energy distribution (Fig.2.5). One peak represents the stellar emission , obscured by optically thin hot dust component and the other is produced by the reemission in the far-IR of the stellar radiation obscured by the dust envelope. The presence of hot and cold dust components suggest that there was a discontinuity in the mass-loss history. A possible cause for such discontinuity may be periodic thermal pulsations predicted for the AGB model stars (Iben and Renzini 1983). The clear separation between maxima, the cool outer dust shell and low IR variability indicate that the dust shell is far away from the central star and the intense mass-loss processes are not active now. Observations indicate that the mass-loss rates of central stars of planetary nebulae are up to several orders of magnitude below that of the immediately preceding AGB evolution (Perinotto 1989). Therefore, mass-loss has to decrease strongly during the transition between the AGB and the PNe. The mass-loss values given in Table 2.5 are almost two orders less than that of the typical mass-loss rates of few$\times 10^{-4} M_\odot$ yr^{-1} on the AGB phase.

Most of the sources in this second group are classified as carbon-rich based on the infrared properties of their dust envelopes (Omont et al 1993). The carbon-rich dust envelopes imply the overabundance of carbon in the photospheres, which suggest that these stars have undergone third dredge-up which occurs in the advanced phase of AGB evolution of low and intermediate-mass stars (Iben and Renzini 1983) Eight out of the eleven sources in this group are identified with having at least one of the molecular carbon features, for example, in IRAS 23304+6147 and IRAS 04296+3429 CO, HCN and 21 μm emission features are detected (Woodsworth et al 1990; Loup et al 1993)). The strong unidentified emission feature at 21 μm is not seen in PNe

Table 2.6: Molecular observations of program stars. VH is the star's position in the van der Veen and Habing (1988) colour-colour diagram.

IRAS Name	CO	V_{exp}	OH	HCN	3.3μ	21μ	Chem. Type	VH(region)	Ref
05238−0626								IV	
08187−1905								-	
17086−2403	No		No					-	h
04296+3429	Yes	15.6	No	Yes	Yes	Yes	Carbon	V	a,c
05113+1347	...	...	...	...	Yes	Yes	carbon	V	f
05341+0852			No		Yes	Yes	carbon	IIIb	g
06530−0213	Yes	31	No				carbon	IV	b
07253−2001								IIIb	
08143−406								-	
14429−4539	Yes	18.2	No					IIIb	b
17441−2411	Yes		No					V	
23304+6147	Yes	15.5	No	Yes		Yes	carbon	V	a,c
17150−3224	Yes		Yes					V	e
17291−2402								VIII	d

(a) Woodsworth et al 1990; (b) Loup et al 1993;(c) Kwok et al 1989

(d) Likkel et al 1991; (e) Hu et al 1993b;(f) Hrivnak et al 1994

(g) Geballe et al et al 1992; (h) te Lintel Hekkert et al 1991

and AGB stars, but only in post-AGB stars (Kwok 1993). In IRAS 17441−2411, IRAS 06530−0213, IRAS 05113+1347 and IRAS 14429−45389 CO molecular feature has been identified (Omont et al 1993 and references therein). In IRAS 05341+0852 and IRAS 04296+3429 an unidentified 3.3 μm molecular feature has been detected (Geballe and van der Veen 1990) which is generally attributed to Polycyclic Aromatic Hydrocarbons (PAH). In none of these sources OH has been detected. This may be because all these sources are carbon-rich, or the decreased mass-loss rate has reduced the OH- density below that required to sustain an OH maser (Sun and Kwok 1987). Lack of OH and low far-IR variability index (Table 2.1) are consistent with the reduced mass-loss (Likkel et al 1991). Most of these sources fall in the region V of VH IRAS colour-colour diagram. This region is characterized by stars which are non-variable and perhaps are in the transition phase between AGB and PNe. The carbon-rich dust envelopes and non-variability of these sources suggest that these stars are in the post-AGB stage of evolution.

2.5.1 Description of individual sources

IRAS 04296+3429:

This object has been classified as a carbon-rich G0 supergiant using the blue part of the spectrum (Hrivnak 1995). We classified this object as F5I based on our red spectrum. We use the spectral type derived by Hrivnak, as his spectral resolution is superior to ours. The double peak energy distribution similar to IRAS 06530−0213 suggests the presence of two dust components, cold and hot. The photometric magnitudes B and V derived by Hrivnak and Kwok (1991) are in good agreement with our photometric values. The distances 3.6 kpc and 4.2 kpc estimated by Kwok et al (1989) and Omont et al (1993) respectively are slightly less than the distance 5 kpc derived from our analysis. This may be due to the uncertainties involved in estimating the reddening due to interstellar medium and circumstellar envelope. The characteristics of the dust envelope and the detection of CO, HCN, 3.3 μm and 21 μm (Table 2.6) emission features indicate that IRAS 04296+3429 is a carbon-rich post-AGB F-G type supergiant.

IRAS 05113+1347:

This is a G type supergiant of magnitude V =12.63. It has large near-IR and far-IR excesses. IRAS 05113+1347 has rising flux at 0.55 μm which reaches peak at 1.25 μm. The large near-IR excess may be due to the thick hot dust component closer to the photosphere of the star. The large value of E(B-V)=2.0 may be due to circumstellar dust. Recently Hrivnak (1995) has studied the spectra of this source and found strong C2 and C3 absorption features. The large near-IR and far-IR excess, presence of 3.3 μm and 21 μm molecular features (Table 2.6), the high galactic latitude (-14°) and the spectral type of G3I suggest that it is carbon-rich post-AGB supergiant similar to IRAS 04296+3429.

IRAS 05238−0626:

This is a high galactic latitude (-21°) F2 supergiant having far-IR excess. The Kurucz model of T_{eff}=7500 K and log g=1.0 fits very well with the 0.44 μm to 4 μm energy distribution. The T_{eff}=8000 K derived from near-IR fluxes (Garcia et al 1990) agrees with our spectral classification of F2II. The star has only cold dust component similar to IRAS 08187−1905. The BVRI magnitudes derived recently by Torres et al (1995) suggest that there is no variation in the IRAS 05238−0626 brightness (Table 2.3).

IRAS 05341+0852:

This star has an optical counterpart of magnitude V =12.63. This has been classified as F6 supergiant based on both optical and near-IR spectra. The energy distribution of IRAS 05341+0852 has been compared with the Kurucz model of T_{eff}=6500 K and log g=1.0. The slight deviation of flux distribution from 1 μm to 4 μm from the model fluxes (Fig.2.5), suggests that the star has optically thin hot dust component. Geballe and van der Veen (1990) have discovered 3.3 μm emission feature which is generally found in carbon-rich PNs and post-AGB stars (Geballe et al 1992). The presence of 3.3 μm and 21 μm (Table 2.6) emission features suggest that IRAS 05341+0852 is a carbon-rich post-AGB F supergiant.

IRAS 06530−0213:

This source is a F0 supergiant of magnitude V =14.11. Within the uncertainties, our

BVRI photometry of this source agrees well with the photometry of Hu et al (1993a). We also confirm the spectral class of F0I estimated by Hu et al. The IRAS colours place the star in box IV of IRAS colour-colour diagram. The stars in this box are typically stars at the end of their mass-loss phase and have very thick oxygen-rich circumstellar shells. The photometry of this object taken in two epochs does not indicate any variability. This object has large reddening E(B-V)=1.5, which might have been affected by unaccountable reddening near the galactic plane as the star is near the plane of the Galaxy. The characteristics of the dust envelope, spectral type and presence of CO molecular emission suggest it is a post-AGB F supergiant.

IRAS 07253−2001:

This star has $H\alpha$ filled in emission. This source has been classified as F5 supergiant based on its red spectrum. The flux distribution from 0.44 μm to 0.9 μm fits with T_{eff}=7000 K and log g=1.0. The shape of the energy distribution from 1 μm to 100 μm (Fig.2.5), suggests the presence of warm and cold dust shells. In the van der Veen and Habing (1988) IRAS colour-colour diagram this source is in box IIIb which is characterized by stars having increasing mass-loss rates.

IRAS 08143−4406:

We classify this star as F8I from its optical spectrum. The energy distribution of IRAS 08143−4406 indicate that it has optically thin hot dust component in addition to cold dust component similar to IRAS 05341+0852. This star has been surveyed for radio continuum emission (Van de steen and Pottasch 1993) and is found negative detection.

IRAS 08187−1905: This IRAS source is associated with a F6 supergiant of V =8.86. The flux distribution between 0.44 μm and 3.4 μm fits very well with the Kurucz atmospheric model of T_{eff}=6500 K and log g=1.0. The T_{eff}=6300 K derived from the T_{eff} and V-I relation (Jones et al 1995) is in good agreement with the above result. Recently Garcia et al (1990) from the near-IR photometry indicated that this star may be a main sequence star or a giant. But from our spectra, we classified this object as F6I. This has been confirmed from our analysis of high resolution spectra. It has very narrow Balmer profiles typical of low gravity stars. The detailed

spectroscopic analysis of this candidate will be published elsewhere.

IRAS 14429—4539:

This object has been classified as a G0 supergiant by Hu et al (1993a). The flux distribution of this candidate indicates that it has cold and hot dust shells. CO molecular emission has been detected by Nyman et al (1992). The average BVRI magnitudes (Table 2.2) obtained by us are in good agreement with Hu et al (1993a). The estimated distance of the star from its V =13.49 and $M_V = -4.7$ and E(B-V)=0.1 is approximately 35 kpc which is very large. However Loup et al (1993) infers distance of 6kpc from molecular observations.

IRAS 17086—2403:

This IRAS source is associated with an optical candidate of magnitude V =11.8. The BVRI fluxes very well fits with the T_{eff}=9500 K and log g=1.0. The T_{eff}=9500 K corresponds to spectral type of A2. The V-I colour of the star after reddening correction corresponds to a temperature of around T_{eff}=9500 K (Jones et al 1995).

IRAS 17150—3224:

This IRAS source is a cold bi-polar proto planetary nebula which has been studied by Hu et al (1993b). The BVRI photometry of Hu et al (1993a) taken in 1989 agrees with our photometry taken in 1993, showing no evidence for brightness change.

IRAS 17291—2402:

This IRAS source is associated with an optical candidate of magnitude V =14.08. The shape of the energy distribution from 0.44 μm to 100 μm suggests the existence of a temperature gradient in the circumstellar envelope. From the energy distribution of this star it is clear that star has warm and cold dust components. The CO and OH molecular emissions were not detected (Likkel et al 1991).

IRAS 17441—2411:

This IRAS source is AFGL 5385. We found its optical position by positional coincidence. Its visual magnitude V =13.35. The overall flux distribution from 0.44 μm to 100 μm indicates it has large far-IR excess and it has warm and cold dust shells. The IRAS colours places it in box IV of VH (1988) diagram. Detection of CO and

non-detection of OH molecular emission (Likkel et al 1991) indicates that the star may have a carbon-rich circumstellar envelope. According to the far-IR colours, this star falls in the region (Likkel et al 1991) of IRAS colour-colour diagram of very cold objects, where PPNe and evolved stars with CO detection are present. The observed B-V=1.7, and E(B-V)=0.9 yields the B-V=0.8 which corresponds to spectral type not later than G0. We conclude that IRAS 17441−2411 is a post-AGB star.

IRAS 23304+6147:

This object appears to be similar to IRAS 04296+3429. The presence of CO molecular emission and 21 μm emission (Woodsworth et al 1990; Kwok et al 1989) indicate that it has a carbon-rich circumstellar envelope. The CCD BVRI images of this star are stellar in appearance. The BVRI magnitudes obtained by us and those obtained by Hrivnak and Kwok (1991) are given in Table 2.2. The BVRI magnitudes obtained at three different epochs , suggest that IRAS 23304+6147 is gradually becoming fainter. But there is no significant variation in (B-V). The distance d =4 kpc inferred from molecular observations (Omont et al 1993) is comparable to the distance d =5 kpc derived in the present work.

2.6 Conclusions

We studied 14 IRAS sources with far-IR colours similar to PNe and post-AGB stars. We compared energy distributions of these sources with Kurucz atmospheric models and found that most of the sources have both hot and cold dust components. The sources IRAS 05238−0626, IRAS 08187−1905 and IRAS 17086−2403 have only cold dust components. From low resolution optical spectra and BVRI photometry we derived spectral types and luminosity classes for these sources. We estimated the stellar and dust envelope parameters of these stars. The dust envelope characteristics, low infrared flux variability, high galactic latitude, spectral type and supergiant luminosity class suggest that these 14 IRAS sources with far-IR (IRAS) colours similar to planetary nebulae are post-AGB stars. The dust envelopes around these stars are the result of severe mass-loss experienced by these during their AGB stage of evolution. None of these sources are associated with star forming regions. Several of these

sources have CO molecular envelopes with expansion velocities similar to those of evolved stars. Our sample also contains sources showing 3.3 μm and 21 μm emission features indicating that these are carbon-rich post-AGB stars.

Chapter 3

Chemical Composition Analysis

In this chapter we describe high resolution spectroscopic observational program and reduction procedures. We also discuss in brief the computational methods and analysis techniques involved in the study of chemical composition of post-AGB stars.

3.1 Observations

The high resolution spectroscopic data required for chemical composition analysis of post-AGB stars in this study, have been obtained with various telescopes. The spectrum of HD 179821 was obtained with the IDS+IPCS system fed by the 2.5 m Issac Newton Telescope (INT) located in La Palma. The spectra for IRAS 18095+2704 were also obtained with the INT. Spectroscopic observations for IRAS 05341+0852, IRAS 08187-1905 and HD 105262 were made with 2.1 m telescope (mcdat82) at McDonald Observatory. This telescope is equipped with a Cassegrain Echelle Spectrograph and a Reticon 1200×400 pixel CCD (McCarthy et al 1993). Each exposure yields an image frame containing 28 orders, having spectral range 1200Å to 1500Å with resolution 0.07 to 0.25 Å per pixel.

The medium resolution ($\Delta\lambda$=1.2Å) spectroscopic data for the high galactic latitude luminous star HD 105262 has been acquired using the 2.3 m telescope (Vainu Bappu observatory, Kavalur) at Cassegrain focus. The telescope is equipped with a Boller and Chiven (B&C) spectrograph and GEC p8603 CCD chip. The observation

log for the high resolution spectra and medium resolution spectra is given in Table 3.1.

3.2   Reductions

The CCD spectra were reduced using standard Image Reduction and Analysis Facility (IRAF) packages. Reduction of raw spectroscopic images consists of three steps: instrumental calibration which consists of bias and dark frame subtraction and flat field correction of object images, extraction of one-dimensional spectra, and wavelength calibration.

We averaged the bias frames taken on each night using the IRAF task *zerocombine* and the resultant bias frame for each night is subtracted from the spectra and flat field frames. This is done by the task *ccdproc* in CCDRED package. The bias subtracted flatfields are median combined with *flatcombine* task and normalized by *apnorm* in the SPECRED package of IRAF. The normalized flat field images divided into the spectrum frames to remove pixel-to-pixel variations across the CCD chip, again this is accomplished using *ccdproc*. We did not use dark frames, as the dark counts are negligibly small over the bias counts. Now the image is ready for extraction of the one-dimensional spectrum.

The extraction of the one-dimensional spectrum starts by defining the properties of each slit. These properties are the position of the object in the slit, the spatial size of the object and the curvature of the object position as a function of dispersion. In some cases, where background noise is high, (either due to long exposures or moon light), background subtraction from the adjacent pixels within the slit is required and these regions need to be defined. The signal within the defined aperture (normally 6-10 pixels) is then summed for each dispersion line and the background for that line is subtracted. This entire process may be done by the task *apall* in SPECRED (ECHELLE) package. The task *apall* also has the option to remove cosmic-ray hits on the spectrum. The net result of *apall* is the extracted one-dimensional spectrum with counts vs pixel number and is free of cosmic rays.

Table 3.1: High resolution and medium resolution spectroscopic observation log.

Objects	Wavelength range λλ	Grating lines/mm	Δλ	Date of obs.	Telescope
IRAS18095+27	4360 - 4650	1800	0.6	05 jul 93	La Palma INT
	4660 - 4950	"	0.6	04 jul 93	"
	4900 - 5205	"	0.6	"	"
	4600 - 4800	2400	0.35	19 Aug 92	"
	5327 - 5459	2400	0.35	24 may 91	
	6112 - 6226	"	"	"	"
	6285 - 6405	"	0.40	23 May 91	"
	6515 - 6630	"	0.40	"	"
	7060 - 7185	"	0.45	"	"
	7395- 7510	"	0.45	"	"
HD179821	4030 - 4520	1800	0.6	18 Nov 90	"
	4635 - 5120	"	0.6	"	"
	6230 - 6716	"	0.6	"	"
IRAS08187−1905	5025 - 5950	Echelle	0.16	10 Dec 95	Mcdonald mcd82
	5710 - 7230	"	0.16	"	"
IRAS05341+0852	6230 - 7230	"	0.16	11 Dec 95	"
HD56126	5710 - 7230	"	0.16	08 Dec 95	"
HD105262	5710 - 7230	"	0.16	"	"
	6380 - 8700	"	0.16	17 Jan 96	"
HD 105262	4200 - 4600	1800	1.1	13 Feb 95	VBO, VBT
	4900 - 5300	1800	1.2	14 Feb 95	"
	6000 - 6400	"	1.2	13 Feb 95	"
	6300 - 6700	"	1.2	14 Feb 95	"
	7100 - 7500	"	1.2	05 May 95	"

Wavelength calibration requires similar extracted spectra for each slit of comparison frame. The emission lines in the arc spectrum (Thorium or Thorium-argon) are identified using the atlas of Thorium-Argon spectra. The dispersion correction (wavelength solution) is determined from the arc spectrum by using Legendre polynomial of order 2 or 3 . This wavelength correction is determined by using the task *identify* in SPECRED or *ecidentify* in ECHELLE package. Finally each individual object spectrum is wavelength-corrected using the task *dispcorrection*. Now we have the spectrum with counts vs wavelength. The stellar spectrum is then smoothed by fitting a slowly varying function (such as cubic spline) to the continuum. This fit is divided into the spectrum to produce a flat spectrum where continuum is normalized to unity.

Before measuring equivalent widths, one must remove the telluric features in the stellar spectrum. Telluric features are removed by dividing the spectrum by that of a rapidly rotating hotter star, normally early A- or B-type stars, observed near the same air mass and reduced by the same methods. The rapid rotation of the hot stars guarantees that any weak lines present will be highly broadened and close to the continuum level. Telluric features are removed from the regions 6100Å, 6500Å, 7100Å, 7400Å, 7700Åand 8700Å.

Equivalent widths (W_λ) have been measured in two ways using *splot* package in IRAF. 1) by fitting a gaussian profile to the absorption line and 2) by measuring the total area of the line. If the absorption line is symmetric, full width at the half flux point is taken to fit a gaussian profile. But if the absorption line is not symmetric and has only right or left wing of the profile in gaussian form, then we have taken right half width or left half width at the half flux points, respectively, in constructing gaussian profile. These W_λ values usually agree to within 10% uncertainty. This small uncertainty may be due to the incorrect placement of continuum between each measurement and to the fact that the spectral lines are not perfectly gaussians. This uncertainty in W_λ may introduce an uncertainty in abundances to approximately Δlog (Abun) $\leq$0.1 dex. Slightly blended lines are deblended by the routines available in the *splot* package. We fit gaussians to individual absorption lines, and measured equivalent widths. For severely blended lines equivalent widths are not measured.

3.3 Analysis

3.3.1 Assumptions

The general assumptions made for stellar atmospheres in deriving chemical composi-
tion are as follows:

a) the atmosphere is in a steady state,

b) the flux of energy is constant with depth in the atmosphere since energy source for
the star lies far below the atmosphere and no energy comes into the atmosphere from
above. The flux is usually specified by an effective temperature such that flux=σT_{eff}^4,
σ=5.6697E-5,

c) the atmosphere is homogeneous and there are no spots ,no magnetic fields and no
granules etc,

c) the atmosphere is thin relative to the radius of the star, and hence it is plane
parallel,

d) there is no relative motion of the layers in the normal direction and no net ac-
celeration of the atmosphere; so the pressure balances the gravitational attraction
$\rho d^2 r/dt^2 = -\rho g + dP/dr = 0$

where ρ is the density and $g = GM^\star/R_\star^2$ is the gravitational acceleration, which is
assumed constant as the atmosphere is thin, with $M_\star$ and $R_\star$ as the mass and radius
of the star respectively.

This type of model atmosphere is called Local Thermodynamic Equilibrium (LTE)
atmosphere. These are the usual assumptions of essentially all abundance analyses
of stellar photospheres. The LTE analysis may be valid for the normal stellar at-
mosphere. In the context of analysis of low-mass supergiants with highly extended
atmospheres and dust shells around them, all of these assumptions are equally sus-
pect. There are known failures of LTE (Luck and Lambert 1985; Boyarchuk et al
1985). The oxygen abundance derived from O I 7770Å triplet (Gratton 1990) lines is
higher than that of abundance derived from [O I] 6300Å. This suggests that the non-
LTE effects in the excitation of the oxygen atom affect the formation of the permitted

7770Å triplet, but not the forbidden line.

The use of non-LTE models is constrained by lack of sufficient atomic data like collision strengths, size of the atom and uncertainties in the treatment of radiation field in model atmospheres. At present it is a difficult task to use non-LTE for analysis of every chemical element except for few selected elements. In this thesis, we used LTE model atmosphere in analyzing the chemical composition of photospheres of our selected post-AGB stars.

3.3.2 Atmospheric models

For effective temperature in the range 5000 K to 7500 K, we used atmospheric models of Gustafsson et al (1975), computed by MARCS code by R.E. Luck. For effective temperature higher than 7500 K , we used Kurucz (1979) atmospheric models computed using ATLAS6. Both these models are constructed based on the assumptions of the LTE atmosphere given in section 3.3.1

3.3.3 Codes used

In our study of chemical composition, we adopted both Fine Analysis and Spectrum Synthesis methods depending on the quality of available data. We used the updated computer codes, LINES for fine analysis and MOOG for spectrum synthesis analysis, which were originally developed by Sneden (1973). The detailed description of these codes and methods can be found in Sneden (1973) thesis and in a review article by Castelli and Hack (1990). We briefly describe here each of these methods.

3.3.3.1 Fine analysis

This method consists of comparing the measured equivalent width of a given unblended line with the equivalent width calculated for a given atmospheric model. A detailed computation of the equivalent width of each individual line as a function of abundance of the atom under consideration is carried out. For a given stellar model, abundance is modified until the computed equivalent width matches with that of

the observed equivalent width. This can be achieved by numerous iterations with some prefixed step value (we use 0.1 dex). Using fainter lines would be the best for the determination of abundances because their equivalent widths are not affected by microturbulence, by blending with the near by lines and by the damping constants. Moreover the weak lines are least affected by non-LTE. But to derive reliable elemental abundances, with the fine analysis method, one would require very high resolution spectra with good S/N ratio.

We used the computer code LINES (Sneden 1973) in our abundance analysis for fine analysis method. The code LINES basically solves the radiative transfer problem for spectral lines under the LTE assumptions and calculates line depths and equivalent widths for a given stellar atmospheric model. The LINES requires line data as an input. The line data, for each line consists of wavelength, excitation potential, first and second ionisation potentials and oscillator strength. All these atomic quantities are well-determined except oscillator strengths for lines of astrophysical interest. We have discussed about the gf-values in section (3.3.4).

3.3.3.2 Spectrum synthesis analysis

This method consists of comparing the observed spectrum with the computed spectrum. In this method fluxes are computed for very close λ values, with the resolution $\Delta\lambda=0.001$Å. This computed spectrum must be degraded to the resolution of the observed spectrum to allow a direct comparison. Broadening mechanisms, like instrumental broadening, rotational broadening and macro-turbulent broadening should be taken into account in the spectrum synthesis calculations. Instrumental broadening can be represented by a gaussian function, which has the same FWHM as the instrumental profile used to obtain the observed spectrum, and macrovelocity broadening can be simulated by gaussian function. The rotational broadening may be taken into account by computing the Doppler shifts of the intensities coming from different parts of the stellar disc and then integrating the Doppler-shifted intensities to obtain the flux. In spectrum synthesis calculations one requires extensive line lists for each element in the different ionisation states, with known laboratory wavelengths, excitation potentials for lower and upper levels and reliable transition probabilities (gf-values)

and broadening parameters. A huge database for both atomic and molecular lines is the pioneering work of Kurucz (1987, 1988).

Spectrum synthesis analysis has some advantages over fine analysis in chemical composition studies. The comparison of the computed spectrum with the observed one makes it possible to derive line identification, microturbulence, rotational velocities, Doppler shifts and abundances from single and blended lines. The continuum level in the observed spectra can be better estimated, particularly in the case of stars with high rotational velocities and stars with numerous metallic lines. Because the comparison of profiles gives much more information than the comparison of equivalent widths does, the computed spectrum is used to confirm abundances obtained with the fine analysis.

We have used spectrum synthesis code MOOG in our abundance analysis. MOOG inputs are: stellar atmosphere model, abundances of relevant elements, beginning and end points in the spectrum, step size in the spectrum, width of the spectrum to be considered at each point and line parameters which are similar to LINES. Given these as inputs to MOOG, it will calculate continuum flux, point by point, separated by a given step size. This calculated spectrum is degraded to the required observed spectrum resolution by supplying the resolution of the spectrum as PFUNC in MOOG code. MOOG must be run several times by adjusting the input abundances of elements until the computed spectrum matches that of observed one (see Sneden 1973 for detailed description of the MOOG code).

3.3.4   gf values

Oscillator strengths (gf values) are the most crucial physical data in abundance analysis. Laboratory measured values are proved to be highly reliable, but these are available for very few lines of astrophysically interest. In our study we made extensive use of Luck (1993, Private communication) compilation of gf values. For C I and N I we have taken the theoretical gf values calculated by Hibbert et al (1991,1993). The theoretical gfs of C I are in good agreement with the gfs determined from solar inverse spectrum (Biemont et al 1993). Theoretical gf-values have been chosen for

for main sequence stars, giants and supergiants (Flower 1977) are available. These empirical formulae for B-V vs T_{eff} are derived from observations of pop I stars. Consequently they are totally inadequate for use with metal-poor stars like pop II stars. For metal-poor stars, one has to rely on the theoretical T_{eff}:B-V:BC relations based on model atmospheres for different metallicities. Computed B-V colour indices for variety of model atmosphere of different metallicity are available (Kurucz 1979). Another widely used photometric system in deriving atmospheric parameters is Strömgren uvby system. The b-y colour is sensitive to temperature. Relyea and Kurucz (1978) have constructed grids of b-y colour and T_{eff} with metallicity range of pop I to Pop II. The use of photometric calibrations in determining T_{eff} in the case of post-AGB stars is hampered by reddening: either due to circumstellar, circumsystem, interstellar or some combination of those. The interstellar reddening contribution may be negligible for the high latitude post-AGB stars, but it is significantly important for the galactic post-AGB stars. Most of the post-AGB stars are IRAS sources, having circumstellar dust shells around them. Reddening properties of these dust shells are not known clearly. Using solely photometric systems to estimate T_{eff} for this kind of objects may lead to high temperature uncertainties and erroneous chemical composition. Another difficulty is that the computed grids do not go below gravity log g=1.0. Most of the known post-AGB stars are low gravity (Luck 1993) objects which go down to log g=0.3. To work in the region where these stars are located, the grids must be extrapolated. The primary calibration sources in the literature include: Bell and Gustafsson (1978) for T≤ 6000 K for all colours and Lester et al (1986) calibrations for T≥ 6000 K for (b-y) colours. All above mentioned methods (based on the availability of data) are used in estimating T_{eff}.

Spectroscopic T_{eff} determinations can be done in two ways: one is by excitation analysis of neutral atomic lines and the other is by matching Balmer profiles with the observed ones. In the case of excitation analysis, one plots the abundances determined from individual lines of neutral atomic lines of any species (eg Ti I,Cr I, Fe I) versus lower excitation potential. Correct T_{eff} is that T_{eff} for which abundances of neutral atomic lines are independent of their excitation potentials. This method assumes that there are no systematic excitation effects in the gf values. This is the most widely

used method in determining T_{eff} in the chemical composition analysis based on high resolution spectra. The T_{eff} determination by this method requires many neutral atomic lines with wide range of lower excitation potential. Applying this method in T_{eff} determination in post-AGB stars is constrained by the fact that the most of the post-AGB stars are metal-poor and there are very few neutral lines; hence insufficient range in low excitation potential of observed lines. This also assumes the lines are unblended and emission free. Another spectroscopic method to determine T_{eff} is that the comparison of synthetic and observed Balmer line profiles. Kurucz (1979) synthesized Balmer profiles for various models of pop I and pop II atmospheres. The cores of Balmer profiles are more sensitive to T_{eff} in A- and F-stars. Again here we restrict to only Hδ and Hγ, as there is a possibility of dust envelope effects in the Hβ and Hα profiles.

3.3.5.2   Surface gravity determination

Surface gravity can be determined from both photometry and spectroscopy. The synthetic colours of UBV and ubvy for different models of gravity and metallicity are computed by Relyea and Kurucz (1978). The c1-index Strömgren photometric system (c1=(u-v)-(v-b)) is very sensitive to changes in gravity for stars in the range 10,000 K $\geq T_{eff} \geq$ 5500 K (Relyea and Kurucz 1978). However, photometric determination of gravity is severely affected by circumstellar reddening.

Spectroscopically, gravity can be determined by using ionisation equilibrium of of different ionic states of any species (usually Fe I and Fe II). Here gravity is the free parameter to adjust until the abundance of Fe I is equal to the abundance of Fe II for given T_{eff}. Finding the gravity by ionisation balance has two difficulties. One is insufficient number of metallic lines in most of the post-AGB stars which are metal-poor. The second is that Fe II lines are too strong in the metal rich stars, and hence subject to microturbulence effects. The scatter in the Fe II abundance can be significant from which it follows that the Fe II line selection is critical in determining gravity. Another spectroscopic method to estimate surface gravity is by comparing the computed wings of Balmer profiles with the wings of observed profiles.

One can also use the mass and radius relation to determine log g. An equivalent form representing this relation is as follows:

$$\log g = \log g(M/M_\odot) - 10.62 - \log(L/L_\odot) + 4\log T_{eff}$$

The problem here is that stellar luminosity and mass are unknown. This can be applied to pop II post-AGB stars, by assuming typical pop II $M/M_\odot$=0.6 and typical post-AGB luminosity of $\approx 10^4$.

3.3.5.3 Microturbulent velocity

Another important physical parameter in abundance analysis is the microturbulent velocity (ξ_t). This can be determined by forcing the Fe II, Ti II and Fe I abundances to be independent of their equivalent widths. In this method ξ_t is the adjustable parameter for a given T_{eff} and log g model. The value of ξ_t may not be critical in the analysis of post-AGB metal-poor stars, if only weak lines are selected for final abundances. The use of weak lines also means that radiative damping terms will not be important. Normally in many of post-AGB stars there are not enough lines with a good range in equivalent widths. In this case one has to assume the ξ_t of another similar post-AGB star having almost similar physical parameters.

3.3.6 Selected post-AGB stars for Abundance Analysis: IRAS 05341+0852, HD 56126, HD 179821, HD 70379, IRAS 18095+2704 and HD 105262

IRAS 05341+0852

This is an optically visible star with IRAS colours suggesting it is post-AGB star. Geballe and van der Veen (1990) detected a strong 3.3 μm emission feature which is normally seen in the dust envelopes of evolved stars. This object is also one of the few post-AGB candidates which have been identified with unique 21 μm emission feature. In chapter 2, we studied its Spectral Energy Distribution (SED) from 0.44 μm to 100 μm and low resolution optical spectra and it has been suggested as a low-mass post-AGB F6 supergiant. In Chapter 4, we have for the first time studied the

chemical composition of this object based on high resolution spectra. The results of abundance analysis confirm the post-AGB nature of IRAS 05341+0852.

HD 56126

This star is the known post-AGB star satisfying the predicted chemical properties of post-AGB stars. This object also shows 21 μm emission feature (Geballe et al 1992). Bakker (1995) studied carbon molecular lines C2, CN and C3 in the AGB remnant of this object. Parthasarathy et al (1992) and Klochkova (1995) studied the elemental abundances of this object and found that this is a carbon-rich low-mass post-AGB star. This star has been discussed in Chapter 4 along with the IRAS 05341+0852.

HD 179821

This is a truly remarkable object. It has become the target of scrutiny ever since Odenwald (1986) found large far-IR excess due to dust envelopes. This object has been classified as a low-mass post-AGB star (Pottasch and Parthasarathy 1988; Hrivnak et al 1989; Likkel et al 1991; Justtanont et al 1992; van der Veen et al 1994) based on its SED, spectral class and molecular features. Zuckerman and Dyck (1986) suggested that this star was once a runaway O or B type star from its kinematics. In many ways this object also resembles the massive yellow supergiants with dust envelopes. Very recently, Kastner and Weintraub (1995) and Hawkins et al (1995) detected an extended nebula around this object and they suggested that HD 179821 is a massive yellow supergiant caught in between massive red giant branch and Wolf-Rayet phase of stars. Till date, the nature of this unusual object is not clear. In chapter 5 we discussed for the first time the chemical composition of this object. The results of our abundance analysis strongly support the suggestion that this object is a low-mass post-AGB star.

HD 70379

In chapter 2, we identified HD 70379 as a post-AGB candidate. Detailed chemical composition analysis of this star, based on high resolution spectra, is presented in chapter 4. The results of abundance analysis confirm the post-AGB nature of this star.

IRAS 18095+2704

This is a high latitude F3 supergiant of magnitude V=10.4. Hrivnak et al (1988) pointed out that this is an excellent candidate for proto-planetary nebula. Klochkova (1995) analyzed the high-resolution spectra of this object and found that it is an oxygen-rich evolved star. In Chapter 5 we analyze the elemental abundances based on the high resolution spectra obtained from ESO.

HD 105262

This is an interesting object with large proper motion ($0''.056$ yr^{-1}), lying at high galactic latitude ($+72°$). This was thought to be a HB star belonging to Wolf 630 group of stars (Eggen 1969) with M_v=0.4. However Eggen (1977) noted that the value of Strömgren C1 index (1.41) for HD 105262 is much larger than for any known HB star (C1=1.2 to 1.3). He also pointed out that this may be similar to the metal-poor luminous high latitude supergiant BD +39° 4926. Very recently Abt (1993) suggested that this may be another HR 4049 like star based on the narrow Balmer profiles which are similar to that of supergiants. For the first time we studied (Chapter 6) the chemical composition of this star based on medium ($\Delta\lambda$=1.2Å) and high ($\Delta\lambda$=0.2Å) resolution spectra. The kinematics and elemental abundances indicate that HD 105262 is most probably a low-mass post-AGB supergiant.

Chapter 4

Chemical composition of IRAS 05341+0852 a post-AGB star with 21 μm emission

4.1 Introduction

The AGB stars, post-AGB stars (or PPNe) and PNe which have dust envelopes around them are among the most numerous objects detected by IRAS. These are very luminous infrared objects corresponding to critical phases of low and intermediate-mass stars. Detailed studies of these objects in the wavelength region from ultraviolet to radio region are provide clues to understand the role of thermal pulses, nucleosynthesis, mixing and mass-loss and the transition from Oxygen-rich stars to Carbon-rich stars etc. The 11.3 μm emission of SiC is used to identify warmer carbon-rich circumstellar envelopes. It is absent in the circumstellar envelopes of coldest late AGB and post-AGB stars. With IRAS LRS spectra one can identify carbon-rich late AGB stars circumstellar envelopes. However, the situation is more complex for post-AGB objects with cold circumstellar envelopes. Several oxygen-rich post-AGB stars have LRS spectra hardly distinguishable from some carbon-rich post-AGB stars. HCN and OH observations and optical and near-IR spectroscopic observations are then

necessary to clarify the C/O character of some of the post-AGB stars.

The discovery of dust shells around some of the bright high latitude supergiants by Parthasarathy and Pottasch (1986) similar to PNe and their suggestion that these are post-AGB supergiants, led to a detailed study of these stars. Pottasch and Parthasarathy (1988) have shown that some of these stars have unusual LRS spectra. The CO/HCN line ratios of several of these post-AGB stars indicate that they have carbon-rich circumstellar envelopes (Omont et al 1993). On the other hand, the infrared spectra of some of these post-AGB stars show unidentified infrared features at 3.3, 6.2, 7.7, 8.6 and 11.3 μm, which are commonly attributed to the polycyclic aromatic hydrocarbon (PAH) molecules.

Recently, detection of strong broad emission feature at 21 μm and unusually strong 3.4-3.5 μm and 6-9 μm emission features in several PPNe and post-AGB stars were reported (Kwok et al 1995 and references therein). The optical spectroscopy has indicated that all the 21 μm emission sources are carbon-rich post-AGB stars (Hrivnak 1995). Detailed chemical composition study of one of the post-AGB stars with 21 μm feature (HD 56126) showed that it is overabundant in carbon and s-process elements indicating that it has gone through the third dredge-up on the AGB (Parthasarathy et al 1992; and Klochkova 1995).

Thus detailed chemical composition analysis of post-AGB stars with carbon-rich photospheres and carbon-rich circumstellar dust permits us to understand the correlation between C/O and abundances of s-process elements and the association of s-process enhancements with shell-flashes and dredge-up.

In our study of chemical composition of carbon-rich post-AGB stars we included IRAS 05341+0852 as it is found to have carbon-rich circumstellar dust (Geballe and van der Veen 1990). Parthasarathy (1993) found it to be a F-type supergiant with IRAS colours similar to planetary nebulae. Manchado et al (1989) made near-IR photometry of this star. IRAS 05341+0852 shows 3.3, 3.4-3.5, 7.7, and 11.3 μm PAH -related emission features (Geballe and van der Veen 1990; Kwok 1995) and also weak 21 μm feature (Kwok 1995). In this chapter we study in detail the chemical composition of IRAS 05341+0852.

Table 4.1: Basic parameters of IRAS 05341+0852 and HD 56126

		IRAS05341+0852	Ref.	HD56126	Ref.
Sp.type	a	F6I	a	F5I	c
T_{eff}		6500 K	a	6500 K	d
log g		1.0	a	0.5	d
α		$05^h13^m10^s$	b	$07^h13^m25.3^s$	e
δ		$08°52'23''$	b	$10°05'09''$	e
l''		$196°$		$206.75°$	
b''		$-12.0°$		$10°$	
V		11.89	a	8.23	f
(B-V)		0.61	a	0.9	f
E(B-V)		0.13	a	0.60	f

(a). Reddy & Parthasarathy (1996)., (b). IRAS catalogue

(c). Nassau et al (1965)., (d). Parthasarathy et al (1992)

(e). SAO catalogue., (f). Hrivnak et al (1989)

Reddy and Parthasarathy (1996) studied the flux distribution and low resolution optical spectrum and concluded that IRAS 05341+0852 is a post-AGB F6 supergiant type star. It is found to be very similar to the bright post-AGB F supergiant HD 56126 in T_{eff}, log g (Table 4.1) and [Fe/H] (Parthasarathy et al 1992). HD 56126 is also a carbon-rich post-AGB star with overabundance of s-process elements and it also shows 21 μm emission feature (Parthasarathy et al 1992). We carried out chemical composition analysis of HD 56126 in order to compare the similarities and differences in the chemical composition of IRAS 05341+0852 and HD 56126.

4.2 Description of the spectra

A few selected regions of the spectra of IRAS 05341+0852 are shown in Fig.4.1, along with those of HD 56126. It is clear from Fig.4.1 that the spectra of IRAS 05341+0852 is completely dominated by s-process elements Nd, Ce, La, Sm, Pr etc. The heavy

Table 4.2: Radial velocities of IRAS 05341+0852 and HD 56126

element	# of lines	IRAS05341+0852 $V_{helio} = 2.58$ km s^{-1} V_{obs} (km s^{-1})	σ	HD 56126 $V_{helio} = 16.28$ km s^{-1} V_{obs} (km s^{-1}	σ
C II	7	22.7	0.5	72.5	2.5
O I(7774Å)	3	24.1	0.7	-	-
O I(6157Å)	3	-	-	71.5	1.15
N I	1	23.0			
Sc II	3	22.9	0.5		
Fe II	5	22.9	1.1	74.5	1.5

element line identifications were done using the spectra of s-process rich star FG Sge (Kipper and Kipper 1993). We identified strong (EW=50mÅ) Li I doublet line at 6707Å in IRAS 05341+0852, which is absent in HD 56126. We also identified the S I and Al I lines in the spectrum (Fig. 4.1) of IRAS 05341+0852. Examining the spectral lines of heavy elements reveal that most of the lines are asymmetric. The sharp spectral features in IRAS 05341+0852 (Fig. 4.1), suggest that the star has highly extended atmosphere. The important feature observed in most of the post-AGB stars is Hα in emission. The Hα profile of IRAS 05341+0852 is compared with that of HD 56126 in Fig. 4.2. The Hα (Fig. 4.2) shows emission in the wings and a narrow absorption core similar to HD 56126. The structure of the Hα profile clearly indicates mass outflows. The list of identified lines and their equivalent widths (EWs) are given in Appendix.

4.3   Radial velocities

Measurement of radial velocity comes from 22 absorption lines showing no line asymmetry on our high resolution spectrum of IRAS 05341+0852. The telluric lines in the spectrum are used as references in measuring the radial velocity of these lines. We also derived radial velocities for HD 56126 from C II, O I and Fe II lines. The mean
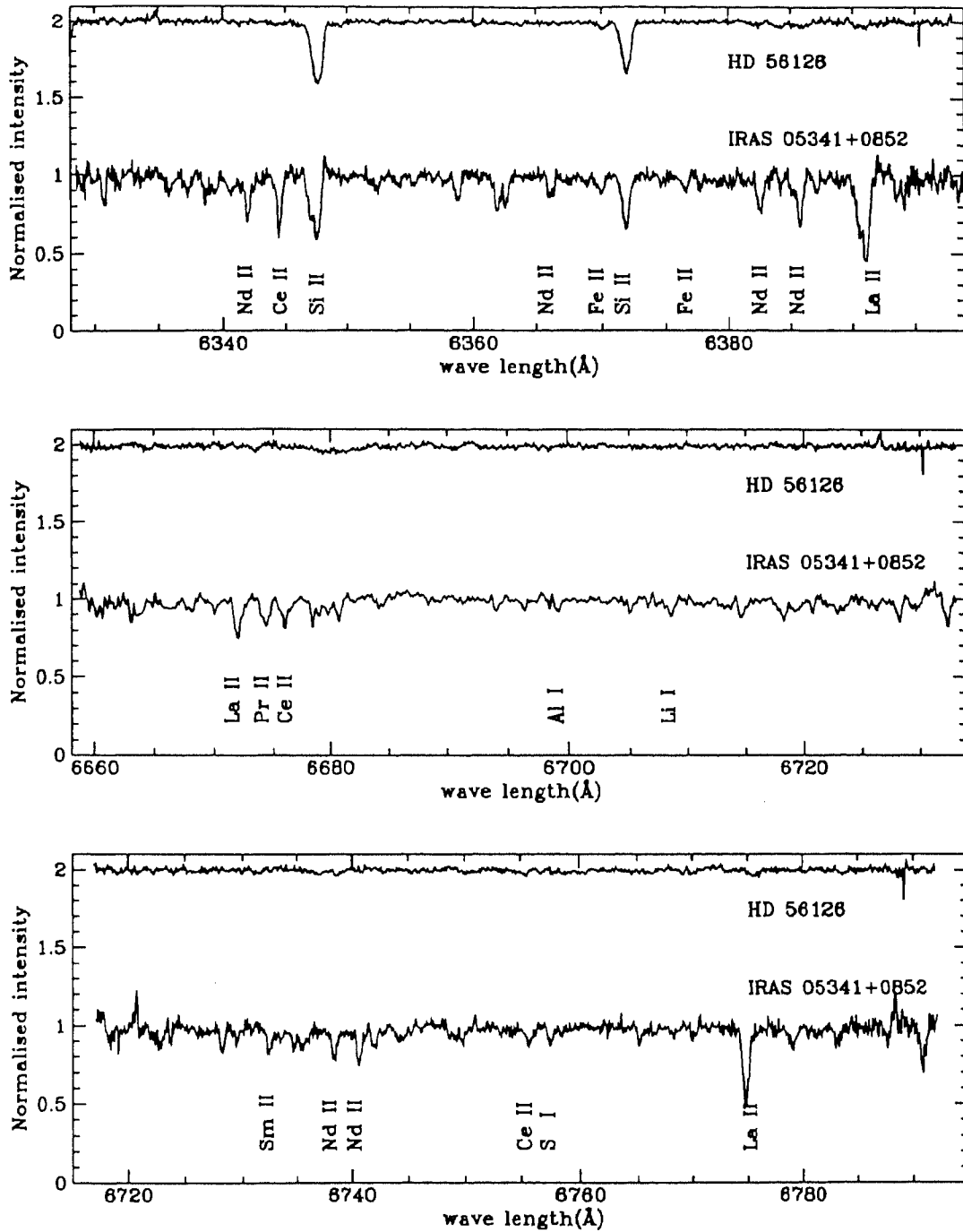
Figure 4.1: *Spectra of IRAS 05341+0852 is compared with a carbon-rich post-AGB star HD 56126. Important features of Li, Al, S and several s-process elements are marked. The spectra of IRAS 05341+0852 is dominated by s-process elements.*
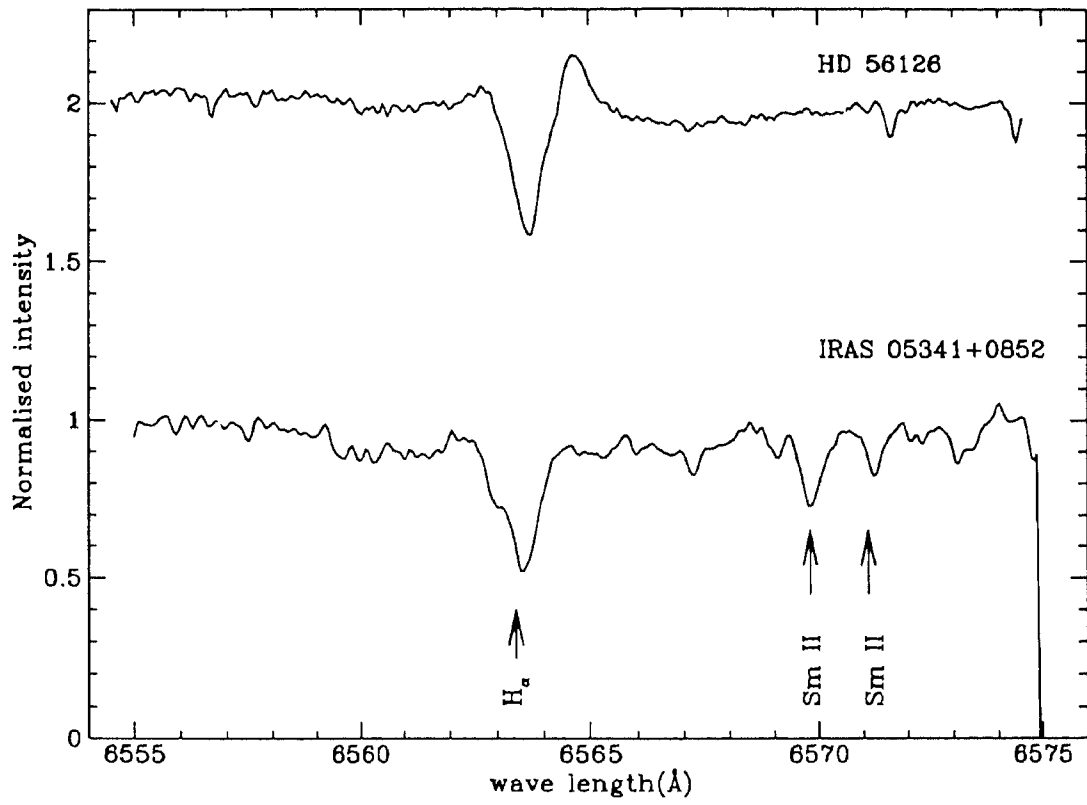
Figure 4.2: *Hα-profiles of IRAS 05341+0852 and HD 56126*

Table 4.3: Sulphur atomic data used in the sulphur abundance analysis

λ_{lab}	LEP(ev)	log gf
6748.573	7.868	-1.320
6748.682	7.868	-0.730
6748.779	7.870	-0.530
6748.839	7.868	-0.530
6756.851	7.870	-1.669
6757.007	7.870	-0.830
6757.171	7.870	-0.240
6757.195	7.870	-0.240

observed radial velocity of each element and the heliocentric correction velocities for the two stars are given in Table 4.2. After heliocentric correction, we obtain radial velocities, V_r=25 $\pm$1km s^{-1} and V_r=89$\pm$1 km s^{-1} for IRAS 05341+0852 and HD 56126 respectively. The derived velocity of IRAS 05341+0852 V_r=25 km s^{-1} suggests that the star may be an old disk population star. However, HD 56126 is a high velocity star, most probably a halo low-mass post-AGB star. The values of V_r for HD 56126 is in good agreement with the values V_r=90 km s^{-1} derived by Klochkova (1995). However Parthasarathy et al (1992) obtained a value which is 15 km s^{-1} more than that derived in this work. Bakker(1995) derived radial velocity V_r= 83 km s^{-1} from the C II, N I and O I lines.

4.4   Chemical composition analysis

The chemical composition analysis uses a set of model atmospheres and a combination of selected spectral lines and measurements of their equivalent widths and in some cases spectrum synthesis. In this section we discuss model atmospheres and atomic data needed in the abundance analysis. We also discuss the derivation of stellar model parameters T_{eff}, log g, microturbulence and metallicity. Finally we discuss the derived abundances and their sensitivity to uncertainties in the derived model

parameters.

4.4.1 Atmospheric models and atomic data

Elemental abundances have been derived with the local thermodynamic equilibrium (LTE) model atmosphere techniques. We used the updated code " LINES" originally developed by Sneden (1973) in deriving the elemental abundances, by fine-analysis technique. Crucial elemental abundances like Li, S and CNO have been determined from the spectrum synthesis analysis allowing for blends (see for details chapter 3)

The most important atomic data in the chemical composition analysis is the reliable transition probabilities (log gf) for observed lines. In Table 4.5 we list the spectral lines which are used in the chemical composition analysis. The table also contains low excitation potentials (LEPs), EWs , and log gf value for each line. We have taken the log gf values for most of the lines, from the recent compilation of R.E. Luck (1993,private communication). The adopted gf values in our carbon abundance analysis come from the work of Biemont et al (1993) who determined the gf values of C II lines from the solar abundance analysis. The gf values for N I lines are from Lambert et al (1982). The gf values for oxygen triplet at 7774Å are from solar abundance analysis of Lambert et al (1982). The set of sulphur lines used in the abundance analysis of spectrum synthesis are given in Table 4.3. The quoted gf values for S I lines are computed recently by Biemont et al (1993). The oscillator strengths for Fe I lines are all laboratory values which are taken from Bard et al (1991), Holweger et al (1991) and O' Brian et al (1991) or from the compilation of Fuhr et al (1988). The abundance analysis of Fe II lines is based on the accurate gf values determined experimentally by Biemont et al (1991) and Drake et al (1994). The measured gf values for Ni I at longer wavelengths are not available. We adopted the gf values determined by semi-empirical relations by Kurucz and Peytremann (1975).

The accurate gf values for the heavy elements are not available especially for the lines in the longward of 6250Å. The gf values used in our analysis come from either solar abundance analysis or theoretical estimates. For Y II abundance analysis, we used the solar oscillator strengths derived by Hannaford and Whaling (1982). The

Table 4.4: Atmospheric parameters used in the chemical composition analysis of IRAS 05341+0852 and HD 56126

Star	T_{eff}	log g	ξ_t	[M/H]
IRAS 05341+0852	6500 K	0.5	5 km s^{-1}	−1.0
HD 56126	7000 K	0.1	5.5 km s^{-1}	−1.0

La II abundances are based on the reliable gf values determined recently by Bord et al (1996). The gf values for Nd II lines in our spectral range are not available. Out of 30 identified Nd II lines we got gf value for only one line at 6365.550Å (Ward 1985). The available gf values for Sm II, Ce II and Pr II are listed in Table 4.8 which are taken from Kurucz and Peytremann (1975).

4.4.2 Atmospheric parameters

The atmospheric model parameters: effective temperature (T_{eff}), surface gravity (log g) and microturbulent velocity (ξ_t) for the chemical composition analysis of IRAS05341+0852 were determined as follows.

Reddy and Parthasarathy (1996) have estimated T_{eff}=6500K and log g=1.0 by comparing the flux distribution of this source with Kurucz atmospheric models by applying the interstellar reddening E(B-V)=0.23. The B-V vs T_{eff} calibrations of Flower (1977) yields T_{eff}=6200K. The spectral type F6I (Reddy and Parthasarathy 1996) of this source corresponds to T_{eff}=6200K. We used these parameters as initial values in deriving the accurate atmospheric parameters by spectroscopic method.

A spectroscopic estimate of T_{eff} is found by identifying the model atmospheres for which the iron abundance given by Fe I lines is independent of their low excitation potential. We tried with three models of different T_{eff} for a given log g and ξ_t . The log g has been determined by forcing the Fe I and Fe II lines to yield the same iron abundance for the given T_{eff} and ξ_t . The ξ_t has been determined from individual Fe I lines to show no dependence on their equivalent widths
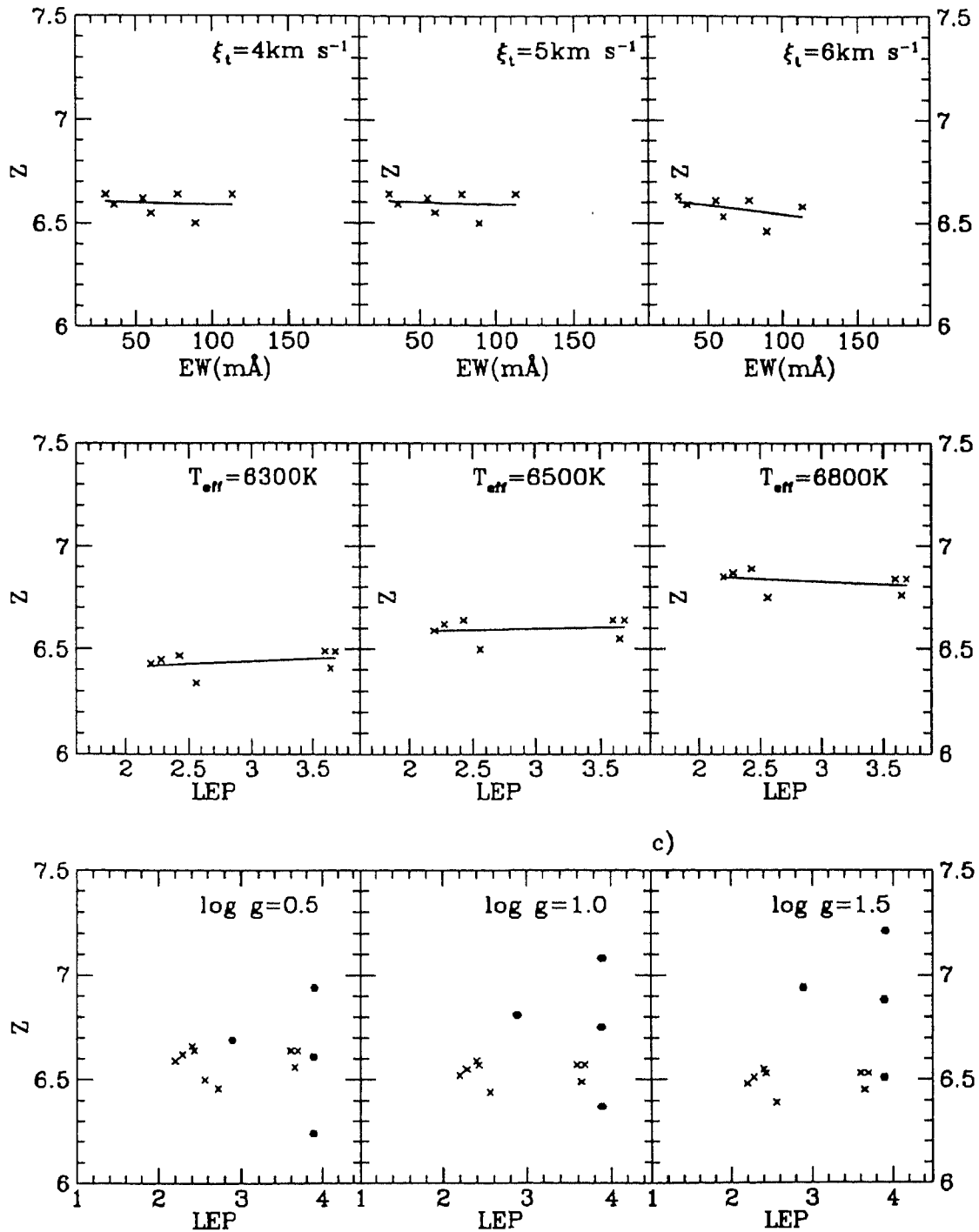
Figure 4.3: *Spectroscopic determination of atmospheric parameters: Top panel: log*
ε (Fe I) vs Ews of Fe I lines, Middle panel: log ε (Fe I) vs LEP, Bottom panel: log ε
(Fe II)(filled circles) and log ε (Fe I)(croses) vs LEP.
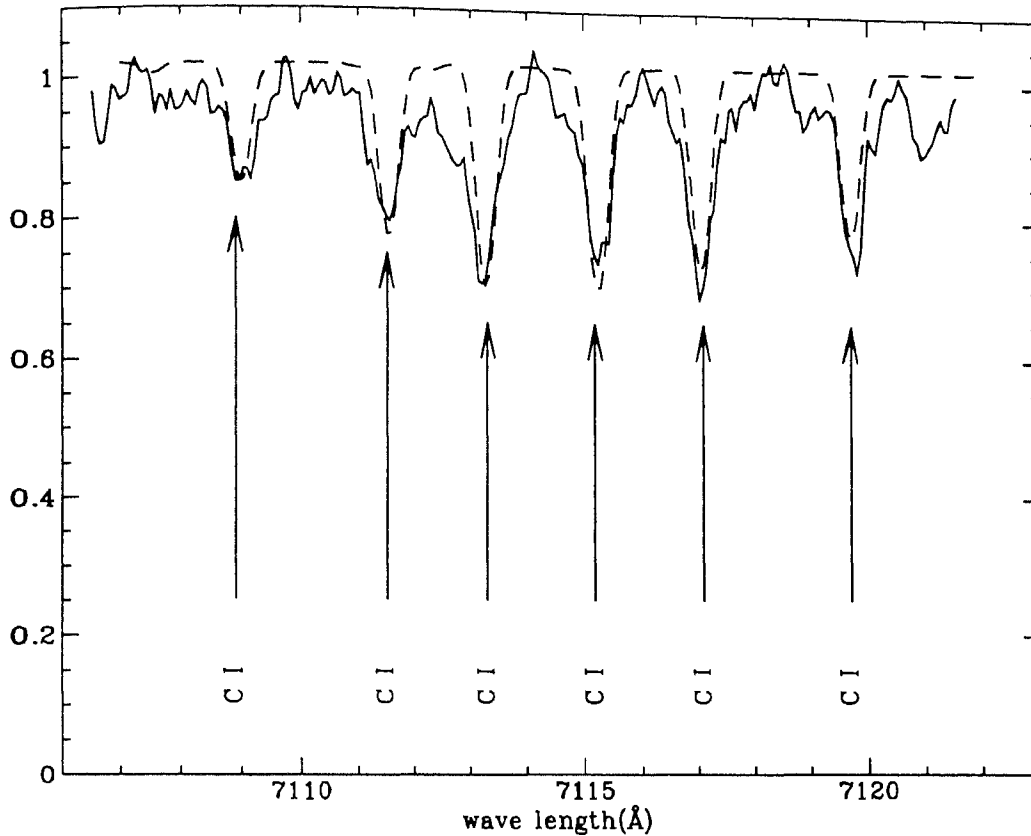
In Fig. 4.3 we illustrate the spectroscopic determination of stellar parameters ηg Fe I and Fe II lines. In the top panel log ϵ(Fe I) versus EWs of Fe I lines are tted. No trend is apparent for a ξ_t=5km s^{-1}. In the middle we plotted logϵ(Fe I) sus low excitation potential of Fe lines and for T_{eff}=6500 K the slope of the fit Imost zero. In the bottom panel we plotted abundances of Fe I and Fe II versus itation potentials for three different surface gravities for a given T_{eff} and ξ_t. The ındances of Fe I and Fe II are in good agreement for the log g=0.5 model.

4.4.3 Abundances

From above analysis we found model atmosphere: T_{eff}=6500 K, log g=0.5 dex , ξ_t=5 km s^{-1} and metallicity [M/H]=$-$1.0 is the most appropriate for the atmosphere of IRAS 05341+0852. Abundances derived using the above model are given in Table 4.6. Summary of elemental abundances of IRAS 05341+0852 and HD 561326 are given in Table 4.6 and Table 4.7 respectively. In this section we briefly discuss the abundance analysis of each species.

The abundance of Li has been determined by spectrum synthesis analysis of Li I resonance doublet feature at 6707.761Å and 6707.912Å. The basic line data required for the synthetic spectrum has been taken from Lambert et al (1993). In addition to the four Li-lines at 6707Å a number of other lines had to be considered. In fitting the synthetic spectra to observed spectra of Li-feature, we included the Ce II line at 6707.740Å as suggested by Lambert et al (1993). We tried to reproduce the observed Li-feature by including the Sm II and Ce II lines and their abundances were determined from other Sm II and Ce II lines in the spectrum. Since the optical spectra of this source is dominated by s-process elements, it is likely that the Li-feature is contaminated by these lines. From the spectrum synthesis analysis of Li-feature, we derive an upper limit to the Li-abundance of IRAS 05341+0852: log ϵ(Li)=2.5. The upper limit to the Li abundance is based on the following facts: there might be still unidentified lines which are contributing to the observed strength of the Li-feature (Lambert et al 1993) and there may be uncertainties in derived abundances of Sm II and Ce II. We derived the carbon abundance both from spectrum synthesis and line analysis. In fig. 4.4 we show the carbon region λ 7100-7125Å which contains five C II lines. The internal scatter among the individual carbon lines is very small. Other carbon lines are detected at 6587Å, 7070Å and 7476Å. These individual lines yield abundances which are in agreement with abundances derived from 7100Å lines. The final C II abundance listed in Table 4.6 is the average of all the individual carbon lines. For N I we have three features at 7423.63Å, 7442.23Å and 7468.27Å. The line at 7442.23Å is not used in our analysis, since it falls at the end of the chip and unfortunately it is hit by cosmic rays. The line at 7423.63Å is blended with the Si I and abundance derived from this line might have been overestimated. We were left

with one clean N I line at 7468.27Å which yields abundance 0.4 dex less than that of N I line at 7423.63Å. Luck and Lambert (1985) showed that the Non-LTE effects on abundances derived from N I lines are upto 0.6 dex for stronger N I lines. Since the identified N I lines in our source are weaker (EW≤70mÅ), the deviation of the abundances due to Non-LTE effects may be small.

We derive oxygen abundance by spectrum synthesis of O I triplet at 7774Å. The lines are very strong and these are known to be plagued by known Non-LTE effects (Johnson et al 1974). The derived average abundance from the three lines log ϵ(O I)=9.2 dex. Takeda (1994) analyzed the Non-LTE effects on the oxygen abundance in the metal-poor dwarfs for different T_{eff}, metallicities and gravities. Non-LTE abundance corrections for O I at λ 7774Å (Takeda 1994) indicate that a large Non-LTE corrections may be needed for IRAS 05341+0852 as the star has a highly extended atmosphere. Bascheck et al (1977) studied the Non-LTE effects on oxygen triplet lines at 7774Å and tabulated the equivalent widths derived from Non-LTE models and from LTE model analysis for A-type stars. From this study we approximately derived the abundance difference of Δ log ϵ (O I) $\leq$ 0.8 between LTE and Non-LTE analysis for IRAS 05341+0852. This analysis yields oxygen abundance [O/H]=+0.5. We can also have rough estimate about oxygen abundance by assuming that the oxygen overabundance follows the trend observed among the field stars increasing with decreasing metallicity as [O/Fe]≈-0.5[Fe/H] until [Fe/H]≈−1.0 (Wheeler et al 1989). This yields an oxygen abundance [O/H]=0.5 for a star of metallicity [Fe/H]=−1.0. In the case of HD 56126, oxygen abundance ([O/H]=−0.21) comes from the O I triplet at 6156Å which is in good agreement with the value ([O/H]=−0.37) of Klochkova (1995)

The abundance of sulphur has been derived from spectrum synthesis of two S I lines at 6757Å and 6748Å. The derived sulphur abundance [Fe/S]= 0.07 which is consistent with the stellar model calculation of AGB stars. Abundance of Aluminum [Al/Fe]=1.07 is based on the two weak Al I lines at 6696.032 (31mÅ) and 6698.669 (28mÅ). We derived the abundance of Si ([Si/Fe]=1.15) from two strong Si II lines at 6347.532Å and 6371.767Å. Our abundance analysis of Fe I and Fe II is based on very limited number of lines. In our iron analysis we used only lines of EW≤150mÅ and

Table 4.5: Lines used in the abundance analysis using the LTE model atmosphere: T_{eff}=6500 K , log g=0.5 , ξ_t=5km s^{-1} and [M/H]=-1.0.

λ_{lab}	ident.	LEP(ev)	EW(mÅ)	log gf	Abun.
6707.980	3.0	.00	35.00	-0.510	3.43
6587.622	6.00	8.53	160.00	-1.049	8.71
7111.480	6.00	8.64	132.40	-1.07	8.64
7113.180	6.00	8.64	176.00	-0.760	8.69
7115.190	6.00	8.64	161.00	-0.899	8.69
7116.990	6.00	8.64	181.00	-1.08	9.05
7119.660	.00	8.64	130.00	-1.31	8.85
7423.630	7.00	10.33	68.00	-0.610	8.50
7468.270	7.00	10.33	60.00	-0.210	8.01
7771.954	8.00	9.14	440.00	0.364	10.29
7774.177	8.00	9.14	509.00	0.217	10.88
7775.395	8.00	9.14	352.00	-0.0400	9.93
6696.032	13.00	3.14	31.00	-1.32	6.44
6698.669	13.00	3.14	28.00	-1.62	6.69
6347.090	14.10	8.12	282.00	0.260	7.87
6371.350	14.10	8.12	227.30	-0.0500	7.63
6439.083	20.00	2.52	110.00	0.390	5.25
7148.150	20.00	2.71	90.00	0.137	5.53
6245.620	21.10	1.51	100.00	-0.930	2.13
6279.740	21.10	1.50	109.00	-1.16	2.41
6604.600	21.10	1.36	135.00	-1.48	2.78
6230.735	26.00	2.56	89.00	-1.281	6.50
6335.337	26.00	2.20	35.70	-1.23	6.59
6336.830	26.00	3.69	30.00	-1.05	6.64
6393.612	26.00	2.43	77.40	-1.62	6.64
6400.010	26.00	3.60	113.00	-0.290	6.64

Table 4.5 continued

λ_{lab}	ident.	LEP(ev)	EW(mÅ)	log gf	Abun.
6411.658	26.00	3.65	60.0	-.620	6.56
6421.360	26.00	2.28	55.0	-1.947	6.62
6494.994	26.00	2.40	126.0	-1.273	6.66
6592.926	26.00	2.72	38.0	-1.599	6.46
6677.999	26.00	2.69	75.0	-1.47	6.71
7411.162	26.00	4.28	52.0	-0.33	6.7
7445.758	26.00	4.26	69.0	-0.02	6.6
7495.077	26.00	4.18	102.0	0.18	6.7
6247.562	26.10	3.89	116.0	-2.51	6.24
6369.463	26.10	2.89	55.00	-4.36	6.69
6383.715	26.10	5.55	43.00	-2.27	6.79
6416.928	26.10	3.89	119.00	-2.85	6.61
6516.083	26.10	2.89	146.00	-3.45	6.53
6643.638	28.00	1.68	12.00	-2.299	5.31
7122.695	28.00	3.54	40.00	0.039	5.20
7525.118	28.00	3.63	26.00	-0.339	5.45
6643.638	28.00	3.85	53.00	0.210	5.46
6795.410	39.10	1.73	111.00	-1.55	2.86
6832.490	39.10	1.74	84.00	-1.82	2.93
6858.240	39.10	1.74	76.00	-2.25	3.28
7264.200	39.10	1.84	161.00	-1.50	3.30
6496.908	56.10	.60	571.00	-0.379	3.76
6399.040	57.10	2.63	115.00	-0.648	3.07
6642.790	57.10	2.51	66.00	-1.08	2.98
6834.050	57.10	.24	104.00	-3.192	3.35
6675.540	58.10	1.53	84.00	8 -1.40	3.60

Table 4.5 continued

λ_{lab}	ident.	LEP(ev)	EW(mÅ)	log gf	Abun.
6755.080	58.10	1.67	75.00	-1.64	3.90
6397.960	59.10	1.04	81.00	-0.819	2.03
6365.550	60.10	.93	46.00	-1.41	2.36
7051.520	62.10	.92	76.00	-1.560	0.40
6256.660	62.10	1.16	62.00	-1.63	0.58
6431.820	62.10	1.40	84.00	-2.04	1.40
6502.000	62.10	1.55	63.00	-1.97	1.27
6570.675	62.10	.99	60.00	-1.91	0.68
6731.890	62.10	1.16	66.00	-1.22	0.20
6741.470	62.10	.99	75.00	-1.72	0.62
7039.225	62.10	.99	101.00	-1.45	0.56

hence the errors due to may be Non-LTE are minimal. The abundances of other iron peak elements Ca, Sc and Ni are also derived from lines which have EW$\leq$ 100mÅ. These abundances (Ca,Sc,Ni/Fe$\approx$0.0) are in good agreement with the iron abundance.

The derived abundance of light s-process element Y is found to be large with respect to Fe ([Y/Fe]=1.85). We could not derive abundances from other light s-process elements Sr and Zr in our observed range of spectrum. However, the abundance of Y is represented by 4 relatively clean Y II lines. The large overabundance of Y suggest that the star is overabundant in light s-process elements. Abundance of Ba ([Ba/Fe]=2.56) is based on very strong (EW=560mÅ) Ba II line at 6496Å. Since it is derived from very strong and single line, the abundance of Ba may be uncertain. Nonetheless, the abundances of other major heavy s-process elements La ([La/Fe]=2.86) (3 lines) and Ce ([Ce/Fe]=2.96)(2 lines) clearly demonstrates that IRAS 05341+0852 is infact rich in s-process elements. The other heavy elements like Pr, Nd and Sm also show large overabundances. The spectra of IRAS 0534 is well dominated by strong Nd II lines. However we were able to deduce the Nd abundance ([Nd/Fe]=1.97) from a single Nd II line at 6365Å due to scarcity of atomic data for other lines. The

Table 4.6: Chemical composition of IRAS 05341+0852 derived from LTE atmospheric model: T_{eff}=6500 K, log g=0.5, ξ_t=5km s_{-1} and [M/H]=−1.0.

Element	# of lines	Abun.	σ	$A_{\odot}$	[X/H]	[X/Fe]
Li I	1	2.5(synth)	-	1.00	1.5	2.45
C II	6	8.77	0.15	8.69	0.08	1.03
N I	2	8.26	0.35	7.99	0.26	1.21
O I	3	9.23(synth)	0.25	8.91	0.32	1.27
		8.43	-		0.47	0.5
AlI	2	6.56	0.17	6.47	0.09	1.04
Si II	2	7.75	0.16	7.55	0.20	1.15
S I	2	6.31(synth)	-	7.21	-0.90	0.07
caI	2	5.39	0.19	6.36	-0.97	-0.01
Sc II	2	2.27	0.19	3.10	-0.83	0.12
Fe I	10	6.60	0.07	7.54	-0.94	0.01
Fe II	5	6.57	0.20	7.54	-0.97	-0.01
NiI	4	5.355	0.12	6.25	-0.89	0.06
Y II	4	3.09	0.22	2.24	0.85	1.80
Ba II	1	3.76	-	2.13	1.63	2.58
La II	3	3.13	0.19	1.22	1.91	2.86
Ce II	2	3.55	0.21	1.55	2.00	2.95
Pr II	1	2.03	-	0.71	1.32	2.27
Nd II	1	2.36	-	1.34	1.02	1.97
Sm II	8	0.71	0.41	0.80	-0.09	0.86

Note:-   After Non-LTE correction of 0.8 dex

Table 4.7: Summary of elemental abundances of HD 56126 from LTE atmospheric model: T_{eff}=7000 K, log g=0.25, ξ_t=5.5km s$_{-1}$ and [M/H]=$-$1.0.

Element	[X/H]^a	[X/Fe]^a	[X/H]^b	[X/Fe]^b	[X/H]^c	[X/Fe]^c
C	0.08	1.08	$-$0.01	1.34	$-$0.06	0.9
N	0.03	1.03	0.17	1.53	$-$	$-$
O	$-$0.37	0.63	$-$0.02	1.33	$-$0.21	0.75
Al	0.47	1.47	$-$	$-$	$-$	$-$
Si	0.0	1.0	$-$0.85	0.5	$-$	$-$
S	$-$0.37	0.63	0.01	1.46	$-$	$-$
ca	$-$0.55	0.45	$-$2.24	0.89	$-$1.25	$-$0.30
Fe	$-$1.0	0.0	$-$1.35	0.0	$-$0.96	0.0
Y II	0.7	1.7	$-$	$-$	$-$0.18	0.78
Ba	$-$0.1	0.99	0.4	1.35	0.4	1.35

Note:-

(a.) Klochkova (1995)., (b.) Parthasarathy et al (1992)., (c.) This work

abundance of Sm([Sm/Fe=0.86) is derived from 8 Sm II lines and the abundance of Pr([Pr/Fe]=2.27) is based on Pr II line at 6398Å.

4.4.4 Uncertainties in the derived abundances

In this section we deal with the possible sources of uncertainties in the derived elemental abundances. The uncertainty in the derived Li- abundance is mainly attributed to the fitting of the synthetic spectra to the observed spectra in the Li region. Since our spectral resolution R=45,000 is insufficient to resolve the lines involved in the spectrum synthesis of Li-region (Lambert et al 1993), the uncertainties in the derived Li-abundance are subject to the uncertainties involved in the abundances of elements that have participated in the spectrum synthesis of Li-region. Lambert et

Table 4.8: Sensitivity of elemental abundances to changes in the adopted atmospheric parameters: T_{eff}= 6500K, Log g=0.5 and ξ_t=5km s^{-1}

species	ΔT_{eff}=250K	Δlog g=0.25	$\Delta \xi_t$
Li I	0.25	0.1	0.02
C II	0.03	0.02	0.14
Al I	0.2	0.04	0.01
Si II	0.05	0.06	0.25
S I			
Ca I	0.2	0.04	0.1
Sc II	0.3	0.2	0.1
Fe I	0.3	0.04	0.05
Fe II	0.1	0.1	0.1
Y II	0.2	0.1	0.05
Ba II	0.4	0.01	0.3
La II	0.2	0.1	0.1
Ce II	0.2	0.1	0.1
Pr II	0.2	0.1	0.0
Sm II	0.2	0.05	0.0

al (1993) also suggested that there may be still few unidentified species in the Li-region and the derived Li- in lithium rich stars may be an upper limit. We performed Li-abundance analysis for different atmospheric models. From Table 4.8, it is clear that the Li-abundance is less sensitive to the selected T_{eff} of the model, and quite insensitive to the surface gravity and micro turbulence.

The line-to-line scatter in the C abundance (Table 4.6) is represented by standard deviation (σ) 0.15 dex. The scatter in the C II abundances is mainly due to the placement of the continuum and the uncertainties in the log gf-values. In the case of N and O analysis, quantifying the line-to-line scatter in the abundances is difficult as these are derived from very few lines. Moreover the O abundance analysis is based on

the oxygen triplet at 7774Å which are largely affected by Non-LTE effects. In order to see what impact the uncertainties in the atmospheric parameters had on the CNO abundances, we repeated the CNO analysis varying ξ_t by $\pm$ 1 km s^{-1}, T_{eff} by $\pm$ 250 K and log g by $\pm$ 0.25 dex. The effects of uncertainties in the derived atmospheric parameters on the derived abundances are tabulated in Table 4.8. The combined effect of these variations produced maximum uncertainty in the CNO abundances of 0.1 , 0.2 and 0.4 dex respectively. In the carbon analysis the uncertainty is largely due to uncertainty in ξ_t and T_{eff}.

The uncertainties in the heavy-element abundances are a bit more difficult to quantify because errors in the atomic data (mainly log gf values) may vary from line-to-line. For those elements for which three or more lines were analyzed, standard errors for the abundances derived from the individual lines are given in Table 4.8. The internal scatter in the case of Y, La and Ce is around 0.2 dex and in the case of Sm it is 0.4 dex. The large scatter in the individual line abundances may be largely due to the unreliable log gf values for most of the heavier elements. Also we have repeated the analysis for the heavy elements by varying the atmospheric parameters as described above. For all elements except Ba II the abundances changed by < 0.3 dex due to changes in the atmospheric parameters. The Ba II abundance is derived from a strong line and stronger lines are particularly sensitive to variations in the microturbulence. In the case of Ba change in the ξ_t by 1 km s^{-1} produces a change of 0.4 dex in Ba abundance. We conclude that the maximum uncertainties due to the uncertainties in the atmospheric parameters in Y, La, Ce, Pr < 0.4 dex and in Ba < 0.6 dex.

4.5 Absolute magnitude

Absolute visual magnitudes for the stars can be estimated from their model atmospheric parameters and core mass through the simple relation,

$$M_v = -2.5log(M/M_\odot) + 2.5logg - 10logT_{eff} - B.C + 31.3$$

The metallicity [Fe/H]=−1.0, its radial velocity V_r=24 km s^{-1} and its high lati-

tude suggest that IRAS 05341+0852 is most probably a low-mass star belonging to old disk Pop-II stars. The observed chemical composition of this star (carbon-rich) also shows that star may be low-mass post-AGB star with core mass of around 0.6 $M_\odot$ to 0.8 $M_\odot$. This corresponds to the original mass range of 1 to 2 $M_\odot$ and the mass-loss on the two ascents of red giant branch probably reduced the mass. Using the stellar parameters derived above and assuming the stellar mass of around 0.7 $M_\odot$ and ignoring the bolometric correction, we find a very high luminosity $M_v = -5.3$. The uncertainties in the derived atmospheric parameters and assumed stellar mass contribute uncertainty in the derived M_v by about ± 1 mag. The high luminosity of this star is consistent with the post-AGB evolutionary tracks (Blöcker 1995). It is also known that the O I features at 7774Å are correlated with the stellar luminosity for a large range of spectral types (Sorvari 1973; Mendoza 1989). We derived $M_v = -5.0$ from the M_v vs W(O I) relation for high latitude A-type luminous stars (Ferro and Mendoza 1993). This value is comparable to the M_v derived from the above relation.

Using the absolute magnitude $M_v = -5.0$, $m_v = 11.89$ and the extinction $A_v = 0.7$ (extinction both due to dust around the star and interstellar medium) the distance modulus method yields a distance r=10 kpc. The distance of the star above the galactic plane (z) is found to be 2.0 kpc using the formula z=r sin b where b=$-12°$.

4.6 Discussion

The overabundances of s-process elements and carbon in IRAS 05341+0852 is the direct evidence for the association of s-process enhancements with shell-flashes and dredge-up. These are clearly responsible for the increase in C/O. The most likely neutron source, for the large overabundance of heavy elements, may be ^{13}C. The small amounts of hydrogen get mixed with ^{12}C rich material which is just below the hydrogen burning shell due to semiconvection during He-shell flashes (Hollowell 1987; Hollowell and Iben 1988). This hydrogen reacts with ^{12}C resulting in ^{13}C. When ^{13}C enriched matter is mixed down due to He-shell flash, it burns via reaction $^{13}C(\alpha, n)^{16}O$ which generates neutrons for s-process elemental production. This reaction is

quite efficient, requiring temperatures $\leq 1.5 \times 10^8$ K, which are easily found in the inter-shell convective zone of models of low-mass stars. Models indicate that this is more efficient in metal-poor AGB stars and/or post-AGB stars with small envelope mass (Iben and Renzini 1984; Lattanzio 1989). The s-process enrichment in the atmosphere of IRAS 05341+0852 has taken place during the shell flash events on the AGB. The neutron exposures follow an exponential distribution. Using the Tables of Malaney (1987) a mean neutron exposure $(\tau_o) = 0.3$ is suggested. A similar value was found by Gonzalez and Wallerstein (1992) for the post-AGB star ROA 24 in Omega Centauri.

The overabundance of Li and Al in IRAS 05341+0852 indicates that there was Hot Bottom Burning (HBB), where the base of the convective envelope is hot enough for nucleosynthesis to occur (Scalo et al 1975). HBB has been suggested as the mechanism responsible for the production of Li in the Li-rich AGB stars discovered by Smith and Lambert (1989, 1990). Infact these are bright AGB stars which are oxygen-rich rather than carbon-rich. Recent calculations by Sackmann and Boothroyd (1992) showed that Li-rich AGB stars are the result of HBB. In the HBB models, temperatures of the order of 0.5 - 1 $\times$ 10^8 K are encountered at the base of the convective envelope (Blöcker and Schönberner 1991; Lattanzio 1992). This is hot enough for the reaction $^{25}Mg(p,\gamma)$ ^{26}Al resulting in the production of Al. More recent model calculations of HBB in AGB stars by Lattanzio et al (1996) and Mowlavi (1995) show that significant amount of Li and Al are convected to the surface as a result of third dredge-up.

However in the words of Lattanzio " the Hot Bottom Burning must be seen as an unfortunate occurrence. It is already difficult using interior models, linked by dredge-up, to predict the composition of AGB star photospheres. To this we must add the possibility of nuclear processing of the envelope, which consists of the initial envelope, and the products of earlier nuclear burning in the interior. A very complicated problem in nucleosynthesis and mixing. "

The possibility of Li synthesis in the AGB stars was first recognized by Cameron (1955) and Cameron and Fowler (1971) who proposed ^7Be transport mechanism in which ^7Li is created via the sequence of following reactions: a) $^3He(\alpha,\gamma)^7Be$, b)
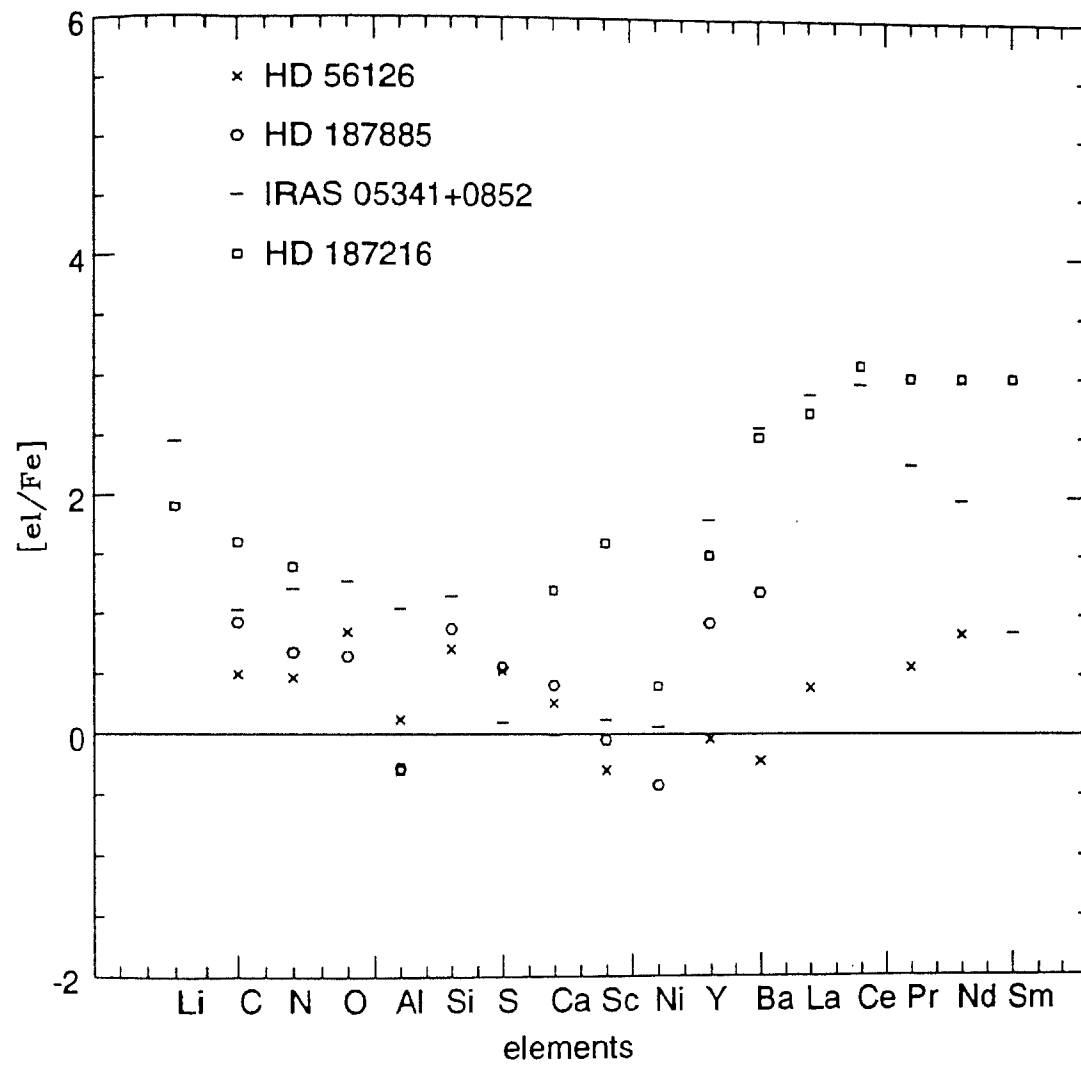
Figure 4.5: *The average elemental abundances of IRAS 05341+0852 is compared with the known carbon-rich post-AGB stars, HD 56126 and HD 187885 and a carbon star HD 187216.*

$^7Be(p,\gamma)^8B$, c) $^7Li(p,\alpha)^4He$, d) $^7Be(e^-,\nu)^7Li$. The first reaction is capable of converting much of the available ^3He to ^7Be in the deep interior if the $T\approx40\text{-}50\times10^6K$.The second and third reactions are destructively effective at $T\approx20\times10^6$ and 3×10^6K respectively. The fourth one will produce and preserve the Li if $T\leq3\times10^6K$. This process can be successful only if the ^7Be produced by the first reaction is transported to regions where $T<3\times10^6K$ in a time smaller than the mean life time of ^7Be to protons. Indeed presence of large Li abundance in evolved stars and theoretical studies suggest that under certain conditions, ^7Li may be created and mixed to the surface of luminous AGB stars (Scalo et al 1975). However the models show (Sackmann and Boothroyd 1992) that the above mechanism takes place more efficiently in most massive AGB stars. Abia et al (1993) found that only 2% of the galactic carbon stars are super-rich Li stars. However there is no information on the abundance of Al in these stars. We do not have a satisfactory explanation for the presence of super-rich Li galactic carbon stars. Most of the Li rich galactic carbon stars may be in the mass range of 2 to $3M_\odot$. However the models of Sackmann and Boothroyd (1992) showed that stars of masses 4 to $6M_\odot$ can produce Li in the envelope as a consequence of hot-bottom burning. Our understanding of nucleosynthesis during the hot bottom burning is far from complete.

HD 56126 (Parthasarathy et al 1992, Klochkova 1995) and HD 187885 (Van Winckel et al 1996) are the only other two post-AGB stars which show clear evidence of AGB nucleosynthesis and third dredge-up. Both are found to have carbon-rich and overabundant in s-process elements. The average abundances of post-AGB stars HD 56126 and HD 187885 and a carbon star 187216 (Kipper and Jørgensen 1994) and IRAS 05341+0852 are plotted in Fig. 4.5. From the Fig. 4.5 it is clear that the abundances of IRAS05341+0852 are very much similar to AGB carbon star HD 187216. Both are metal poor, Li rich, carbon-rich and have large overabundance in s-process elements. Although HD 56126 and HD 187885 are carbon-rich post-AGB stars with similar physical parameters, they do not have overabundance of Li and Al. In these stars Li may have been produced during the Thermally Pulsing phase and then destroyed. The survival of Li last a few thermal pulses. Also the production of Li and Al depends on the temperature at the base of the convective envelope for Hot

Bottom Burning to occur. If the temperature at the base of the convective envelope is much less than 50 million degrees (Boothroyd et al 1995) then the conditions are not sufficient enough for efficient production of Al and Li. The presence of Li and Al in IRAS 05341+0852 indicates that it may have higher temperature at the base of the convective envelope for the production of Li and Al during the hot bottom burning. Also it may depend on the core mass of these stars and their mass-loss episodes. HD 4671 is the only other high latitude supergiant which shows overabundance of Li and mild enhancement in s-process elements which are two chief characteristics of post-AGB stars. However star is found to have underabundance in carbon. This is not understood. The evolutionary status of this object needs further study.

IRAS 05341+0852 is the only star which is carbon-rich, metal-poor ([Fe/H]=−1.0), overabundant in s-process elements, Li and Al. The abundance pattern of IRAS 05341 +0852 is consistent with the predictions of evolutionary models of AGB stars with HBB. However the abundance of Fe ([Fe/H]=−1.0) in IRAS 05341 +0852 and its post-AGB nature, luminosity indicate that it is a low-mass star belonging to the old disk or halo population, which is now in post-AGB stage of evolution.

4.7 Conclusions

From an analysis of high resolution spectra of IRAS 05341+0852 we derived atmospheric parameters: T_{eff}=6500 K, log g=0.5, ξ_t=5 km s^{-1} and [M/H]=−1.0. We found star to be metal-poor with [Fe/H]=−1.0. The radial velocity measurements yield V_r= 25 km s^{-1} which indicates that the star belongs to old disc population. The study of chemical composition of this star yields the following quantitative results:

1. Overabundances of ([C/Fe]=1.03) and ([N/Fe]=1.21) indicate that both H- and He- burning products are brought onto the surface during the dredge-up on AGB.

2. Large overabundances of s-process elements (Y,Ba, La, Ce, Sm etc) strongly indicate that star has gone through third dredge-up episodes.

3. Overabundance of Li ([Li/Fe]≤=2.5) and Al ([Al/Fe]=1.1) in this star are consistent with the theoretical calculations of Li production in the Hot Bottom Burning at the base of the convective envelope of AGB star (Lattanzio 1993, 1996; Mowlavi 1995)

The position of star in the HR diagram, high galactic latitude, presence of detached cold dust shell, asymmetry in Hα profile, low metallicity, overabundances of Li and CNO elements, large ratio of C/O$\leq$2.18, normal sulphur abundance and large abundances of s-process elements clearly establish that IRAS 05341+0852 is low-mass carbon-rich post-AGB star evolved from carbon-rich AGB star.

Chapter 5

Chemical composition of post-AGB stars HD 179821 (G5 Ia), HD 70379 (F6I) and IRAS 18095+2704)

5.1   Introduction

The chemical composition of bright post-AGB stars has been recently reviewed by
Bond (1991) and Luck (1993). In these reviews they discussed the chemical compo-
sition of luminous (low gravity) high latitude supergiants which were found to show
detached cold dust shells with far-IR colours similar to planetary nebulae
(Parthasarathy and Pottasch 1986) and igh latitude low gravity A type supergiants
with warm dust shells (Lamers et al 1986; Waelkens et al 1992). Bond (1991) con-
cluded that the photospheric CNO abundance pattern in such stars are distinctly
atypical of normal population I supergiants, and clearly indicate that these stars
have burned helium. There are few post-AGB supergiants like HR 4049, HD 52961
etc
(Waelkens et al 1991, 1992) which were found to show extreme underabundance
of Fe and other refractory elements, and nearly normal (solar) abundances of CNO.

Bond (1991) proposed the dust grain formation as the depletion mechanism.

The observed abundance pattern of post-AGB supergiants indicates the following groups:

I) Post-AGB stars with no significant underabundance of Fe, slightly overabundant in CNO with respect to normal Population I supergiants. These stars have oxygen-rich circumstellar dust shells. The high latitude F- supergiant HD 161796 is a good example of stars belonging to this group (Luck 1993).

II) Post -AGB stars showing extreme underabundance of Fe and other refractory elements, and nearly normal CNO, S and Zn. Stars belonging to this group are HR 4049, HD 52961 etc (Waelkens et al 1991, 1992). The underabundance of Fe and other refractory elements is due to the dust grain condensation. The abundance pattern is correlated with the condensation temperatures (Bond 1991; Van Winckel et al 1992; Parthasarathy et al 1992) indicating that the depleted refractory elements are locked up in circumstellar dust grains.

III) Post-AGB stars belonging to this group are carbon-rich and overabundant in s-process elements indicating that they have gone through the third dredge-up during their AGB stage of evolution. The star IRAS 05341+0852 is a good example for which we reported the chemical composition in Chapter 4. The other two post-AGB F supergiants showing overabundance of carbon and s-process elements are HD 56126 (Parthasarathy et al 1992; Klochkova 1995) and HD 187885 (Van Winckel et al 1996).

IV) The high latitude low gravity hot post-AGB supergiants were found to show underabundance of Fe and significant underabundance of carbon indicating that these are old disc or halo stars in post-AGB stage of evolution (McCausland et al 1992). The abundance pattern of these stars indicates that they left the AGB before under-going third dredge-up.

Only for a few post-AGB stars in the above mentioned groups detailed chemical composition analysis is available. In order to further understand the abundance pattern of post-AGB F and G supergiants we selected HD 179821, HD 70379 and IRAS 18095+2704. These three stars have detached cold dust shells with characteristics

Table 5.1: Basic data

	HD 179821	HD 70379	IRAS 18095+2704
Sp.type	G5 Ia	F6I	F3 Ib
$\alpha(1950)$	$19^h11^m24^s.9$	$08^h18^m42^s.6$	$18^h09^m30^s.9$
$\delta(1950)$	$00°02'19''$	$19°05'30''$	$27°04'28''$
l	$36°$	$241°$	$53°.8$
b	$-5°$	$10°$	$20°.2$
V	8.30	8.85	10.4
B-V	1.40	0.68	1.03
E(B-V)	0.6	0.3	0.7

similar to high latitude post-AGB stars and planetary nebulae (Parthasarathy and Pottasch 1986; Pottasch and Parthasarathy 1988). The basic parameters of three post-AGB candidates are given in Table 5.1 and the details of these three stars are given below. In this chapter we report an analysis of high resolution optical spectra of these stars and discuss their abundance pattern and evolutionary status.

5.2 Individual stars

5.2.1 HD 179821

Having nearly the coldest IRAS colours (12 μm=31 Jy, 25 μm=650 Jy, 60 μm=520 Jy and 100 μm=170 Jy) among evolved stars, this object has gained considerable attention in recent literature as it displays many unusual properties. We will briefly overview the recent literature on this object.

This is a V=8.4 star of spectral type G5 I_a (Buscombe 1984; Hrivnak et al 1989). In the CO survey of cold IRAS objects, Zuckerman and Dyck (1986) have detected CO molecular emission in HD 179821. It has large CO radial velocity (V_r=100 km s^{-1}) with respect to local standard of rest and also it has large out flow velocity (V_{exp}= 32
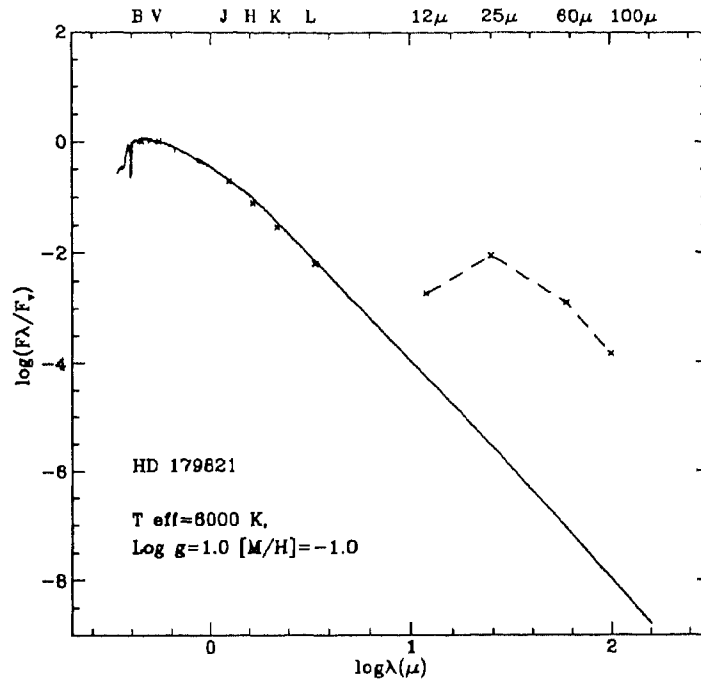
Figure 5.1: *Spectral energy distribution of HD 179821 is compared with Kurucz model atmosphere (solid line). The SED indicates that star has detached cold dust shell and no hot dust shell (no near-IR excess)*

km s^{-1}). Based on its kinematical properties, large IRAS fluxes and out flow velocity, they suggested that the star might once have been a runaway O-type star. Pottasch and Parthasarathy (1988) for the first time,have discussed the post-AGB nature of this star based on its far-IR fluxes. The spectral energy distribution (SED) of this source closely resembles that of high latitude post-AGB candidate HD 161796 and its IRAS colours are similar to planetary nebulae. The large far excess of this star has been attributed to large scale mass-loss in the preceding AGB phase of evolution. The studies of SED from 0.4 μm to 100 μm (Hrivnak et al 1989; van der Veen et al 1989, 1994) points out that the star has a detached cold ($\approx$ 130 K) dust shell (Fig 5.1) and no hot dust component indicating recent cessation of mass-loss. However very recently Hawkins et al (1995) discovered an extended nebula around HD 179821 at near-IR wavelengths and they suggested that it is an extremely massive star which has
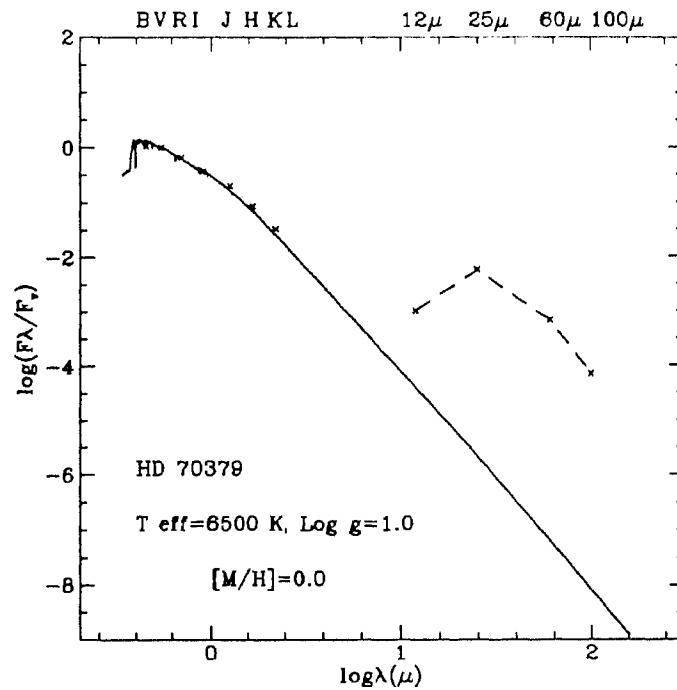
Figure 5.2: *Spectral energy distribution of HD 70379 is compared with Kurucz model atmosphere (solid line). The SED indicates that star has detached cold dust shell and no hot dust*

recently undergone an enormous mass-loss. They predicted the total observable mass in HD 179821 circumstellar envelope is around $8M_\odot$. Polarimetric and coronagraphic near-IR images (Kastner and Weintraub 1995) revealed the presence of extended dust reflection nebula around HD 179821. Under the assumption that the star lies at its kinematical distance (6 kpc), Kastner and Weintraub (1995) also suggested that its circumstellar envelope has a dynamical lifetime of 5000 yr, containing $\approx$ 5 $M_\odot$ of gas and dust and it was likely ejected during a prior OH/IR supergiant phase.   Thus HD 179821 either classified as a post-AGB star descended from a low- or intermediate-mass progenitor or an yellow supergiant descended from massive population I supergiants. Still there is no consensus on the evolutionary status of this dusty G5 supergiant. In this paper we tried to identify the nature of this enigmatic object using the chemical composition analysis based on the high resolution spectra
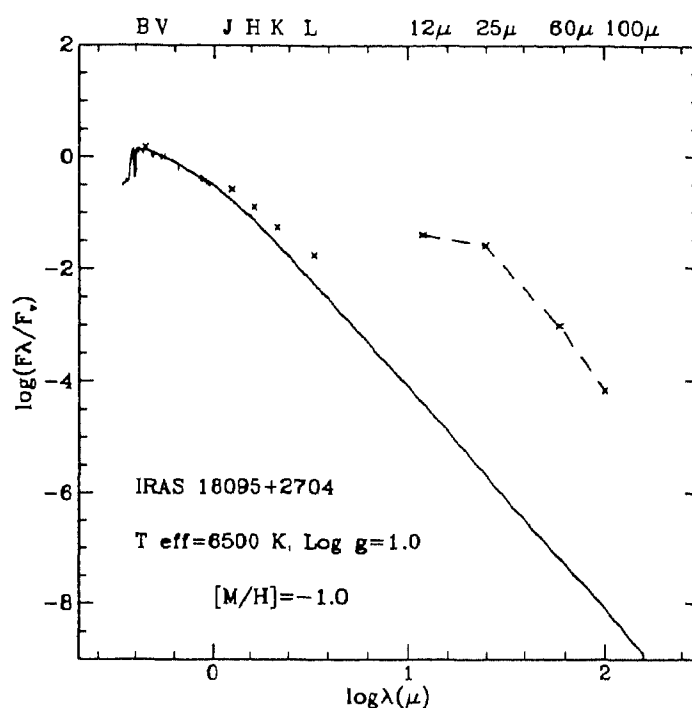
Figure 5.3: *Spectral energy distribution of IRAS 18095+2704 is compared with Kurucz model atmosphere (solid line). This clearly indicates that star has detached cold dust shell and no near-IR excess*

obtained at Isaac Newton Telescope (INT).

5.2.2   HD 70379

This is a F6 supergiant of V=8.86. The SED of (Fig. 5.2) this source from 0.44 μm to 3.4 μm fits very well with the Kurucz atmospheric model: T_{eff}= 6500 K and log g=1.0. This object has been suggested as a low-mass post-AGB star (Reddy and Parthasarathy 1996) based on its SED and low resolution spectra. Here we present the chemical composition analysis to ascertain the post-AGB nature of this candidate.
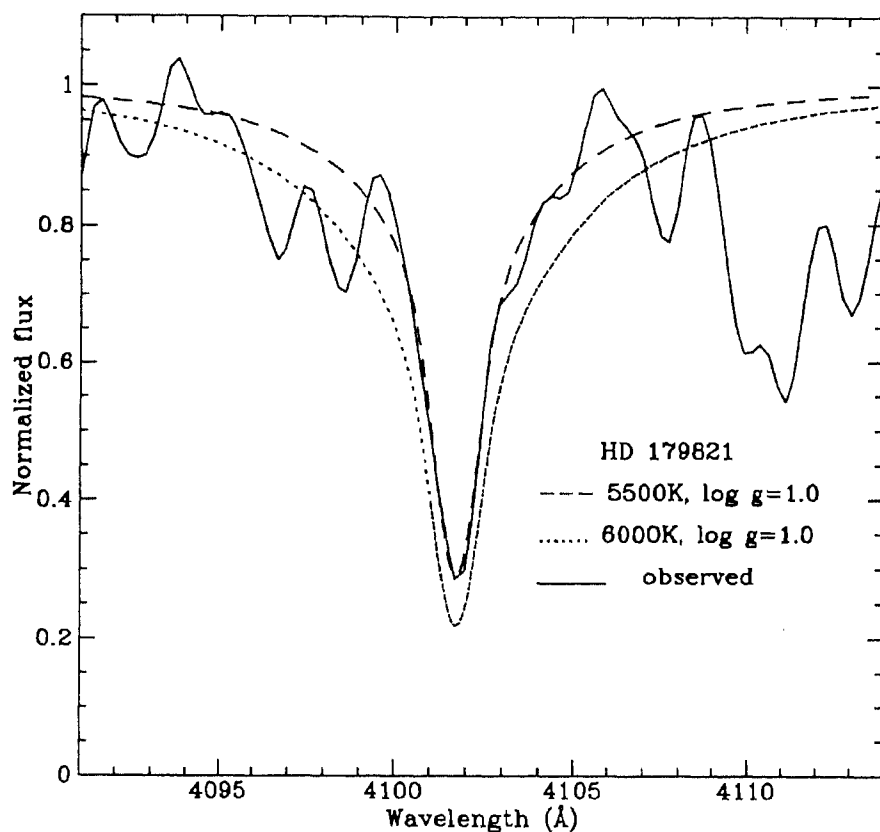
Figure 5.4: *Comparison of Kurucz (1979) calculated Hδ profile with observed Hδ profile of HD 179821*

5.2.3   IRAS 18095+2704

Hrivnak et al (1988) identified the optical counterpart of this object as an F3 supergiant of V=10.54. This star has been suggested as a good candidate for protoplanetary nebula (Hrivnak et al 1988) based on its SED and galactic position. van der Veen et al (1989) estimated the distance of this object to be d=2.4 kpc, and the distance from the Galactic plane to be z=0.8 kpc. Hrivnak et al (1988) also determined a colour excess of E(B-V)=0.78 mag, and concluded that most of this excess is caused by a circumstellar dust envelope created as a result of extensive mass-loss at the rate of 3×10^{-5} M$_{\odot}$ yr^{-1} during the AGB stage. From modeling
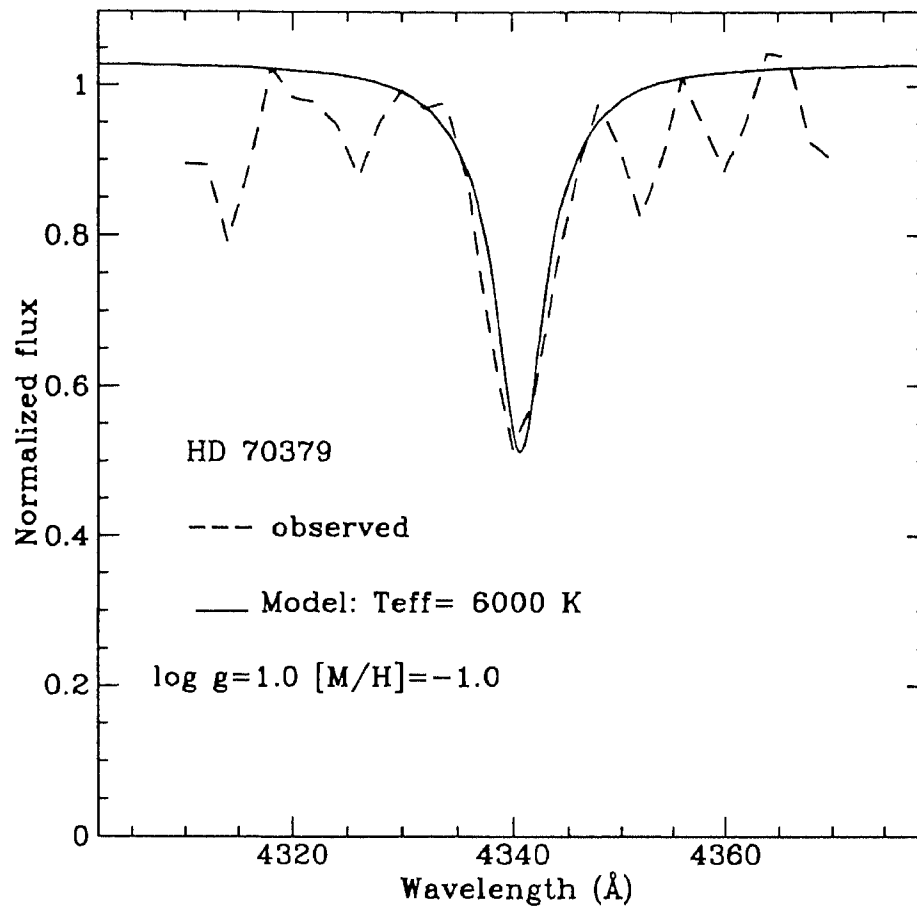
Figure 5.5: *Observed Hγ profile is fitted with Kurucz theoretical Hγ profile of model:*
6000 K, log g=1.0 and [M/H]=0.0

of the spectra in the 0.35 μm-100 μm spectral region , these authors concluded that
IRAS 18095+2704 began to evolve from the AGB about 265 yrs ago and this object is
a very young proto-planetary nebula. The SED of this star is well fitted with SED
of Kurucz (1979) model atmosphere: T_{eff}=6500 K, log g=1.0 and [M/H]=−1.0 (Fig
5.3). The SED of this object shows that the star has detached cold dust shell and no
hot component indicating mass-loss cessation. The presence of OH, 10 μm silicate
features (Eder et al 1988; Volk and Kwok 1987) and non-detection of CO (Nyman
et al 1992) suggest that IRAS 18095+2704 is a oxygen-rich post-AGB star. Recently
Klochkova (1995) carried out the chemical composition analysis of this object and
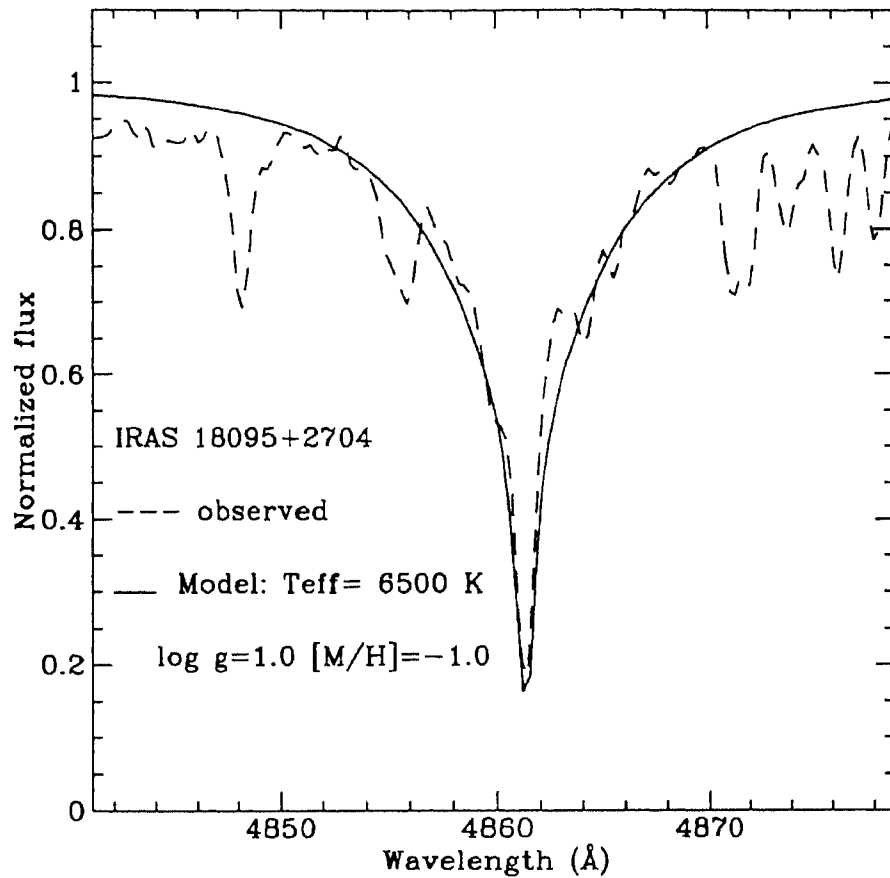
Figure 5.6: *Observed Hβ profile is fitted with Kurucz theoretical Hβ profile of model: 6500 K, log g=1.0 and [M/H]=−1.0*

found anomalous elemental abundances.

5.3 Atmospheric parameters: T_{eff}, log g, ξ_t and metallicity

The photospheric parameters T_{eff} and log g are estimated using the SEDs of the program stars. Each observed SED is compared with the Kurucz model atmosphere with different T_{eff} and log g. The best fitted Kurucz models with the observed SED

Table 5.2: Derived atmospheric parameters of stars from various methods

star	Photometry		Balmer profiles		Adopted values			
	T_{eff}	log g	T_{eff}	log g	T_{eff}	log g	ξ_t	[M/H]
	(K)	dex	(K)	dex	(K)	dex	km s^{-1}	dex
HD 179821	6000	1.0	5500	1.0	5500	0.5	6	-1.0
HD 70379	6500	1.0	6000	1.0	6500	1.0	5	0.0
IRAS18095+2704	6500	1.0	6500	1.0	6500	1.0	5.5	-1.0

are shown for all the objects (Figs. 5.1,5.2,5.3). We also determined T_{eff} and log g using the strengths and wings of the Balmer profile respectively. We fitted theoretical Balmer profiles (Kurucz 1979) calculated for various model atmospheres with the observed profiles (Figs. 5.4,5.5,5.6). The deduced values from Balmer profiles are given in Table 5.2. The physical parameters derived from the above methods are used in determining accurate T_{eff} , log g, microturbulent velocity (ξ_t) and metallicity using excitation balance and ionization equilibrium of metallic lines as discussed in the previous chapters. The final adopted model atmosphere parameters used in the chemical composition analysis are given in Table 5.2.

5.4 Results

5.4.1 HD 179821

Derivation of elemental abundances using line analysis method (Chapter 3) is a bit risky, for stars of late spectral type such as HD 179821 (G5 supergiant). It is more likely that the measured EWs are blended with nearby lines and giving large un-certainties in derived abundances. This problem is more acute in the case of blue regions, where defining the accurate continuum itself is difficult because of severe line and continuum opacities. Thus we restricted our abundance analysis only to spectral ranges > 4600Å. To avoid large uncertainties due to blending, we derived abundances mostly by fitting the calculated spectra to the selected observed regions

(Fig. 5.7) taking into account the possible blends. From the analysis of SED, Balmer profile fittings, spectral line analysis and spectral type we found model atmosphere with T_{eff}=5500 K, log g=0.5, [M/H]=−1.0 and microturbulent velocity ξ_t=6 km s^{-1} may reasonably represent the atmosphere of HD 179821. The average elemental abundances   derived using the above model by spectrum synthesis analysis are given in Table 5.3. We also derived abundances using models with T_{eff}=5000 K, log g=0.5. The results obtained (Table 5.3) also support that the star is metal-poor, and C and s-process elements are overabundant relative to Fe. We found HD 179821 is a metal-poor ([Fe/H]=−0.9) based on the analysis of 25 Fe I lines. This is confirmed by abundances of other iron peak elements like Ca, Ti, Cr and Ni ([Ca/H]=−0.96., [Ti/H]=−1.22., [Cr/H]=−1.1 and [Ni/H]=−1.08). However, ionized metallic lines ([Ti II/H]=−0.3., [Cr II/H]=−0.65., [Fe II/H]=−0.3) yield large abundances compared to neutral lines. The fittings of synthetic spectra to observed regions in Fig. 5.7 show that only neutral lines of Ca and Fe are matched with the adopted model and metallicity of [Fe/H]=−0.9 and ionized lines Fe II and Ti II are not matched. The large discrepancy between ionized and neutral lines may be because of two reasons: one is that ionized lines are too strong ($\approx$300-600mÅ) to use in abundance analysis as these are affected by turbulence and severe blending and other one is that since the atmosphere of HD 179821 is highly extended (log g=0.5) Non-LTE effects on the ionized lines may be playing greater role in the abundance discrepancy. The carbon found to be overabundant ([C/Fe=0.85]) which is an average value derived from three carbon lines at 4769.99Å, 5052.15Å and 6588.99Å. Mg and Si are found to be normal relative to iron ([Mg/Fe]=0.32, [Si/Fe]=0.45) within errors. The abundance of Zn ([Zn/Fe]=−0.15) is based on two Zn I lines at 4722.163Å (60mÅ) and 4810.537Å (212mÅ). The abundance values derived both from spectrum synthesis and line analysis are in good agreement. The important results that come from the spectral analysis of HD 179821 is s-process elemental overabundance. The abundances of Zr, Ba and La are based on each single line and hence we believe uncertainties in these abundances may be large. However the abundance of s-process element Y has been measured from three lines which supports the s-process enrichment in HD 179821.

The errors involved in the abundances of HD 179821 may be larger as most of the
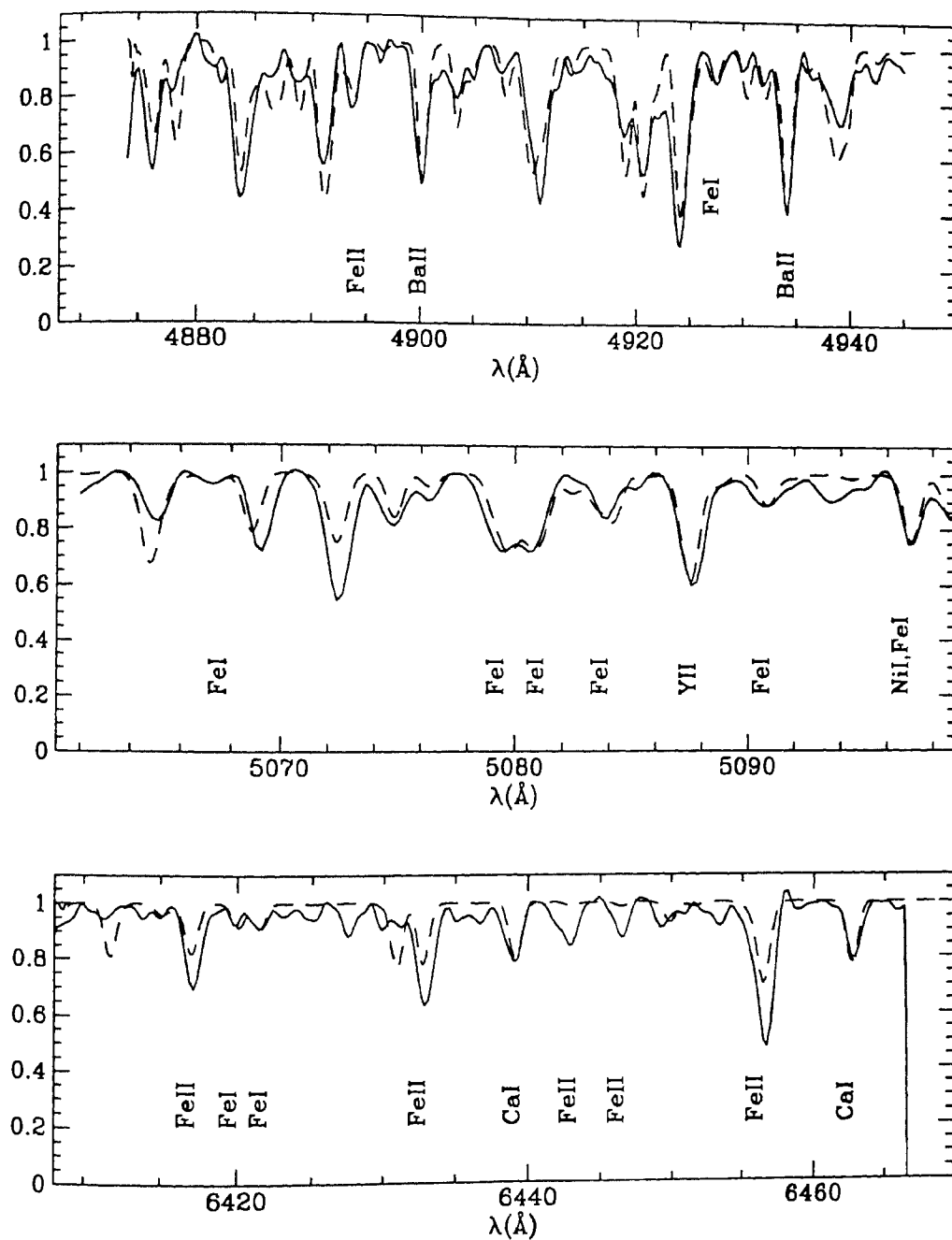
Figure 5.7: *The observed and calculated spectra of HD 179821 in the regions 4870 - 4950Å, 5060 - 5100Å and 6410 - 6470Å showing Ba, Y and Fe lines. Solid lines: observed spectra and Dotted lines: calculated spectra with [Fe/H]=−0.9, [Y/H]=0.2 and [Ba/H]=−0.1.*

abundances are determined from spectrum synthesis. This is because, it is a G-type star and the spectral resolution is not very high. Uncertainties in the abundances may be due to incomplete line list. Accurate gf values are not available for all the lines used in the synthesis analysis. Estimating uncertainties in the abundances of HD 179821 is difficult, due to possible missing lines in the line lists and possible errors in gf values. Another source of error is the uncertainty in derived atmospheric parameters. The analysis of comparing observed Balmer profiles and SED with the theoretical ones, and ionization and excitation balance of Fe I and Fe II lines yield an uncertainty in T_{eff} by $\pm$ 500 K, log g by ± 0.5 dex and ξ_t by $\pm$ 1 km s^{-1}. Change of 500 K in T_{eff} has very little effect on the abundances for higher excitation lines such as C, N, O , Mg, and Si (Table 5.3). However there is noticeable change in the abundance values of iron peak and s-process elements. The uncertainties in log g and ξ_t have little effect on the abundances. The net errors in our abundance values of HD 179821 due to above mentioned uncertainties in the method of analysis may be atleast : $\pm$ 0.2 dex in carbon, $\pm$ 0.3 dex in Mg and Si, $\pm$ 0.2 dex in Fe and Ni , $\pm$ 0.3 dex in Y, Zr, Ba and La.

5.4.2 HD 70379

The chemical composition analysis of HD 70379 (IRAS 08187-1905) is based on high resolution echelle spectra in the range 5010-7200Å. The list of lines,their EWs and oscillator strengths used in this study are given in the Apendix. We used only lines with EWs $\leq$ 150mÅ, to avoid possible blending, turbulence and NLTE effects.

Elemental abundances of HD 70379 have been derived using model atmosphere: T_{eff}=6500 K, log g=1.0, ξ_t=5 km s^{-1} and [M/H]=-0.5 (Table 5.2). Average abundances of each element derived from this model are presented in Table 5.4.

We found from this analysis that HD 70379 is slightly metal-deficient ([Ca/H]=-0.5, [Sc/H]=-0.6,[Ti/H]=-0.6, [V/H]=-0.4, [Cr/H]=-0.4, [Fe/H]=-0.3 and [Ni/H]=-0.3). We found carbon to be overabundant ([C/Fe]=0.2) relative to Fe. The derived carbon abundance is based on 7 well defined lines. The oxygen triplet lines at 6156Å are badly blended with metallic lines. The profiles are not symmetric, (Fig 5.8) and
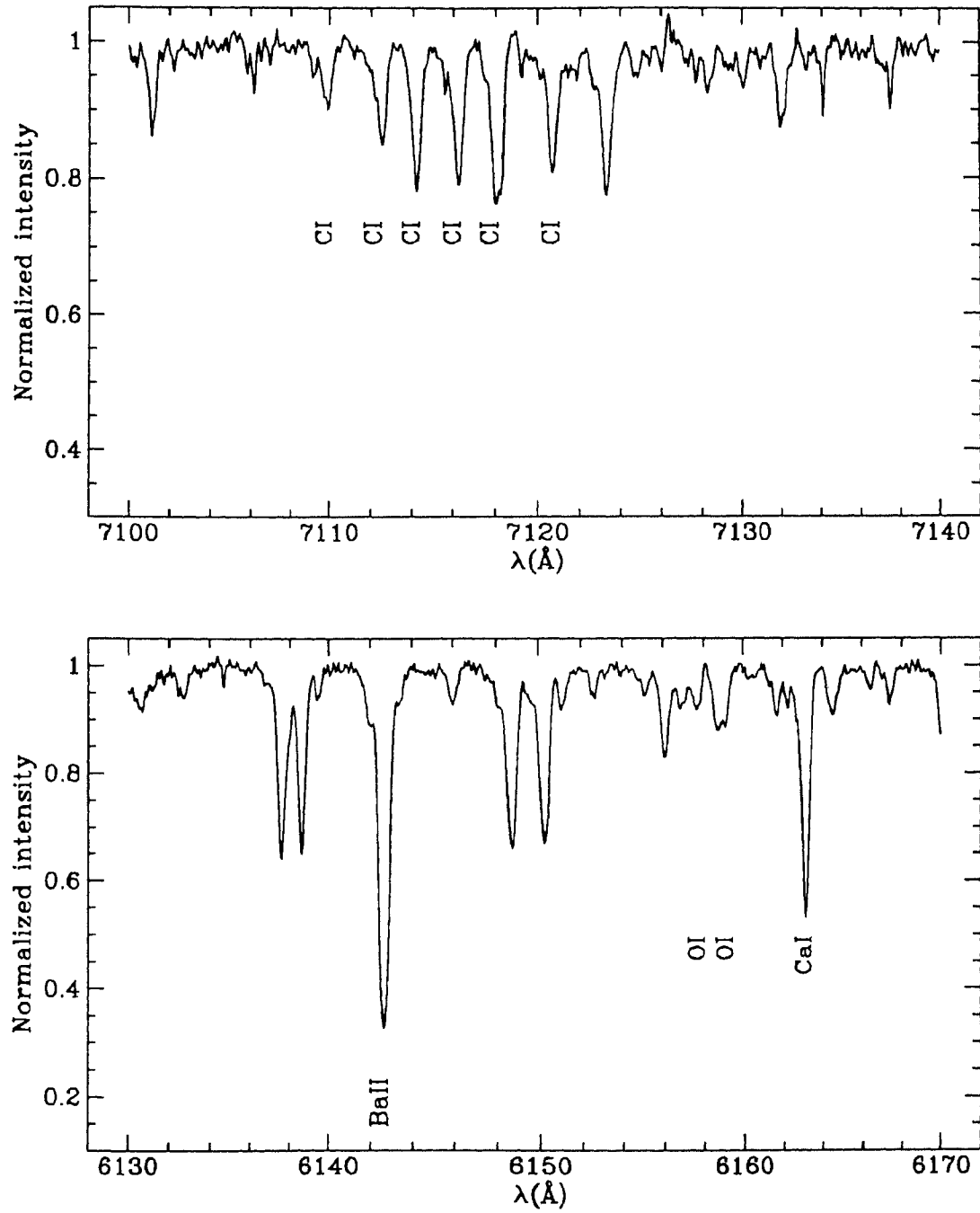
Figure 5.8:   *The spectra of HD 70379 in the regions of 7120Å and 6150Å showing carbon and oxygen lines.*

hence we did not use them in our abundance analysis. We used oxygen forbidden line at 6363Å which yields an overabundance of oxygen ([O/Fe]=0.32) relative to Fe. Na ([Na/Fe]=0.33) and Si ([Si/Fe]=0.5) are found to be overabundant with respect to iron. However the Mg I line at 5711Å (Ew=90mÅ) gives normal abundance ([Mg/Fe]=0.1) and the other MgI line at 5172Å is too strong (Ew=433mÅ) to be used in abundance analysis. The abundance of sulphur ([S/Fe]=0.34) comes from 7 S I lines. Zn abundance ([Zn/Fe]=0.1) is based on single Zn I line at 6362.35Å. From the line analysis of HD 70379, we found mild enrichment in s-process elements. The abundance of light s-process element Y ([Y/Fe]=0.5) is derived from 7 Y II lines and the abundance of heavy s-process element Ba ([Ba/Fe]=0.43) from two Ba II lines at 5853Å and 6141Å. However the abundances of other heavy elements Nd ([Nd/Fe=−0.14) and Eu ([Eu/Fe]=−0.03) are underabundant similar to Fe.

We estimated uncertainties in the derived elemental abundances, due to uncertainties in the derived model atmosphere: $\pm$ 250 K in T_{eff}, ± 0.5 dex in log g and $\pm$ 1 km s^{-1} in ξ_t. Average uncertainties due to uncertainties in the model parameters are as follows: 0.1 dex in C , N, O, Mg, Si and S., $\approx$0.2 dex in iron group elements and 0.2 to 0.3 dex in Y, Ba, Nd and Eu abundances. Most of the derived abundances are the result of more than three lines (Table 5.4) for which internal scatter is represented by standard deviation (σ) in Table 5.4. The large internal scatter in the abundance of S (Table 5.4) mostly may be due to uncertain gf values and in less extent due to measured equivalent widths. Uncertainty in the abundances of O, Mg, Ti and Zn may be large ($\pm$ 0.2 dex - 0.3 dex) for which abundances are derived from single lines.

5.4.3   IRAS18095+2704

The photometry (Fig.5.3) and observed Balmer profile (Fig.5.6) indicate a temperature of 6500 K and log g=1.0. Using these values as starting values and excitation and ionization balance on Fe (Fe I and Fe II) lines, we determined atmosphere model:T_{eff}=6500 K, log g=1.0 ,ξ_t=4.5 km s^{-1} and [M/H]=−1.0 as appropriate model to IRAS18095+2704. The derived atmospheric parameters by us are in good agree-
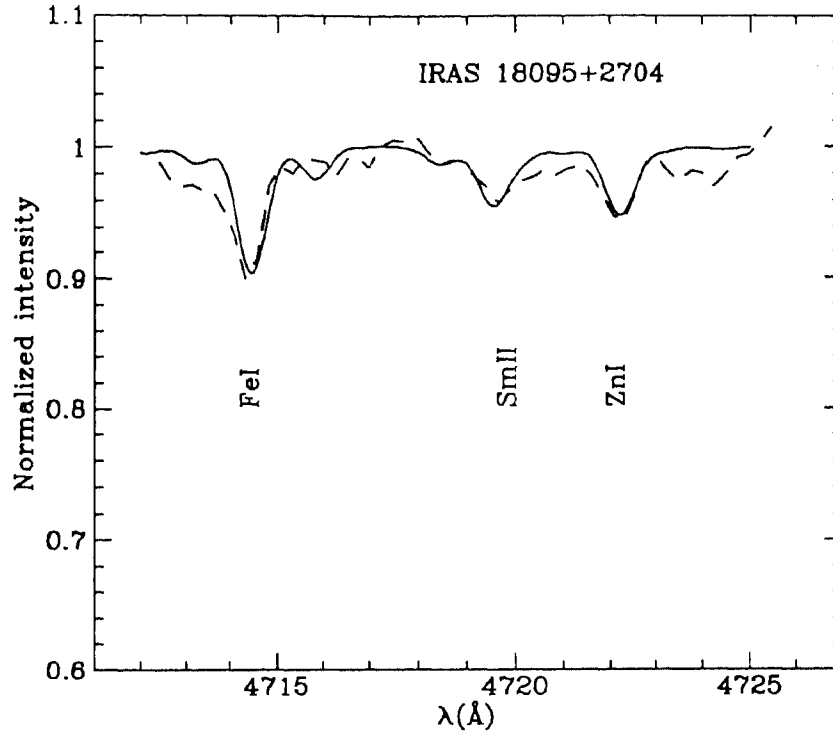
Figure 5.9: *Spectrum synthesis fit to the 4710 - 4730Å region of IRAS 18095+2704. dashed line: observed spectrum and Solid line: synthetic spectrum calculated for [Fe/H]=−0.7 and [Zn/H]=−0.7*

ment with that derived by Klochkova (1995): T_{eff}=6700 K, log g=1.1, ξ_t=4.5 km s^{-1} and [M/H]=−1.0. The average abundances of chemical elements derived from two model atmospheres are presented in Table 5.5. In our final analysis of abundances we adopted model atmosphere derived by Klochkova (1995) as it is derived from many Fe I and Fe II lines.

From our analysis we found it is moderately metal-deficient with [Fe/H]=−0.7. The carbon ([C/Fe]=0.2) and oxygen ([O/Fe]=0.7) are found to be overabundant which are similar to values of Klochkova (1995). However N ([N/Fe]=0.8) abundance deduced by us is 0.4 dex more than that of Klochkova value. The abundances of Mg, Si and S are in good agreement with the abundances derived by Klochkova. The anomalous elemental abundances as reported by Klochkova for neutral Ti, Ca and
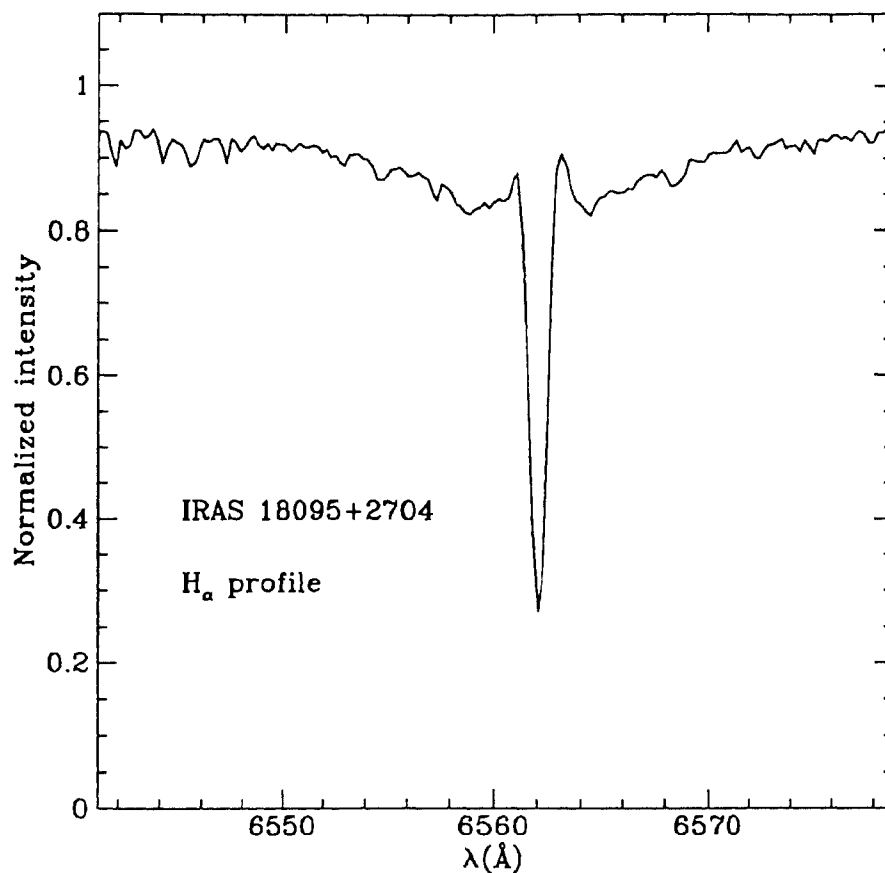
Figure 5.10: *The complex structure of Hα profile of IRAS 18095+2704 is shown*

Cr are not found in our study. Within the uncertainties of methods used and input parameters, we did not find any significant discrepancy between neutral and ionized lines of Ti and Cr. The derived Mn abundance ([Mn/Fe]=0.7) based on 4 reasonably good Mn I lines, confirms the overabundance of Mn I abundance of Klochkova (1995). We also found that the abundances of other iron peak elements Ni ([Ni/Fe]=−0.1) and Zn ([Zn/Fe]=0.0) are not overabundant relative to Fe. Klochkova reported large overabundance of Ni ([Ni/Fe]=0.7) and Zn ([Zn/Fe]=0.8). From line analysis and spectrum synthesis of Y II and Ba II lines we found the star to be deficient in s-process elements. Klochkova also found Y II and Ba II are underabundant, but he found La, Pr, Nd and Eu are overabundant relative to Fe.

Table 5.3: Average elemental abundances of HD 179821 derived from model atmosphere: T_{eff}=5000 K, and 5500 K, Log g=0.5 ξ_t=6 km s^{-1} and [M/H]=-1.0

element	#lines	T_{eff}=5000 K			T_{eff}=5500 K		
		$A_\star$	[X/H]	[X/Fe]	$A_\star$	[X/H]	[X/Fe]
C I	3	8.5	-0.05	1.20	8.5	-0.05	0.9
Mg I	1	7.0	-0.58	0.65	7.0	-0.58	0.37
Si I	1	7.1	-0.45	0.80	7.2	-0.35	0.6
Ca I	4	5.4	-0.96	0.29	5.6	-0.76	0.19
Ti I	3	3.9	-1.12	0.13	4.1	-0.9	0.05
V I	1	3.0	-1.0	0.25	3.6	-0.4	0.55
Cr I	2	4.6	$-.07$	0.18	4.9	-0.77	0.18
Mn	2	4.7	-0.69	0.56	5.0	-0.39	0.56
Fe I	25	6.3	-1.25	0.0	6.7	-0.95	0.0
Fe II	6	7.0	-0.55	0.0	7.3	-0.25	0.0
Ni I	6	5.17	-1.08	0.20	5.6	-0.65	0.3
Zn I	2	3.55	-1.05	0.20	3.8	-0.75	0.2
Y II	3	2.2	-0.04	1.21	2.4	0.16	1.1
Zr II	1	2.56	-0.04	1.11	2.8	0.2	1.2
Ba II	1	2.0	-0.13	1.12	2.0	-0.13	0.8
La II	1	1.00	-0.22	1.03	1.0	-0.22	0.73

The line-to-line scatter in the derived abundances (σ) is large. This is mostly due to the uncertainty in measured EWs as the spectrum has low S/N ratio. The analysis of SED , Balmer profiles and the abundances of Fe I and Fe II lines yield uncertainty in our derived atmospheric parameters: T_{eff} by $\pm$ 250 K, log g by $\pm$ 0.5 dex and ξ_t by $\pm$ 1 km s^{-1}. Uncertainties in the derived parameters contribute net errors in the abundance by $\pm$ 0.2 dex in C, N, O, Mg, Si and S and by $\pm$ 0.3 dex in iron peak and s-process elements.

Table 5.4: Elemental Abundances of HD 70379 for derived atmospheric model: T_{eff}=6500 K, log g=1.0 and ξ_t=5km s^{-1}

Element	# of lines	Average Abun.	STD(σ)	[X/H]	[X/Fe]
C I	7	8.65	0.13	0.10	0.42
[O I]	1	8.99		0.02	0.38
NaI	3	6.34	0.04	0.01	0.33
Mg I	1	7.27		−0.31	0.01
Si I	10	7.71	0.17	0.16	0.48
Si II	2	7.69		0.14	0.46
S I	7	7.23	0.20	0.02	0.34
Ca I	9	5.87	0.08	−0.49	−0.17
Sc II	6	2.61	0.19	−0.56	−0.24
Ti II	1	4.37		−0.65	−0.33
VII	2	3.57		−0.43	−0.11
Cr I	6	5.39	0.14	−0.28	0.04
Cr II	6	5.28	0.06	−0.39	−0.07
Fe I	55	7.19	0.11	−0.31	0.0
Fe II	9	7.18	0.12	−0.32	0.0
Ni I	10	6.0	0.11	−0.25	0.07
Zn I	1	4.44		−0.2	0.1
Y II	7	2.39	0.12	0.15	0.47
Ba II	2	2.24		0.11	0.43
NdII	4	1.04	0.16	−0.46	−0.14
EuII	2	0.16		−0.34	−0.03

Table 5.5: Elemental abundances of IRAS 18095+2704 derived from model atmosphere: T_{eff}=6500 K, log g=1.0, ξ_t=5.5 km s^{-1} and [M/H]=$-$1.0.

element	n	Model: T_{eff}=6500 K, log g=1.0 ξ_t=5.5 km s^{-1}, [M/H]=$-$1.0				T_{eff}=6700 K, log g=1.0 ξ_t=4.5 km s^{-1}, [M/H]=$-$1.0				Abun[a]
		Abun.	σ	[el/H]	[el/Fe]	Abun	σ	[el/H]	[el/Fe]	
C I	10	8.06	0.15	-0.50	0.45	8.10	0.2	-0.46	0.2	8.27
N I	3	7.98	0.1	-0.07	0.88	8.05	0.1	0.0	0.65	7.66
O I	1	8.7	-	-0.23	0.72	8.75	-	-0.2	0.45	8.74
Mg I	3	7.1	0.10	-0.48	0.42	7.35	0.15	-0.23	0.42	7.42
Si I	4	7.2	0.2	-0.35	0.60	7.4	0.23	-0.15	0.5	7.48
S I	2	6.8	0.1	-0.4	0.55	7.0	0.13	-0.21	0.44	6.96
Ca I	4	5.47	0.2	-0.89	0.06	5.8	0.4	-0.56	0.1	5.84
Sc II	2	1.97	0.2	-1.13	-0.18	2.3	0.2	-0.7	-0.05	2.25
Ti I	2	4.4	0.1	-0.62	0.33	4.64	0.02	-0.38	0.27	5.68
Ti II	3	4.17	0.3	-0.85	0.1	4.26	0.2	-0.76	-0.1	4.05
Cr I	4	4.7	0.4	-0.97	0.0	5.0	0.2	-0.67	-0.02	6.02
Cr II	4	4.7	0.2	-0.97	0.0	4.9	0.2	-0.77	-0.12	4.98
Mn I	3	5.14	0.3	-0.25	0.7	5.39	0.3	0.0	0.65	5.12
Fe I	23	6.58	0.2	-1.0		6.9	0.3	-0.65		6.71
Fe II	10	6.62	0.2	-0.9		6.9	0.2	-0.65		6.73
Ni I	4	5.25	0.1	-1.02	-0.07	5.55	0.13	-0.7	-0.05	6.13
Zn I	2	3.8	0.1	-0.9	0.05	4.05	0.1	-0.55	0.1	4.60
Y II	4	0.67	0.2	-1.57	-0.6	1.0	0.14	-1.24	-0.6	1.42
Ba II	3	0.93	0.3	-1.2	-0.25	1.4	0.14	-0.73	-0.1	1.13

Table 5.6: Radial velocity measurements of program stars

star	Date of observation	V_m (km s^{-1})	V_{hc} (km s^{-1})	V_r (km s^{-1})
HD 179821	244 8213.5	76±4	−22.83	54
HD 70379	245 0061.5	45±2	19.88	65
IRAS18095+2704	244 8400.5	−45	10.6	−35
	244 8902.5	−21	−15.3	−36
	244 9173.5	−33	−2.85	−36
	244 9163.5			−32.5[a]

Note:-

(a) Klochkova 1995

5.4.4 Radial velocities

Measurement of radial velocities is one of the key results, obtained from high resolution spectra. We measured Doppler shifts from well defined absorption lines. The measured radial velocities (V_m) for the three stars are given in Table 5.6. The measured velocities are corrected for the heliocentric corrections (V_{helio}) and the final systemic velocities (V_r) relative to heliocenter are given in Table 5.5. The derived velocities of all three stars suggest that they belong to either intermediate thick disc ($V_r \approx 40$ km s^{-1}) or old disc ($V_r \approx 25$ km s^{-1}) population stars. The derived velocities from the spectra of IRAS18095+2704 are in good agreement with the velocity obtained by Hrivnak et al (1988) and by Klochkova (1995). Velocity measurements of this star in a span of about 5 yrs, do not indicate any variations (Table 5.6). The radial velocity (V_{LSR}=54 km s^{-1}) derived from our spectra of HD 179821 is less than the velocity (V_{LSR})=100 km s^{-1}) obtained by Zuckerman and Dyck (1986) from CO observations. We measured doppler shifts from both neutral and ionized lines of HD 179821. We found a large systemic velocity of V_r=65±1 km s^{-1} for HD 70379.

Table 5.7: Chemical composition of HD 179821, HD 70379 and IRAS 18095+2704 are compared with the abundances of average yellow massive supergiants and dwarfs

Star	[Fe/H]	[C/Fe]	[N/Fe]	[O/Fe]	[hs/Fe]
HD 179821	−0.6 to −0.9	0.9	-	-	0.9
HD 70379	−0.3	0.4	-	0.4	0.4
IRAS18095	−0.8	0.45	0.88	0.72	−0.4
Yellow supergiants	0.0	−0.15	0.07	−0.2	
Dwarfs	0 to −2.0	0.0	0.0	≤ 0.4	0.0

5.5 Discussion

The chemical composition of three program stars along with massive yellow supergiants (Barbuy et al 1996) and dwarfs (Wheeler et al 1989) is summarized in Table 5.7. Several remarkable characteristics are revealed by the chemical composition analysis of these sources. We discuss each of these stars in detail.

From the Table 5.7 it is clear that HD 179821 is neither a massive yellow supergiant nor a dwarf. The chemical composition of HD 179821 clearly differs from the average chemical composition of yellow supergiants and dwarfs. The yellow supergiants have elemental abundances: [Fe/H]=0.0, [C/Fe]=−0.2, [N/Fe]=0.1, [O/Fe]=−0.2. However HD 179821 is found to be metal-deficient ([Fe/H]= −0.9) which argues against the massive population I supergiants. The low metallicity of this object indicate that the star may be a low-mass star belonging to old thick disc or halo population group of stars. HD 179821 shows evidence of carbon enrichment with carbon abundance [C/Fe]=0.9 unlike yellow supergiants and dwarfs (Table 5.7). We could not derive abundances of O and N as our observed spectral ranges did not cover the spectral lines of O and N. The large radial velocity coupled with low-metallicity implies that HD 179821 may not be a massive supergiant. The over-abundance of carbon is expected only in those low and intermediate-mass stars which have undergone He-burning via the triple α reaction which occurs in the He shell flashes and third dredge-up mixing episodes during the AGB phase of evolution (Iben and Renzini 1982). The impor-
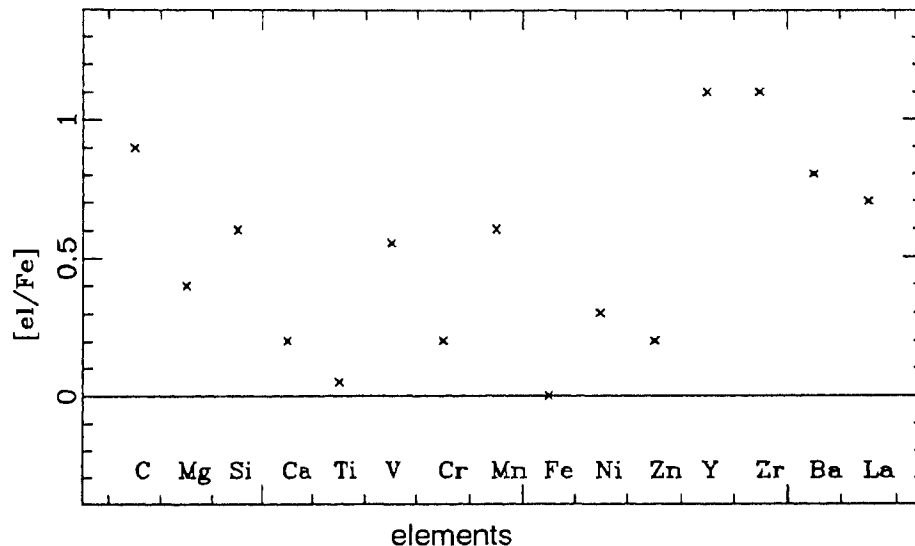
Figure 5.11: Chemical composition of HD 179821

tant result of our quantitative abundance analysis of HD 179821 is the overabundance of the s-process elements like Y, Zr, Ba and La. The enrichment of s-process elements suggests that the star has undergone the predicted nucleosynthesis and dredge-up processes on the AGB phase of evolution. The normal abundance of Zn ([Fe/Zn]=0.2) means that the overabundances of C and s-process elements are due to evolutionary effects and not because of depletion of iron peak elements (Van Winckel et al 1992). With its large radial velocity, chemical composition, HD 179821 resembles a known post-AGB star HD 56126 (V_r=100 km s^{-1}, [Fe/H]=−1.0).

Recently Kastner and Weintraub (1995) and Hawkins et al (1995) suggested that HD 179821 may be a massive yellow supergiant with circumstellar dust mass of around 5-8M$_\odot$, caught in between RGB and Wolf Rayet phase. Based on the post-AGB interpretation of HD 179821 (Pottasch and Parthasarathy 1988., van der Veen et al 1994) and on our chemical composition and atmospheric parameters, we estimate dust and stellar parameters. We assume core mass (M$_c$) of 0.6M$_\odot$ for HD 179821. This is a valid assumption for the central stars of post-AGB stars and PNe (Chapter 2). Using M$_c$=0.6M$_\odot$, the derived T$_{eff}$=5000 ±500 K and log g= 0.5±0.50 (Table 5.2) and

from an equation 4.1 (chapter 4), we estimate $M_v = -4$ to -5. We estimated total reddenning (dust+ISM) $A_v \approx = 2.0$. Extinction due to ISM is estimated from hot O and B stars in the direction of HD 179821. From values $A_v = 2.0$, $V = 8.4$ and $M_v = -4$ to -5, distance modulus ($M_v = (m_v - A_v) + 5 - 5 \log r$) yields distance (r) in the range 1 to 2 kpc. From the derived distance and angular size of $9''$(Kastner and Weintraub 1995) we deduced linear size of the nebula to be of the order 0.04 - 0.09 pc. Using circumstellar CO expansion velocity $V_{exp} = 30$ km s^{-1} and linear size of the nebula we derive the dynamical life time (t_{dyn}) of the nebula be around 800 - 1600 yrs. We also estimated dust mass (M_d) of the order of $4 \times 10^{-3} M_\odot$ using an equation 2.2 (see chapter 2). The M_d/t_{dyn} gives the mass-loss of the order of $5 \times 10^{-6} M_\odot$ yr^{-1}. These derived values are in agreement with the values derived from the optically thin model fits for the detached cold dust shells of post-AGB stars by van der Veen et al (1994). van der Veen et al (1994) also noted that the spectral energy distribution from 1 μm - 100 μm of HD 179821 is similar to a carbon-rich post-AGB star HD 187885 (Van Winckel et al 1996). Another important point to be noted is that the non-detection of HCN toward HD 179821 is attributed to the recent cessation of mass-loss (Hrivnak et al 1989) which is also suggested by its low IRAS variability index VAR=0 (see chapter 2 for details). Presence of strong HCN is the characteristic of heavily mass losing supergiants (Bujarrabal et al 1992; Nercessian et al. 1989). However the most outstanding problem for the post-AGB interpretation is the large expansion velocity of dust envelope.The typical expansion velocities for the post-AGB stars are in the range of 15-20 km s^{-1}.

Thus we conclude that HD 179821 is most probably a low- or intermediate-mass post-AGB star in transition from AGB to PN, based on our abundance analysis results, radial velocity, large displacement (Z=200 pc) from galactic plane, far-IR excess similar to PNe and its loci in the H-R diagram.

The abundance results of HD 70379 show that it is slightly metal-poor ([Fe/H]=-0.3) and overabundant in C ([C/Fe]=0.4) and O ([O/Fe]=0.4. The abundance pattern of HD 70379 is different from that of normal population I supergiants which have [Fe/H]=0.0, [C/Fe]=-0.6, [N/Fe]=0.5, [O/Fe]=-0.4 (Luck and Lambert 1985). Unfortunately we do not have information about the abundance of nitrogen in our ob-
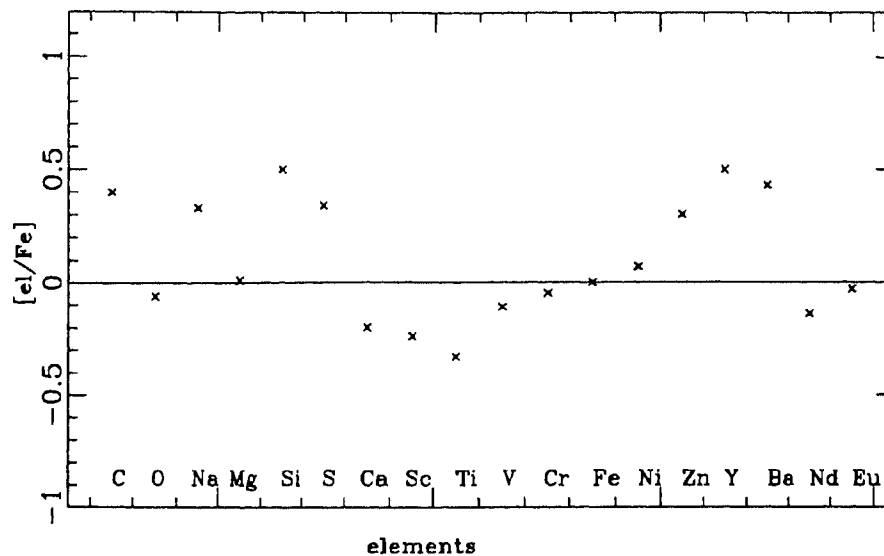
Figure 5.12: Chemical composition of HD 70379

served spectral range. The overabundance of C may be the result of mixing of He-burning products onto the surface on the AGB phase. During He-burning on the AGB, a neutron source may be ignited to drive synthesis of heavy elements by the s-process (see chapter 4). If HD 70379 is a post-AGB supergiant, one might expect to see overabundances of the heavy elements. Our elemental analysis indicates enrichment of s-process elements Y ([Y/Fe]=0.5) and Ba ([Ba/Fe]=0.4). However the other heavy elements Nd and Eu are similar to Fe.

The slow α-capturing elements Na ([Na/Fe]=0.3), Si ([Si/Fe]=−0.5) are also enhanced with respect to Fe which are expected in metal-poor stars (Wheeler et al 1989). However the overabundance of another α-process element S relative to Fe, is not understood in the lines of nucleosynthesis. The production of S, which requires oxygen burning at central temperatures of around $1\text{-}2 \times 10^8$ K, is very hard to explain in low-mass post-AGB stars. The large overabundance of S is also found in extremely metal-poor post-AGB stars like HD 46703, BD +39^0 4926 etc.   The observed large abundances of volatile elements like C, N, O and S and large deficiency in refractory elements (iron peak elements) like Na, Mg, Si, Ca, Ti, Cr, Fe, Ni etc., are attributed
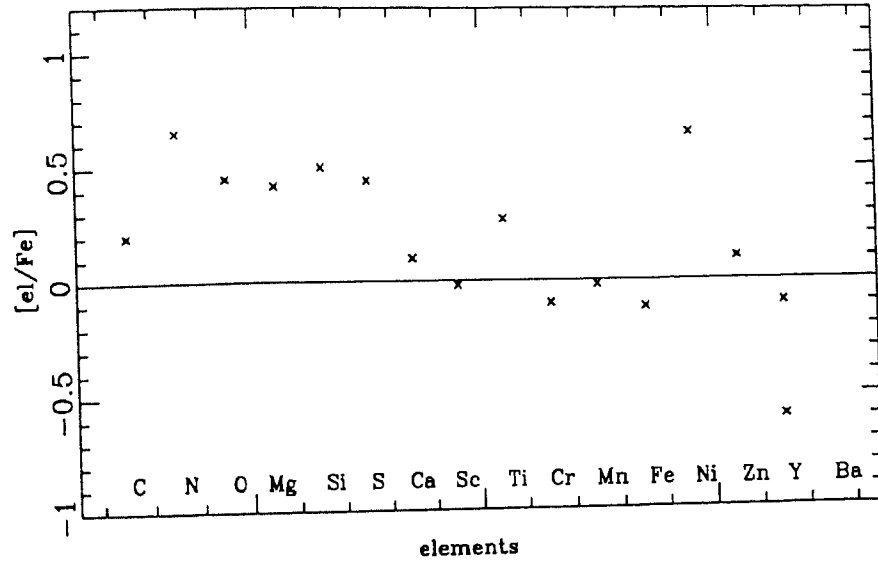
Figure 5.13: Chemical composition of IRAS 18095+2704

to depletion of iron peak elements into grains due to the condensation (Venn and Lambert 1990; Bond 1991; Lambert 1991; Parthasarathy et al 1992; Van Winckel et al 1992). The refractory elements in the form of dust grains have been blown away by radiation pressure and the gas with depleted metal has stayed back, as the radiation pressure transfers greater momentum to the dust grains (Mathis and Lamers 1992; Waters et al 1992). Similar abundance pattern is also seen in slightly metal-poor ([Fe/H]=−0.3) high latitude post-AGB star HD 161796 (Luck et al 1990). It is overabundant in C ([C/Fe]=0.3) O ([O/Fe]=0.4) and ([S/Fe]=0.4. However, in both extremely metal-poor post-AGB stars and HD 161796 s-process enrichment is not evident. Note that the abundance of Zn serves as a good diagnostic to ascertain whether the observed abundances are due to nucleosynthesis or due to depletion of Fe. The derived abundance of Zn ([Zn/Fe]=0.1) comes from a single line and hence relying on the abundance of Zn to interpret either way is difficult.

The solar abundance of S and the abundance of Ca ([Ca/Fe]=−0.2 (which is more depleted than other iron peak elements (Field 1974; Jenkins 1989) and the observed overabundances of C, Na, Si and s-process elements relative to Fe may be the result

of both depletion of Fe and also nucleosynthesis. Thus its high radial velocity (65 km s^{-1}), its galactic position and supergiant like spectrum suggest, it is a low-mass evolved supergiant. The chemical composition and its position in the H-R diagram, double peak energy distribution (chapter2) indicate this is a post-AGB supergiant.

Another important candidate in our sample is IRAS 18095+2704. Recently Klochkova (1995) has studied the chemical composition of this object. Evidence for the third dredge-up is seen in this object with CNO overabundances. However the large O/C=4 suggest that the star is oxygen-rich. Oxygen rich nature of this source also has been suggested by presence of SiO features in IRAS low resolution spectrum. Carbon bearing molecules like CO, HCN are not detected, but OH features are seen in the direction of this object. However we found the s-process elements Y and Ba are deficient. The s-process elemental deficiency is observed only in metal-poor stars with [Fe/H]<−2.0 (Sneden and Parthasarathy 1983) and is not expected in stars of metallicity of IRAS 18095+2704. This object also shows overabundance of S ([S/Fe]=0.6) and α process elements Mg and Si.

5.6   Conclusions

We have analyzed the high resolution optical spectra of three post-AGB candidates HD 179821, HD 70379 and IRAS 18095+2704. Our abundance analysis results of HD 179821 suggests that this is a low-mass evolved object but not a run away population I supergiant ejected from disc. The observed excess abundances in C and s-process elements are consistent with the nucleosynthesis predictions on the advanced phases of AGB evolution. The high radial velocity, low [Fe/H], far-IR excess and its position in the H-R diagram supports the idea that this star is most probably a post-AGB star caught in between AGB and PN. We also estimated the dust parameters of HD 179821 using the derived physical parameters of the star which are in general agreement with the post-AGB evolutionary models. We found mild metal-deficiency in HD 70379. It shows overabundances in C,O, α-process and s-process elements suggesting that it has evolved through the AGB phase. Thus HD 70379 with its high radial velocity (V$_r$=65 km s^{-1}), high latitude (10°) and its optical and IR studies suggest that it is

a low-mass post-AGB supergiant.

Elemental abundances of IRAS 18095+2704 suggest this also to be an evolved low-mass star. We find overabundance of carbon and nitrogen indicating that this star experienced both CNO and triple-α reactions and third dredge-up mixing. However we did not find overabundance of s-process elements.

Chapter 6

HD 105262: A high latitude metal-poor post-AGB A supergiant with large proper motion

6.1 Introduction

Recently Corbally and Gray (1993) surveyed the spectral characteristics of A-type stars in the galactic halo. It is possible that some of the halo A-type stars are misclassified as Field Horizontal Branch (FHB) stars. It may be likely that some of them may be post-AGB A supergiants. Recently, Abt (1993) classified the spectrum of the halo A star HD 105262 (galactic latitude $+76°$) as A0p Ib and found that its spectrum is similar to that of the metal-poor post-AGB A supergiant HR 4049. HD 105262 also shows a high c1-index (Eggen 1974) similar to the post-AGB A and F supergiants (Bidelman 1993). In fact Eggen (1974) suggested that HD 105262 may be similar to the metal-poor post-AGB A supergiant BD+39° 4926 (Kodaira 1973). However Glaspey (1982) argued that HD 105262 is a FHB A-type star.

In order to understand the evolutionary stage and chemical composition of HD 105262 we have carried out an analysis of its spectrum, and the results are presented in this chapter.

6.2 Observations

We have obtained optical spectra of HD 105262 on 13th (UT:22h30m) and 14th (UT: 22h30m) February, 1995 with the 2.3m (VBT) telescope at Kavalur equipped with a B & C- spectrograph and a CCD detector. Spectra cover the wavelength ranges: 4200 - 4600Å, 4900 - 5300Å, 6000 - 6400Å, 6300 - 6700Å, 6800 - 7200Å, 7200 - 7600Å and 7400 - 7800Å. The effective resolution obtained from the FWHM of comparison lines for all the frames is around 1.1Å and the spectra of all the frames has S/N≈100. Spectroscopic reductions were done using the standard IRAF package.

During writing of this thesis we obtained high resolution (0.15Å) optical spectra of this star in the region 5700Å-8700Å. This spectra has been observed with the 2.1 m telescope equipped with echelle spectrograph at McDonald observatory on 8th (UT) December 1995.

6.3 Analysis

6.3.1 The spectrum of HD 105262

The spectrum of HD 105262 in the Hγ region is shown in Fig. 6.1 together with the spectra of normal supergiants HD 87737 (A0 Ib), HD 202850 (B9 Iab) and also the spectrum of the FHB star HD 93329 (A0, [Fe/H]= −1.5). The strength and shapes of the hydrogen line profiles in the spectrum of HD 105262 are similar to that of B9 Iab or A0 Ib supergiants, for example, the Hγ profile in Fig. 6.1. They are not as broad as in FHB stars. The strengths of Mg II 4481Å and Fe lines are much weaker in the spectrum of HD 105262 compared to that of normal A-type supergiants, and they are weaker than those in the metal-poor ([Fe/H]= −1.5) A0 FHB star HD 93329. There is a weak He I line at 4471Å. We also identified He I line at 5875Å (Fig. 6.2) The Fe I lines are extremely weak or absent. The presence of He I lines in the spectrum of HD 105262 indicates that its spectral type may not be later than A0. We estimate the spectral type and luminosity class of HD 105262 to be A0 Ib, in good agreement with that found by Abt (1993).
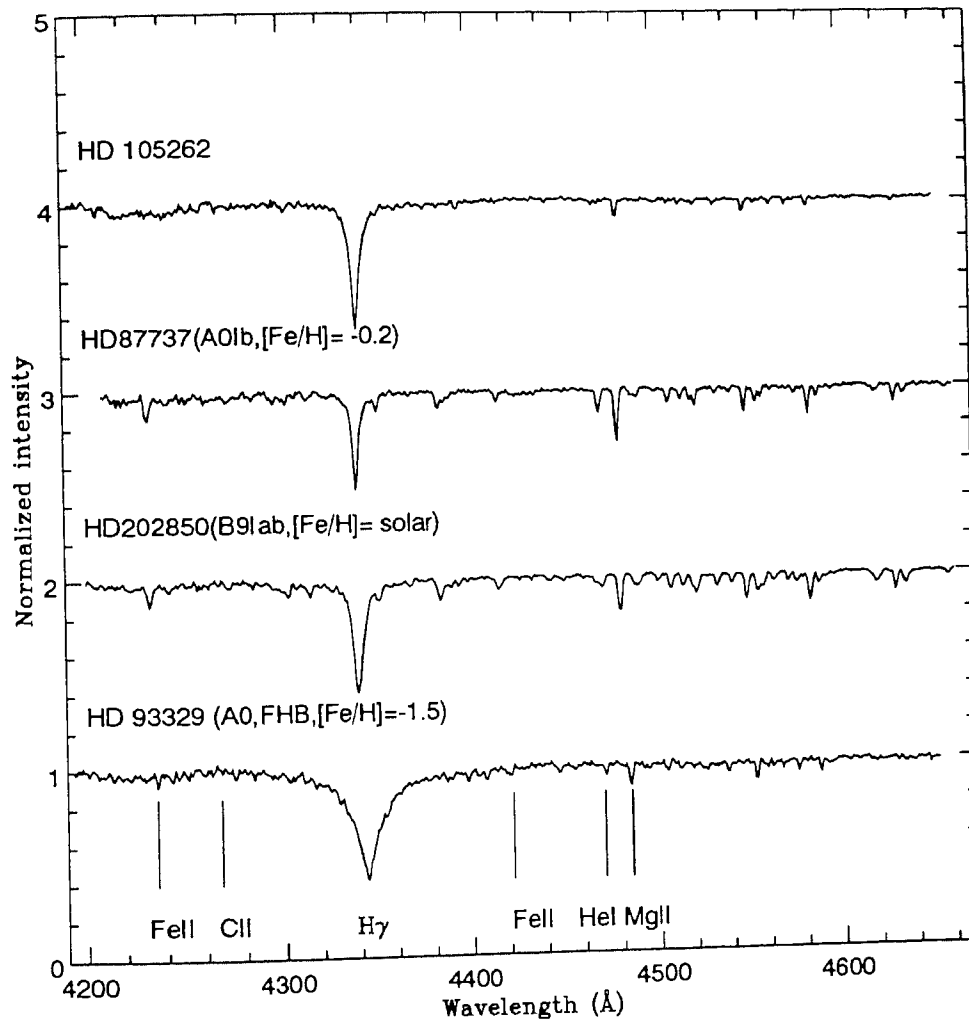
Figure 6.1: *Spectra of HD 105262, normal supergiants, HD 87737(A0 Ib), HD 202850(B9 Iab) and the FHB star HD 93329 (A0, [Fe/H]=−1.5). He I, 4471Å C II, 4367Å ,Hγ, 4340.4Å and metallic lines are identified.*
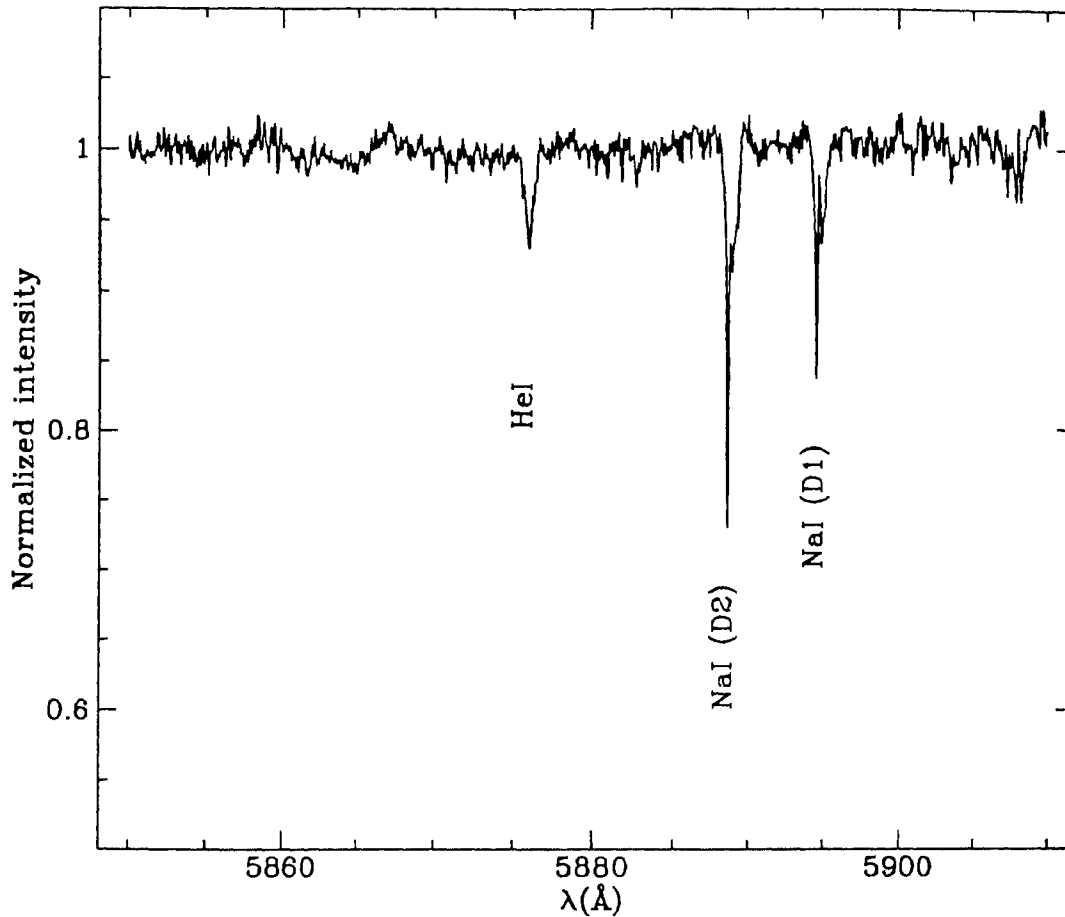
Figure 6.2: *Spectrum of HD 105262 around 5880Å showing the He I line at 5876Å. The ISM NaI(D1) and NaI(D2) lines are also indicated*

6.3.2 Atmospheric parameters

The physical parameters, surface temperature T_{eff}, surface gravity log g and micro-turbulent velocity ξ_t required to determine the elemental abundances, are estimated as follows.

The surface temperature and micro turbulent velocity can be estimated by demanding that there should be no dependence of the FeI abundances upon lower excitation potentials and equivalent widths of FeI lines, respectively. Surface gravity can also be determined spectroscopically by forcing FeI and Fe II to give the same
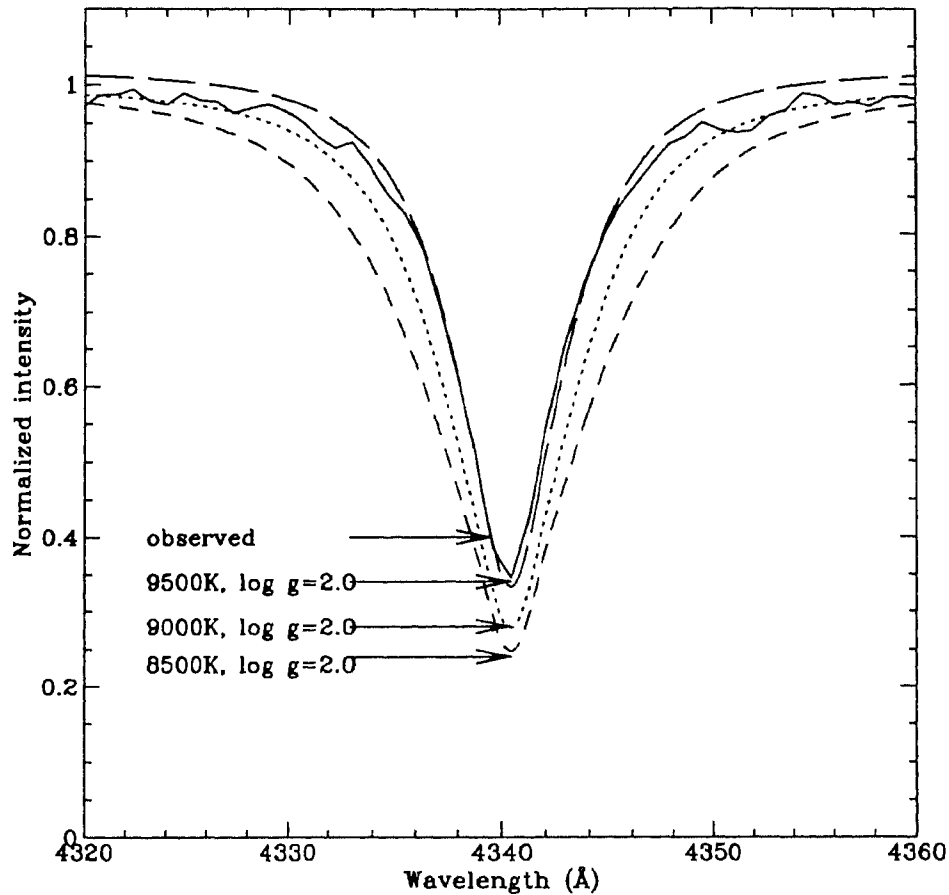
Figure 6.3: *The observed Hγ profile of HD 105262 (solid line) compared with the Kurucz (1979) synthetic Hγ profiles for different temperatures.*

abundance. It is, however, difficult to apply these methods, given that the neutral metallic lines are absent or very weak in the spectrum of HD 105262.

The surface temperature T_{eff} can be derived from the spectral type, UBV and Strömgren uvbyβ photometry. The UBV photometry V= 7.08, B-V= -0.01, U-B= -0.05 and Strömgren photometry b-y= 0.056, c1= 1.406, m1= 0.074 have been taken from Eggen (1977). The colour excess derived by Feltz (1972) for normal stars in the vicinity of HD 105262 are consistent with little or no interstellar reddening. The calibration of spectral-type$-T_{eff}$ relation for supergiants (Flower 1977) yields T_{eff}= 9500 K for A0 supergiants. The T_{eff}= 8500 K, and log g= 1.5 for HD 105262 have

been derived by Klochkova and Panchuk (1987) using the half widths and equivalent widths of the Balmer Hγ and Hδ lines in the T_{eff} versus log g diagram. By comparing UBV colours of HD 105262 with the theoretical UBV colours (Relyea and Kurucz 1978) for [M/H]= -2.0, we estimate T_{eff}= 9000 K and log g= 2.0. An upper limit for the model temperature can be found by considering the absence or presence of He I lines in the spectra. The strengths of He I lines at 4471Å (EW=40mÅ) and at 5875Å(EW=38mÅ) (Fig. 6.2), are expected for the T_{eff}=9000 K, and log g=2.0 model. We also estimated T_{eff} and log g, by comparing the Hγ profile, with the Kurucz (1979) LTE Balmer Hγ grids of [M/H]= -2.0 for different temperatures and surface gravities (Fig. 6.2). We obtained T_{eff}= 9500 K, and log g= 2.0 from matching both the wings and core of the Hγ profiles (Fig. 6.2).

Another parameter involved in deriving the chemical composition is the microturbulent velocity ξ_t. We adopted ξ_t= 4 km s^{-1}. This value is typical for low surface gravity metal-poor post-AGB supergiant stars such as HD 56126 (ξ_t= 4 km s^{-1} (Parthasarathy et al. 1992), HD 52961 (ξ_t= 5 km s^{-1}; Waelkens et al. 1991), BD+39° 4926 (5 km s^{-1}; Kodaira 1973). We adopt for our abundance analysis T_{eff}= 9000 K, log g= 2.0 and ξ_t= 4 km s^{-1}.

6.3.3 Absolute magnitude

The equivalent width of the O I triplet at 7771Å in the spectrum of A-type stars is sensitive to the luminosity (Sorvari 1974). Using the equivalent width of O I 7771Å triplet and M_v calibration of Sorvari (1974) we derive M_v= -4.0. Klochkova and Panchuk (1987) derived M_v= -4.8 from the equivalent width of Hγ profile. The M_v versus uvby and β photometry calibration for high proper motion, metal poor, A-type giant stars (Stetson 1991) yields M_v= -5.0.

The absolute magnitude (M_v) may also be calculated using a standard formula,

$$M_v = -2.5 log(M/M_\odot) + 2.5 logg - 10 logT_{eff} - B.C + 31.3 \qquad (6.1)$$

By using the adopted photospheric parameters of HD 105262, (T_{eff}=9000 K, log g=2.0) and the typical mass of 0.6M$_\odot$ of pop II stars, we find M_v=-2.5. The bolometric correction (B.C) of -0.2 has been applied. However this formula is very

sensitive to log g and T_{eff} (e.g T_{eff}=9500 K, log g=1.5 yield M_v=−4.0). Uncertainties in derived T_{eff} and log g values, introduce an uncertainty of about 1.5 mag in M_v.

6.3.4 Chemical composition

Abundances of the chemical elements were determined with the local thermodynamic equilibrium (LTE) model atmosphere grids computed by Kurucz (1979). For computing the synthetic spectra and equivalent widths, we used updated codes LINES and MOOG (Sneden 1973). We have used oscillator strengths (log gf) of O I-triplet at 6156Å and N I lines, listed by Waelkens et al. (1991). For O I-triplet at 7771Å, we used gf values of Takeda (1994). For other metallic lines, we have taken gf values from Fuhr et al (1988).

We have derived elemental abundances of HD 105262 using the model atmosphere: T_{eff}= 9000 K, log g= 2.0, [M/H]= −2.0 and microturbulent velocity ξ_t= 4 km^{-1}. Keeping in mind the uncertainties in the T_{eff} of this kind of stars, we also carried out abundance analysis using the models with T_{eff}= 8500 K, and T_{eff}= 9500 K for different microturbulent velocities. The uncertainties in the estimated atmospheric parameters, T_{eff} of ±500 K, log g of ±0.5 dex and ξ_t of ±2 km^{-1} introduce uncertainties in derived abundances approximately by ± 0.3 dex.

The carbon abundance is based on single C II line at 4267.27Å. Abundance of carbon has been derived both from the line analysis and synthetic spectra. The nitrogen abundance is derived from lines in the red region at 7442.63Å and 7468.28Å. The oxygen abundance is derived from the O I-triplet lines at 6156Å and at 7771Å. The oxygen abundance ([O/H]= 0.2) derived from 7771Å triplet lines is larger than the oxygen abundance ([O/H]= −0.5) obtained from 6156Å triplet lines. The over-abundance of oxygen from 7771Å triplet lines may be due to Non-LTE effects. We applied Non-LTE correction of 0.6 dex (Baschek et al. 1977) to our LTE abundance of oxygen, the abundance [O/H]= −0.4 after correction is comparable to the abundance derived from the O I lines at 6156Å. The CNO abundances are found to be [C/H]= −0.1, [N/H]= −0.3, [O/H]= −0.5. The abundances of α-process elements
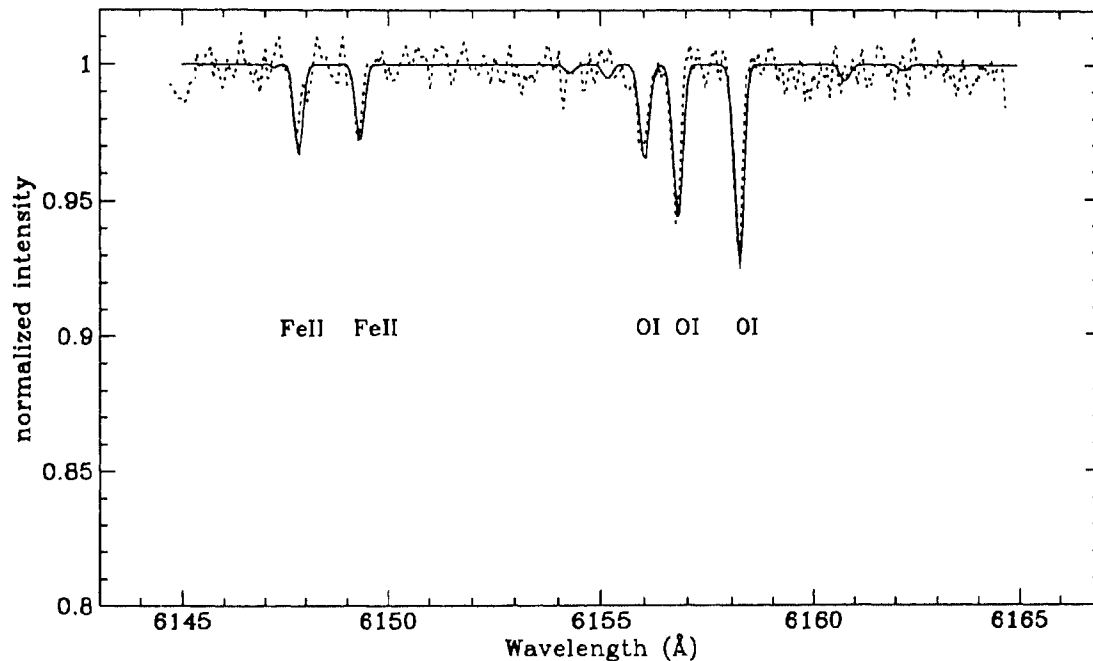
Figure 6.4: *Synthesis of O I lines at 6156Å for HD 105262. The observed (dotted lines) Fe II lines and O I lines are well matched with [Fe/H]=−2.4 and [O/H]=−0.9 for an adopted model (solid lines): T_{eff}=9000 K, log g=2.0 ξ_t=4 km s^{-1} and [M/H]=−2.0*

Mg, Si have been found to be [Mg/H]= −1.6, [Si/H]= −1.4. The abundance of silicon and magnesium are derived from the lines at 6347.09Å, 6371.35Å and 5183.60Å, 5172.69Å respectively. We estimated the He abundance ([He/H]=−0.2), using the He I line at 4471Å. Since the HeI line at 4471Å is weak and blended with metallic lines, the abundance of He is highly uncertain. To check our abundance analysis, we also carried out spectrum synthesis analysis of the FHB star HD 93329 using the spectra of the same resolution obtained with the same instrument. The derived metal abundances are in good agreement with the abundances obtained by Adelman and Philip (1994). The elemental abundances derived from high resolution echelle spectra are given in brackets in Table 6.1 and Table 6.2. These values are in good agreement with the values obtained from low resolution spectra. The CNO abundances of HD 105262 with respect to iron are found to be over abundant: [C/Fe]= +2.3, [N/Fe]=

Table 6.1: Elemental Abundances of HD 105262 for different temperatures. The values given in brackets are the abundances derived from high resolution spectra.

T_{eff} log g=2.0 ξ_t=4km s^{-1}	[C/H]	[N/H]	[O/H]	[Mg/H]	[Si/H]	[Ti/H]	[Fe/H]
8500	−0.3	−0.3	−0.6	−1.9	−1.8	−2.1	−2.3
9000	−0.1	−0.3 (−0.42)	−0.5 (−0.87)	−1.6	−1.4 (−1.35)	−2.0	−2.2 (−2.4)
9500	0.3	0.1	−0.4	−1.0	−1.0	−1.8	−2.1

+2.0, [O/Fe]= +1.5. The CNO, Mg, Si and metal abundances of HD 105262, HD 107369, HD 46703 and BD+39° 4926 are compared in Fig. 6.3. The abundance (Table. 6.1) pattern of HD 105262 is similar to that of the metal-poor high galactic latitude post-AGB supergiant BD+39° 4926 (Kodaira 1973).

6.3.5 Space motions

From our spectra the radial velocity of HD 105262 is found to be V_r= 42±1 km s^{-1}. This is in agreement with the radial velocity measurements made earlier: +42.0±3.7 km s^{-1} (Young 1942), +42.0±6.8 km s^{-1} (Albizkij 1947), +41.4 km s^{-1} (Wilson 1953) and +45.0 km s^{-1} (Glaspey 1982).

The proper motion of +0″.038 year^{-1} and -0″.042 year^{-1} in right ascension and declination respectively, are listed in the SAO catalogue. The total proper motion of HD 105262 is μ= 0″.056 year^{-1}. Taking the heliocentric radial velocity V_r= 41 km s^{-1}, proper motion μ= 0″.057 year^{-1} and M_v= −5 the space motion is found out to be V_s= 700 km s^{-1} with respect to the Sun. The high space velocity of HD

Table 6.2: Comparison of chemical composition of HD 105262 with various types of evolved stars.

[el/H]	HD105262	HD46703	BD+39° 4926	HD107369	PopI supergiants	BHB star M4 No. 4408
[C/H]	−0.1	−0.27	−0.4	≤−1.27	−0.25	−0.99
[N/H]	−0.3(−0.42)	+0.22	0.4	−0.68	+0.7	+0.1
[O/H]	−0.5(−0.87)	−0.46	−0.1	−1.10	−0.16	−0.9
[Mg II/H]	−1.6	−1.48	−1.5	-	−0.12	−0.35
[Si II/H]	−1.4(−1.35)	−1.94	−1.7	−0.95	−0.22	−0.57
[Ti II/H]	−2.0	−1.89	−3.7	−0.84	−0.07	−0.6
[Fe II/H]	−2.2(−2.4)	−1.56	−2.9	−1.16	0.11	−1.06

105262, is larger than the escape velocity from the Galaxy of 290 km s^{-1} near the Sun. The positions of HD 105262 in the equatorial galactic plane are X= −73pc, Y= −765pc, and Z= 2.5 kpc. The radial velocity V$_r$= 41 km s^{-1} and a distance 2.6 kpc of HD 105262 from the Sun yields space velocity components with respect to the galactic co-ordinate system: U= 445 km s^{-1}, V= −545 km s^{-1}, and W= −12 km s^{-1}. However by taking the M$_v$=−2.5 as derived from Eq. 1, we find a distance of only 850pc and its space motion 230km s^{-1}. In that case, it may be a nearby object and which is consistent with the high proper motion. Correspondingly its space velocity components become: U= 150 km s−1, V= −170 km s^{-1} and W= 28 km s^{-1}. The (U,V) components of HD 105262 suggest that the star is a member of the halo group of stars and it does not belong to the Wolf 630 group of stars (Eggen 1969).
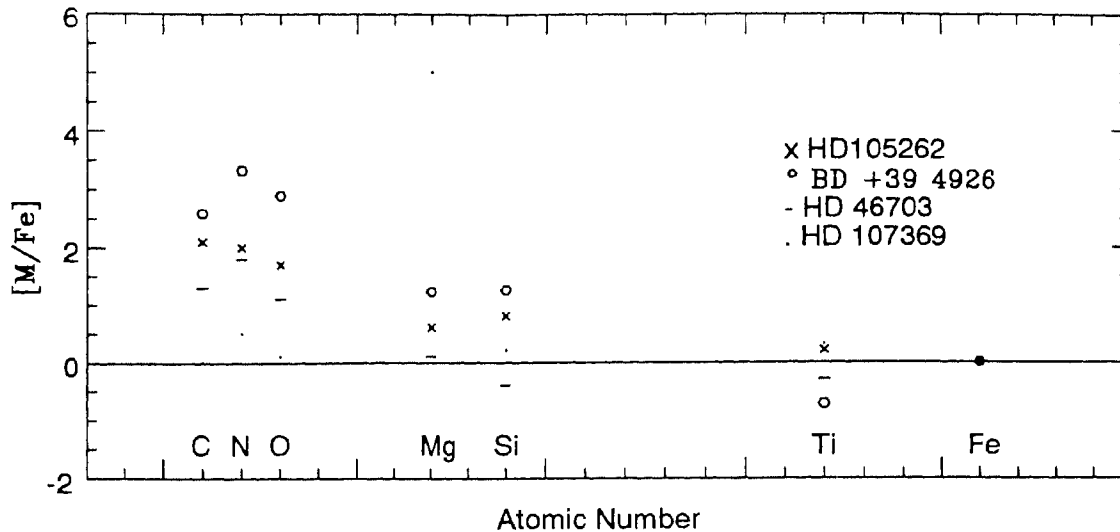
Figure 6.5: *Elemental abundances of HD 105262, metal-poor post-AGB supergiants HD 46703, BD+39° 4926 and an evolved pop II A star HD 107369.*

6.4 Discussion

The main results found from our analysis of HD 105262 are: (1) that it is a metal-poor evolved population II star, (2) the photospheric abundances of metals are very low [Fe/H]= −2.2, but the CNO and the α-process elements Mg and Si are overabundant with respect to iron. The chemical composition of HD 105262 clearly differs from the chemical composition of population I giants and halo dwarfs. Population I supergiants have elemental abundances: [Fe/H]= 0, [C/Fe]= −0.5, [N/Fe]= +0.5 and [O/Fe]= −0.3 (Luck 1993), whereas in metal-poor halo dwarfs : [C/Fe]= 0, [N/Fe]= −0.25, and [O/Fe]= 0.35 (Wheeler et al. 1989) and in metal-poor (Fe/H=−1.1) Blue Horizontal Branch (BHB) star No. 4408 in M4 (Lambert et al. 1992): [C/Fe]=+0.1, [N/Fe]=+1.1 and [O/Fe]=+0.2. However, the elemental abundances of HD 105262 using model atmosphere parameters, T_{eff}= 9000 K, log g= 2.0, ξ_t= 4.0 km s^{-1} and [M/H]= −2.0 are found to be [Fe/H]= −2.4, [C/Fe]= +2.3, [N/Fe]= +2.0, [O/Fe]= +1.5 and [α/Fe]= +0.7. Recently Van Winckel (1995) has studied a similar metal-poor (Fe/H=−1.1) star HD 107369. This star was first classified as a horizontal

branch (HB) star. HD 107369 is a high latitude A-type star having high Strömgrem cl-index similar to HD 105262. Bond and Philip (1973) suggested from its photometry that HD 107369 is   similar to the metal-poor high latitude object BD+39° 4926. Though HD 107369 shares some of its properties with HD 105262, it differs in chemical composition (Table. 6.2). The small C/O=0.2 and no enhancement of α-process elements, indicate that the star HD 107369 has not gone through the third dredge-up which occurs on the AGB. On the other hand, in HD 105262, the observed large C/O=1.2 and over abundance of Mg are the result of 3α-process via He-burning on the AGB, which are brought to the photosphere during the third dredge-up episode. However, [Mg/Fe]=+0.4 has been found as an upper limit, in metal-poor stars with [Fe/H]= -1.0 to -2.0 (Fuhrmann et al. 1995). The abundance ratio [Mg/Fe]=+0.6 in HD 105262 suggests that the star is metal-poor and slight excess in Mg abundance may be attributed to stellar evolutionary effects on the AGB. The star HD 107369 has neither Hα emission nor observed IR excess, which are similar to HD 105262. But the much pronounced excess in both CNO and α-process elements compared to HD 107369 clearly demonstrates that HD 105262 is relatively in an advanced stage of evolution. But as shown in Fig. 6.3, the chemical abundance pattern is strikingly similar to that of the metal-poor high latitude post-AGB stars, such as BD+39° 4926 (Waelkens et al. 1992) and HD 46703 (Bond and Luck 1987). The overabundance of C and the mild excess of α-process elements suggest that these elements have been brought up to the surface during the AGB phase.

Though HD 105262 shares its chemical composition and high luminosity similarities with high latitude post-AGB supergiants, it differs from other high latitude post-AGB stars, in its large proper motion, high space velocity and the absence of circumstellar dust. Most of the known high latitude post-AGB stars such as, HR 4049, HD 52961, HD 46703 and BD+39° 4926 are radial velocity variables. However, radial velocity measurements of HD 105262 over the last few decades do not show any evidence for variability indicating that it is not a binary star. Thus, HD 105262 may be a single star which has evolved with primordial metallicity in the halo. However, the peculiar chemical composition observed in high-latitude post-AGB stars has been attributed to selective depletion of iron peak elements. The presence of circumstel-

lar dust around these stars and the over abundance of sulphur with respect to iron strongly supports the idea that depleted refractory elements are locked up in the circumstellar dust grains. The question, whether the low metallicity [Fe/H]$=-2.2$ of HD 105262 is primordial and CNO and α-process abundances are stellar evolutionary effects, can be explained by two diagnostic elements zinc and sulphur. Our spectral resolution is not sufficient enough to resolve zinc lines and unfortunately we do not have spectra covering the SI lines to estimate its abundance.

Finally we discuss the kinematics of HD 105262. The large proper motion $0''.057$ year^{-1} and its distance 2.6 kpc from the Sun can be understood from its high space motion. Most of the halo objects were discovered from their large proper motion. As the star approaches the galactic plane, it attains high velocity because of gravitational potential of the Galaxy and therefore shows peculiar large proper motion. Thus, the large proper motion of HD 105262 is not because of proximity, may be due to high space motion in the orbit. Since the HD 105262 is an evolved low-mass (as seen in the discussion) star, with an extended atmosphere, it may be mimicking the supergiant spectrum (Parthasarathy 1994). Hence the derived M_v from balmer profiles, should be taken with caution. And may be we should not use the MK luminosity class and M_v calibration to estimate absolute luminosities and distance of these stars. Also, the M_v derived from equivalent width of the O I triplet vs luminosity class, may not represent the true luminosity of HD 105262. Instead if we take $M_v=-2.5$ (see section 3.3), we arrive at a distance of only 850pc and space velocity 230 km s$^-$. In that case, HD 105262 is a nearby evolved object with a luminosity of only 800L$_\odot$. The large proper motion and chemical composition indicate that it is a nearby low-mass star in an advanced stage of evolution.

6.5 Conclusion

From our spectrum synthesis analysis, we conclude that HD 105262 is not a FHB star. The low metallicity, over abundances of CNO and α-process elements and its locus in the HR diagram suggest that it is a low-mass population II star in the post-AGB stage of evolution. The large ratio of C/O$= 1.2$ shows that HD 105262 is a carbon-

rich star. The absolute luminosity and the distance of HD 105262 are uncertain. To disentangle this luminosity problem, it is highly important to remeasure the proper motion of this star.

Chapter 7

Conclusions

In this thesis we studied post-AGB stars in two parts: first, selection of post-AGB stars (Chapter 2) and second, chemical composition analysis (Chapter 4, Chapter5 and Chapter6) of few selected post-AGB candidate stars. We briefly summarize the important results obtained in this study.

In the first part, we selected a sample of 14 IRAS sources whose colours are similar to PNe and post-AGB stars. We identified the optical counterparts for these IRAS sources on the POSS and ESO sky survey plates. For all the identified stars, we obtained CCD imaging and BVRI photometry. For some of the bright stars in the sample, we also obtained low resolution optical and near-IR spectra. Using optical photometry and spectroscopy, we derived spectral types and luminosity classes for all the stars. We found all stars are in the A-F-G spectral types with luminosity class I or II. We estimated interstellar extinction using O and B stars in the direction of sample stars. We compared the observed spectral energy distribution from 0.4 μm to 100 μm with the theoretical energy distributions. We found the stars, IRAS 08187-1905, IRAS 05233-0626 and IRAS 17086 -2403 have only cold dust component, detached from the central stars. The rest of the sources present a double-peak energy distribution, one is due to hot dust component (near-IR) and the second one is due to cold dust component (far-IR). Using simple model, we derived stellar and dust envelope parameters. The results obtained in this study are in general agreement with post-AGB evolutionary models. The stellar parameters like gravity and T_{eff}

and dust envelope parameters like dust temperature, dust mass, dynamical life time of the dust envelope and high galactic latitude coupled with molecular observations of CO, OH, HCN, 3.3 μm and 21 μm features suggest that all the stars considered here are associated with post-AGB evolutionary phase.

The main part of this study is devoted to chemical composition analysis of selected post-AGB stars. One of the important results obtained in this thesis comes from the chemical composition analysis based on high resolution spectra of IRAS 05341+0852 (Chapter 4). We suggested in chapter 2 that this star is a good candidate for carbon-rich post-AGB star based on its optical, near-IR, far-IR and molecular observations. This is one of the few stars in which 21 μm emission has been detected. We found from the chemical composition analysis that the star is metal-poor ([Fe/H]=-1.0), carbon-rich (C/O$\geq$1) and large overabundance of s-process elements Y ([Y/Fe]=1.80), Ba ([Ba/Fe]=2.58), La ([La/Fe]=2.86), Ce ([Ce/Fe]=2.95),Pr ([Pr/Fe]=2.27), Nd ([Nd/Fe]=1.97 and Sm ([Sm/Fe]=0.86). With low metallicity, large C/O and overabundance of s-process elements, IRAS 05341+0852 is a third post-AGB star which shows clear cut evidence for nucleosynthesis and third dredge-up during helium shell flashes on the AGB phase. The other two post-AGB stars are HD 56126 and HD 187885 both are metal-poor, carbon-rich and overabundant in s-process elements. However, IRAS 05341+0852 is the first post-AGB star showing overabunance of Al, Li which are not enhances in HD 56126 and hD 187885. Overabundance of Li has been observed in HD 4671, but it is underabundant in C. The post-AGB nature of this object is debatable. Presence of large contents of Li and Al indicate that IRAS 05341+0852 has developed Hot Bottom Burning during its AGB evolution. The Hot Bottom Burning models predict production of Li only in the massive AGB stars. Low metallicity, radial velocity, large displacement from the galactic plane indicate that it is a low-mass star belonging to old thick disc or halo. The observed overabundance of Li and post-AGB nature of IRAS 05341+0852 suggest that Li can be produced in low-mass post-AGB stars also.

In Chapter 5 we studied the chemical composition of three post-AGB stars: HD 179821, HD 70379 and IRAS 18095+2704, based on high resolution spectra. The chemical analysis study of HD 179821 made it possible to understand the nature of

this coldest IRAS source. This star was thought to be a massive supergiant (Hawkins et al 1995; Kastner and Weintraub 1995) with large envelope mass of around 5-8 $M_\odot$. From the analysis of high resolution spectra, we found the star is metal-poor ([Fe/H]$\approx$1.0) and overabundant in C and s-process elements. The abundance of Zn found to be deficient similar to Fe. These results suggest that the observed metallicity of HD 179821 is intrinsic and the overabundances of C and s-process elements are the result of nucleosynthesis and deep mixing during the AGB phase. Its large radial velocity, low-metallicity and overabundances of C and heavy elements indicate that HD 179821 is a low-mass post-AGB star in transition between AGB and PNe and not a massive yellow supergiant. We also estimated distance, dust mass and dynamical age of dust envelope which are consistent with the post-AGB model calculations. HD 70379 is another bright IRAS source which has been suggested as a good candidate for low-mass post-AGB supergiant (Chapter 2). The chemical composition analysis results show that it is slightly metal-poor ([Fe/H]=-0.3) and overabundant in C,N ,and s-process elements. It is also found to be overabundant in sulphur similar to C. Overabundance of S as a result of nucleosynthesis in low-mass stars is difficult to understand. Thus the normal abundance (solar) of S indicates that the observed low metallicity is not intrinsic but it is due to depletion of iron-peak elements. Taking S abundance as the metallicity indicator, we discussed the chemical composition of HD 70379. We found slight overabundance of C and s-process elements which indicate that the star has undergone AGB nucleosynthesis and third dredge-up mixing. We conclude from its optical, IR properties, galactic position (Chapter 2) and chemical composition that HD 70379 is a new post-AGB star. In our study of chemical composition, we found IRAS 18095+2704 as an oxygen-rich post-AGB star. Evidence for third dredge-up is seen with CNO overabundances. The photospheric oxygen nature of this candidate confirms the chemical classification of oxygen-type based on dust envelope properties. However, we found deficiency in s-process elements Y and Ba.

We studied in detail, the medium and high resolution optical spectra of HD 105262 in Chapter 6. This is a high C1-index (C1=1.4), high galactic latitude (+72°) and high proper motion (0.057$''$) star. This star was previously thought to be a FHB star

with absolute magnitude M_v=0.8. Comparison of spectral features of HD 105262 with that of FHB star and supergiant of same spectral types show that it is an A-type supergiant with an extended atmosphere. The atmospheric parameters: T_{eff}=9000 K and log g=2.0 have been determined from the fittings of observed Balmer profiles with that of calculated profiles, from Strömgren photometry and from UBVR photometry. Using LTE model atmospheres we derived elemental abundances. We found the star is extremely metal-poor ([Fe/H]=-2.4). The abundances of CNO and α-process elements Mg, Si are found to be overabundant relative to Fe. We also discussed in detail the kinematics of HD 105262. From the derived radial velocity and absolute magnitude (M_v=−4 to −5), we found its space motion of around 700 km s^{-1} which is much larger than the escape velocity from the Galaxy of 290 km s^{-1} near the Sun. From the galactic positional components (X,Y,Z) and space velocity components (U,V, W) we conclude that HD 105262 is a member of halo group of stars. We argued in detail the results of both chemical composition analysis and kinematics and concluded that it is most probably a low-mass post-AGB star.

Line Identification

Appendix:

In this appendix we tabulated the identified lines in the spectra of post-AGB stars HD 70379, IRAS 18095, HD 179821 and IRAS 05341+0852. Each table contains laboratory wavelength (λ_{lab}), element identification (Iden), low excitation potential (LEP), measured equivalent width (EW) in mÅ log gf values and derived abundance (log N).

Table A1: Line data of HD 70379

λ_{lab} Å	Iden	LEP	Ew mÅ	log gf	log N
5380.322	C I	8.64	165	-1.665	8.63
6006.06	C I	8.64	37		
6010.65	C I	8.64	26		
6014.842	C I	8.64	49		
6587.622	C I	8.53	124	-1.049	8.77
6663.01	C I	8.85	68		
6671.82	C I	8.85	30		
6828.193	C I	8.53	89	-1.386	
7100.130	C I	8.64	47	-1.473	
7108.92	C I	8.64		-1.595	
7111.450	C I	8.64	73	-1.07	8.44
7113.171	C I	8.64	115	-0.76	8.44
7115.17	C I	8.64	129	-0.899	8.53
7116.963	C I	8.64	156	-1.08	8.92
7119.704	C I	8.64	97	-1.31	8.62
6156.80	O I	10.740		-0.44	8.49
6158.171	O I	10.741	43	-0.29	
5682.647	NaI	2.1	108	-0.710	6.39
5889.973	NaI	0.0		0.1099	
5895.8940	NaI	0.0		-0.190	
6160.753	NaI	2.1	43	-1.270	6.34
6154.230	NaI	2.1	21	-1.570	6.31
5645.618	Si I	4.93	37	-2.14	7.72
5772.149	Si I	5.080	47	-1.750	7.59
5780.388	Si I	4.920	28	-2.35	7.81
5793.079	Si I	4.93	84	-2.06	
5797.865	Si I	4.95	69	-2.05	
5948.548	Si I	5.08	117	-1.230	7.72
6091.920	Si I	5.87	20	-1.404	7.52
6125.026	Si I	5.61	27	-1.513	7.55
6155.142	Si I	5.62	72	-0.965	7.55
6721.844	Si I	5.56		-1.264	
6848.566	Si I	5.860		-2.090	
6347.095	Si II	8.12	267	0.219	7.84
6371.355	Si II	8.12	195	-0.104	7.53
5172.698	Mg I	2.710	433	-0.3810	
5183.619	Mg I	2.720	447	-0.158	
5711.095	Mg I	4.340	90	-1.683	

Table A1: continued

λ_{lab} Å	Iden	LEP	Ew mÅ	log gf	log N
6318.708	Mg I	5.108	136	-1.970	
5278.961	S I	6.860	63	-2.020	7.59
6041.93	S I	48	7.870	-1.00	7.42
6046.015	S I	75	7.870	-0.779	7.48
6052.682	S I	7.870	66	-0.6300	7.25
6743.575	S I	7.870	34	-0.7001	7.0
6748.779	S I	7.870	70	-0.440	7.14
6757.195	S I	7.870	89	-0.2900	7.15
5581.979	Ca I	2.52	71	-0.555	5.84
5590.126	Ca I	2.52		-0.5711	5.92
5601.286	Ca I	2.52	78	-0.5230	5.86
5857.459	Ca I	2.92	152	0.24	6.12
6102.727	Ca I	1.88	154	-0.606	6.03
6107.26	Ca I				
6122.260	Ca I	1.886	213	-0.316	6.29
6162.180	Ca I	1.90	226	0.09	6.03
6166.440	Ca I	2.52	28	-1.33	6.12
6169.044	Ca I	2.52	42	-0.778	5.76
6169.564	Ca I	2.52	68	-0.590	5.86
6449.820	Ca I	2.52		-0.502	5.76
7148.150	Ca I	2.71	166	-0.137	6.31
5129.162	Ti II	1.892	282	-1.39	
5154.075	Ti II	1.566	457	-1.920	
5185.908	Ti II	1.893	217	-1.350	4.37
5303.223	V II	2.276	170	-1.930	3.34
5332.665	V II		127		
5819.930	V II	2.522	34	-1.700	3.64
5296.702	Cr I	0.98	73	-1.40	5.34
5348.326	Cr I	1.00	79	-1.290	5.30
5781.759	Cr I	3.32	56		
5783.866	Cr I	3.32	10	-0.295	5.27
5787.926	Cr I	3.32	20	-0.083	5.38
5305.866	Cr II	3.83	136	-2.08	5.32
5308.429	Cr II	4.07	129	-1.81	5.21
5310.697	Cr II	4.07	81	-2.28	5.30
5313.585	Cr II	4.07	162	-1.65	5.32
5420.929	Cr II	3.76	113	-2.360	5.37
6053.475	Cr II	4.74		-2.16	

Table A1 continued

λ_{lab} Å	Iden	LEP	Ew mÅ	log gf	Log N
5239.823	Sc II	1.455	153	-0.7701	2.47
5318.361	Sc II	1.357	59	-2.040	2.55
5667.153	Sc II	1.500	110	-1.200	2.63
6245.620	Sc II	1.510	107	-0.930	2.34
6604.600	Sc II	1.357	66	-1.480	2.43
5067.155	Fe I	4.22	55	-0.9700	7.32
5068.771	Fe I	2.94	153	-1.230	7.30
5090.782	Fe I	4.26	84	-0.4000	7.04
5141.746	Fe I	2.42	80	-2.150	7.20
5162.281	Fe I	4.18	165	0.0200	7.25
5198.718	Fe I	2.22	111	-2.135	7.23
5216.283	Fe I	1.61	185	-2.150	7.31
5302.307	Fe I	3.28	167	-0.8800	7.38
5364.880	Fe I	4.44	160	0.2210	7.24
5373.714	Fe I	4.47	40	-0.8600	7.25
5389.486	Fe I	4.41	77	-0.4110	7.15
5393.176	Fe I	3.24	140	-0.9100	7.15
5398.287	Fe I	4.44	50	-0.6700	7.16
5410.918	Fe I	4.47	170	0.2800	7.30
5445.053	Fe I	4.39	140	-0.0200	7.26
5487.755	Fe I	4.14	90	-0.7100	7.31
5569.631	Fe I	3.42	170	-.54000	7.19
5576.099	Fe I	3.43	132	-1.100	7.33
5633.953	Fe I	4.99	45	-0.270	7.17
5706.008	Fe I	4.61	68	-0.5300	7.36
5753.132	Fe I	4.26	60	-0.7600	7.22
5763.002	Fe I	4.21	90	-0.4500	7.13
5905.680	Fe I	4.65	30	-0.7300	7.14
5916.257	Fe I	2.45	21	-2.99	7.34
5930.191	Fe I	4.65	72	-0.2300	7.14
6003.022	Fe I	3.88	62	-1.120	7.27
6027.056	Fe I	4.07	53	-1.210	7.43
6056.013	Fe I	4.73	55	-0.4600	7.27
6065.494	Fe I	2.61	128	-1.530	7.11
6136.624	Fe I	2.45	200	-1.400	7.46
6137.702	Fe I	2.59	174	-1.40	7.37
6165.363	Fe I	4.14	11	-1.55	7.08
6191.570	Fe I	2.43	145	-1.600	7.17

Table A1 continued

λ_{lab} Å	Iden	LEP	Ew mÅ	log gf	log N
6200.321	Fe I	2.61	45	-2.437	7.29
6213.437	Fe I	2.22	61	-2.660	7.34
6215.149	Fe I	4.19	40	-1.440	7.59
6219.287	Fe I	2.20	97	-2.433	7.41
6246.327	Fe I	3.60	109	-0.9600	7.27
6252.565	Fe I	2.40	122	-1.687	7.03
6265.141	Fe I	2.18	61	-2.55	7.20
6335.337	Fe I	2.20	91	-2.23	7.15
6336.830	Fe I	3.69	77	-1.05	7.18
6355.035	Fe I	2.84	33	-2.420	7.31
6265.141	Fe I	2.18	61	-2.55	7.20
6358.687	Fe I	.86	17	-4.468	7.30
6393.612	Fe I	2.43	140	-1.62	7.15
6400.010	Fe I	3.60	138	-0.52	7.07
6411.658	Fe I	3.65	122	-0.82	7.28
6419.956	Fe I	4.73	66	-0.240	7.17
6421.360	Fe I	2.28	127	-2.027	7.30
6430.856	Fe I	2.18	114	-2.006	7.08
6575.037	Fe I	2.59	31	-2.820	7.46
6593.887	Fe I	2.43	49	-2.422	7.16
6609.118	Fe I	2.56	20	-2.692	7.11
6677.997	Fe I	2.69	109	-1.470	6.96
6750.164	Fe I	2.42	43	-2.62	7.28
6945.210	Fe I	2.42	51	-2.48	7.23
5132.674	Fe II	2.84	183	-4.18	7.64
5234.630	Fe II	3.22	339	-2.05	7.42
5264.808	Fe II	3.33	243	-3.19	7.62
5272.400	Fe II	5.95	55	-2.03	7.12
5425.259	Fe II	3.20	214	-3.36	7.46
5813.670	Fe II	5.57	24	-2.75	7.12
5991.378	Fe II	3.15	159	-3.74	7.32
6084.105	Fe II	3.20	112	-3.98	7.23
6113.329	Fe II	3.22	82	-4.31	7.18
6239.948	Fe II	3.89	105	-3.68	7.47
6247.562	Fe II	3.89	227	-2.51	7.36
6383.715	Fe II	5.55	56	-2.27	7.08
6416.928	Fe II	3.89	167	-2.85	7.16
6432.683	Fe II	2.89	158	-3.74	7.07

Table A1 continued

λ_{lab} Å	Iden	LEP	Ew mÅ	log gf	log N
6446.400	Fe II	6.22	24	-2.16	7.10
5035.370	Ni I	3.635	142	0.29	5.93
5080.535	Ni I	3.655	155	0.130	6.21
5155.771	Ni I	3.898	76	-0.090	5.99
5754.666	Ni I	1.935	54	-2.330	6.36
5760.841	Ni I	4.105	18	-0.799	6.12
5805.226	Ni I	4.167	26	-0.639	6.20
6086.288	Ni I	4.266	14	-0.530	5.88
6176.816	Ni I	4.088	40	-0.530	6.23
6339.118	Ni I	4.154	28	-0.539	6.13
6643.638	Ni I	1.675	48	-2.229	5.98
6767.784	Ni I	1.826	60	-2.169	6.11
7122.206	Ni I	3.542	106	0.039	5.82
6362.350	Zn I	5.790	38	0.272	4.58
5087.426	Y II	1.084	265	-0.17	2.31
5119.120	Y II	0.992	109	-1.36	2.18
5123.222	Y II	0.992	258	-0.824	2.81
5200.415	Y II	0.99	236	-0.569	2.34
5205.730	Y II	1.033	502	-0.342	4.38
5402.783	Y II	1.839	154	-0.630	2.53
5546.032	Y II	1.748	-1.097	2.48	
5728.877	Y II	1.839	83	-1.125	2.50
5200.415	Y II	0.992	236	-0.569	
6613.73	Y II	1.740	90	-1.09	
6832.474	Y II	1.740		-1.82	
6795.428	Y II				
5853.688	Ba II	0.604	279	-1.0	2.16
6141.727	Ba II	0.704	405	-0.08	2.32
5092.803	NdII	0.380	36	-0.630	
5130.588	NdII	1.304	59	0.459	
5293.169	NdII	0.823	30	-0.06	
5319.820	NdII	0.550	36	-0.209	
6437.698	EuII	1.320		-0.276	0.16
6645.127	EuII	1.380	65	0.204	0.15

Table A2: line data of IRAS 18096+2704

λ_{lab} Å	Iden	LEP	Ew mÅ	log gf	Log N
4769.997	C I	7.48	37.0	-2.103	7.90
4775.877	C I	7.49	61.2	-2.093	8.30
6587.622	C I	8.85	61	-1.049	8.05
7087.820	C I	8.64	26	-1.480	8.14
7100.130	C I	8.64	31.4	-1.473	8.19
7111.480	C I	8.64	34.4	-1.07	7.80
7113.180	C I	8.64	77.0	-0.760	8.02
7115.190	C I	8.64	69.8	-0.899	8.10
7116.990	C I	8.64	78.5	-1.08	8.24
7119.660	C I	8.64	58.9	-1.31	8.30
7442.230	N I	10.33	35.3	-0.31	7.87
6156.800	O I	10.740	54.60	-0.44	8.82
4481.140	Mg II	886			
4703.003	Mg I	4.34	234.0	-0.60	7.29
5172.690	Mg I	2.71		-0.48	7.10
5183.619	Mg I	2.72		-0.238	7.10
6347.090	Si II	8.12	0.260		
6371.350	Si II	8.12	-0.050		
7405.790	Si I	5.61	79.1	-0.71	7.40
7409.100	Si I	5.61	74.6	-1.10	7.50
7415.950	Si I	5.61	107.0	-0.41	7.40
7423.510	Si I	5.62	84.5		7.40
4694.117	S I	6.52	52.3	-1.673	7.00
4696.262	S I	6.52	46.0	-1.56	6.90
4425.44	Ca I	1.88	83.0	-0.36	5.30
7148.150	Ca I	2.71	113.0	0.161	5.78
6122.226	Ca I	1.886	133.7	-0.316	5.77
6162.180	Ca I	1.90	160.8	-0.090	6.20
4374.470	Sc II	0.62			
4670.413	Sc II	1.36		-1.284	2.33
5031.020	Sc II	1.36		-0.38	2.20
4417.720	Ti II	1.16		-1.43	4.22
4470.860	Ti II	1.16			4.22
4646.170	Cr I	1.03	60.0	-0.79	4.79
5345.810	Cr I	1.00	65.0		4.98
5409.800	Cr I	1.03	82.0		4.80
4588.20	Cr II	4.07	240.0	-0.734	5.22
4616.630	Cr II	4.07	124.0	-1.283	4.77

Table A2 continued

λ_{lab} Å	Iden	LEP	Ew mÅ	log gf	Log N
4427.330	Fe I	0.05	197	-3.100	6.94
4447.730	Fe I	2.22	160	-1.321	6.9
4678.850	Fe I	3.60	66	-0.720	6.92
4736.780	Fe I	3.21	126	-0.540	7.00
5001.87	Fe I	3.88	126	-0.0499	7.10
5049.830	Fe I	2.28	138	-1.410	7.00
5068.770	Fe I	4.22	105	-1.070	7.10
5072.080	Fe I	4.28	131	-0.720	
5074.740	Fe I	4.22	90	-0.0499	7.10
5090.780	Fe I	4.26	54	-0.500	6.90
5142.530	Fe I	4.26	125	-0.700	
5162.280	Fe I	4.18	109	0.089	7.00
5339.940	Fe I	3.26	32	-0.5699	6.10
5364.880	Fe I	4.44	93	0.200	6.90
5367.480	Fe I	4.41	95	0.260	6.90
5369.970	Fe I	4.37	104	0.390	6.92
5373.714	Fe I	4.47	20	-0.880	6.80
5383.380	Fe I	4.31	132	0.480	6.90
5405.780	Fe I	0.99	178	-1.98	7.06
5415.210	Fe I	4.39	128	0.510	6.90
5432.960	Fe I	4.44	112	-0.79	
5434.530	Fe I	1.01	161	-2.22	7.00
6191.570	Fe I	2.43	71	-1.48	6.80
6322.690	Fe I	2.59	44	-2.40	
6393.612	Fe I	2.43	72	-1.57	6.83
6400.010	Fe I	3.60	96	-0.07	6.80
7411.160	Fe I	4.28	56	-0.33	
7511.030	Fe II	3.90	104	0.32	6.8
7445.760	Fe II	4.26	87	-0.02	6.86
4620.52	Fe II	2.83	199	-3.52	7.00
4893.82	Fe II	2.83	63	-4.46	6.80
5414.07	Fe II	3.22	97	-3.78	6.95
5425.26	Fe II	3.20	125	-3.49	7.00
6369.46	Fe II	2.89	55	-4.31	6.90
6383.71	Fe II	5.55	32	-2.26	6.77
6516.080	Fe II	2.89	142	-3.55	6.88
4604.990	Ni I	3.48	37	-0.35	5.67
4714.420	Ni I	3.38	90	0.23	5.68

Table A2 continued

λ_{lab} Å	Iden	LEP	Ew mÅ	log gf	Log N
5035.370	Ni I	3.635	94	0.23	5.55
7122.206	Ni I	3.542	46.5	-0.05	5.56
4722.160	Zn I	4.03	60.0	-0.35	4.06
4810.540	Zn I	4.08	61.0	-0.176	4.00
4883.690	Y II	1.08	103.30	0.07	1.00
4900.120	Y II	1.03	113.00	-.09	1.22
5087.430	Y II	1.08	65.7	-.17	0.90
5119.120	Y II	0.99	14.5	-1.36	0.90
4524.940	Ba II	2.51	103.2		0.9
4554.040	Ba II	0.00	357.4		1.5
6141.730	Ba II	0.70	222.2		1.0

Table A3: line data of HD179821

λ_{lab} Å	Iden	LEP	Ew mÅ	log gf
6587.622	C I	8.53		-1.049
4769.997	C I	7.48		
5052.151	C I	7.68		i-1.240
4703.003	Mg I	4.34		-0.44
6414.987	Si I	5.87		-1.20
6439.08	Ca I	2.52		0.15
6462.570	Ca I	2.52		
6462.749	Fe I	2.45		
6471.67	Ca I	2.52	74	-0.88
6493.788	Ca I	2.52		-0.40
4820.414	Ti I	1.50		-0.44
5024.85	Ti I	0.82	115	-0.422
5064.658	Ti I	0.05		
4851.496	V I	0.00		-1.139
4652.167	Cr I	1.00	138	-1.70
4789.342	Cr I	2.54		-0.566
4739.113	Mn I	2.93	88	-0.66
4783.424	Mn I	2.30		0.042
4260.486	Fe I	2.40		-0.02
4678.854	Fe I	3.60	257	-0.66
4733.597	Fe I	1.48		-3.71
4736.783	Fe I	3.21		-0.84
4789.658	Fe I	3.55		-1.31
4871.325	Fe I	2.86		-0.41
4875.88	Fe I	3.33		-2.01

Table A3 continued

λ_{lab} Å	Iden	LEP	Ew mÅ	log gf
4896.44	Fe I	3.88		-2.06
4905.138	Fe I	3.93		-2.00
5001.870	Fe I	3.88		-0.05
5006.00	Fe I	2.83		-0.72
5028.133	Fe I	3.57		-1.10
5041.08	Fe I	0.96		-2.89
5044.218	Fe I	2.85	52	-2.55
5048.439	Fe I	3.96		-1.26
5067.16	Fe I	4.22		-0.92
5068.77	Fe I	2.94		-1.07
5074.75	Fe I	4.22		-0.05
5083.345	Fe I	0.96		-3.00
5090.782	Fe I	4.26		-0.46
5097.05	Fe I	4.28		-0.43
6340.75	Fe I			
6419.96	Fe I	4.73		-0.27
6421.36	Fe I	2.28		-2.01
6469.192	Fe I	4.83	50	-0.68
4260.486	Fe I	2.40		0.18
4893.817	Fe II	2.83		-4.46
4923.930	Fe II	2.89		-1.43
4686.222	Ni I	3.60	80	-0.64
4829.03	Ni I	3.54	76	-0.33
4831.182	Ni I	3.61		-0.42
4904.43	Ni I	3.54	124	-0.218
5003.747	Ni I	1.68		
5080.539	Ni I	3.65		0.13
4722.163	Zn I	4.03	100	-0.75
4810.537	Zn I	4.08	236	-0.176
4900.124	Y II	1.03		
5087.430	Y II	1.08		-0.87
5112.279	Zr II	1.66	98	-1.38
6496.908	Ba II	0.6	550	-1.0
6526.95	La II	0.23		-1.84

Table A4: Line identification in IRAS 05341+0852

λ_{lab}	Element	LEP	EW(mÅ)	log gfs
6707.98	Li I	0.00	50	-0.430
6587.622	C I	8.540	106	-1.049
6655.531	C I	8.537	44	-1.941
7076.52	C I		225	
7100.130	C I	8.643	50	-1.436
7108.92	C I	7.946	77	-1.595
7111.450	C I	8.640	77	-1.070
7113.171	C I	8.650	171	-0.759
7115.17	C I	8.640	155	-0.899
7116.963	C I	8.650	174	-1.079
7119.704	C I	8.650	128	-1.309
6698.669	Al I	3.14	49	-1.619
6243.823	Si I		124	
6254.200	Si I			
	Fe I			
6347.095	Si II	8.12	310	0.260
6371.355	Si II	8.12	219	-0.049
6757.195	S I	7.87	66	-0.240
6462.500	Ca I			
	Fe I			
6493.788	Ca I	2.520	74	-0.109
6717.68	Ca I	2.71	88	-0.524
7148.150	Ca I	2.71	136	0.137
6245.630	Sc II		97	
6309.886	Sc II		91	
6604.600	Sc II		144	
6271.830	Cr II		167	
	Ce II			
6258.713	Ti I		232	
	Nd II			
6230.735	Fe I			
	V I			
6232.648	Fe I			
6252.565	Fe I	2.404	61	-1.686
6318.027	Fe I		111	
6335.337	Fe I	2.197	28	-2.230
6336.830	Fe I	3.686	36	-1.049
6393.610	Fe I	2.433	87	-1.619

Table A4 continued

λ_{lab}	Element	LEP	EW(mÅ)	log gf
6386.75	Fe I		62	
6400.000	Fe I	3.602	117	-0.519
6411.660	Fe I	3.654	75	-0.819
6421.350	Fe I	2.278	54	-2.027
6494.994	Fe I	2.404	126	-1.273
6574.252	Fe I	0.990	48	-5.040
6592.926	Fe I	2.727	39	-1.599
6677.997	Fe I	2.692	75	-2.470
7093.09	Fe I	4.558		-2.019
7411.162	Fe I	4.28	52	-0.33
7445.758	Fe I	4.26	69	-0.02
7495.077	Fe I	4.18	102	0.18
7511.031	Fe I	4.18	169	0.32
6238.390	Fe II		156	
6248.562	Fe II		131	
6369.463	Fe II	2.891	55	-4.360
6375.960	Fe II		56	
6383.715	Fe II	5.553	43	-2.270
6456.391	Fe II	3.903	314	-2.299
6516.05	Fe II	2.891	141	-3.450
7224.464	Fe II			
6643.638	Ni I	1.676	25	-2.299
7122.206	Ni I	3.542	58	0.039
6435.02	Y I	0.07	120	-0.823
6613.730	Y II	1.740	300	-1.097
6795.41	Y II		94	
6832.49	Y II	1.740	84	-1.939
6858.24	Y II		117	
6496.908	Ba II	0.604	560	-0.368
6262.250	La II		427	
6296.090	La II		223	
6305.460	La II		198	
6320.429	La II		355	
6390.493	La II		400	
6399.040	La II		115	
6526.99	La II		385	
6642.79	La II		66	
6671.40	La II		180	

Table A4 continued

λ_{lab}	Element	LEP	EW(mÅ)	log gf	
6774.33	La II		326		
6834.05	La II		104		
7066.23	La II		530		
6343.960	Ce II		180		
6507.16	Ce II		34		
6468.97	Ce II		75		
6652.72	Ce II		96		
6675.54	Ce II		84		
6755.08	Ce II		75		
6829.38	Ce II		88		
6397.960	Pr II	1.04	81	-0.819	
6413.680	Pr II		56		
6656.83	Pr II		63		
6673.78	Pr II		134		
6292.840	Nd II		68		
6330.290	Nd II		89		
6341.530	Nd II		105		
6390.00	Nd II		263		
6425.790	Nd II		119		
6428.65	Nd II		136		
6465.24	Nd II		90		
6504.46	Nd II		45		
6519.86	Nd II		66		
6550.19	Nd II		250		
6580.95	Nd II		124		
6637.19	Nd II		108		
6637.96	Nd II		166		
6650.57	Nd II		105		
6737.79	Nd II		99		
6740.11	Nd II		136		
6842.66	Nd II		44		
6385.20	Nd II		187		
6846.72	Nd II		198		
7037.30	Nd II		107		
7054.74	Nd II		64		
7142.04	Nd II		53		
6256.660	Sm II	1.160	62	-1.63	KP
6291.82	Sm II	1.400	88	-1.32	KP

Table A4 continued

λ_{lab}	Element	LEP	EW(mÅ)	log gf	
6327.475	Sm II	1.250	242	-1.32	KP
6431.00	Sm II	1.400	84	-2.04	KP
6502.00	Sm II	1.55	45	-1.97	KP
6549.77	Sm II	1.05	161	-2.14	KP
6382.07	Nd II		157		
6569.224	Sm II		142		
6570.675	Sm II	0.99	60	-1.91	KP
6589.725	Sm II	1.26	67	-1.41	KP
6856.03	Sm II	1.07	110	-1.51	KP
6861.10	Sm II		57		
6862.82	Sm II	0.88	57	-1.96	KP
7039.225	Sm II	0.99	95	-1.49	KP
042.24	Sm II	1.070	91	-1.42	KP
7051.52	Sm II	0.920	76	-1.56	KP
6645.127	Eu II		159		
7030.33	Hf II		190		

References

Abia, C., Boffin, H.M.J., Isern, J., Rebolo, R. 1993, A&A 272, 445

Abt, H. 1993 (private communication)

Adelman, J., Philip, A.G.D. 1994, MNRAS 269, 579

Albizkij, W.A. 1947, Publ. Crimean AstroPhys. Obs., 1, 20

Bakker E.J 1995, Thesis, University Utrecht, The Netherlands

Barbuy, B., De Medeiros, J.R., Maeder, A. 1996, A&A 305, 911

Baschek, B., Schulz, M., Sedlmayr, E. 1977, A&A 55, 375

Bard A., Kock, M., & Kock, M. 1991, A&A 248, 315

Barlow, M.J. 1983, IAU Symp. 103, 105

Bedijn, P.J. 1987, A&Ap 186, 136

Bell, R.A., Gustafsson, B. 1978, A&AS 34, 229

Bidelman, W.P. 1951, ApJ 113, 304

Bidelman, W.P. 1993, in "Luminous High-Latitude Stars", ASP Conference
    Series 45, ed. D.D. Sasselov, p. 49

Biemont, E., Grevesse, N., Hauge, Ø. 1979, Solar Physics 61, 17

Biemont, E., Grevesse, N., Hannaford, P., Lowe, R.M. 1981, ApJ 248, 867

Biemont, E., Karner, C., Meyer, G., Traeger, F., Zuputlitz, G. 1982, A&A 107, 166

Biemont, E., Grevesse, N., Hannaford, P., Lowe, R.M. 1989, A&A 222, 307

Biemont, E., Baudoux, M., Kurucz, R.L., Ansbacher, W., Pinnington, E.H. 1991,
    A&A 249, 539

Biemont, E., quinet, P., Zeippen, C.J. 1993, A&AS 102, 435

Blöcker, T., Schönberner, D. 1991, A&A 244, L43

Blöcker T. 1995, A&A 299, 755

Bond, H.E., Philip, A. 1973, PASP 85, 332

148

Bond, H.E., Luck, R.E. 1987, ApJ 312, 203

Bond, H.E. 1991,in "The evolution of stars: photospheric abundance connection",
    IAU Symp. 145, ed. G. Michaud and A. Tutokov, p. 341

Boothroyd, A.I., Sackmann, I -J.,Wasserburg, G.J. 1995, ApJ. Letts 442, 21

Bord, D.J., Barisciano, L.P., Jr. Cowley, C.R. 1996, MNRAS 278, 997

Boyarchuk A.A., Lyubmikov L.S., Sakhibullin N.A 1985, Astrophysics 22, 203

Bujarrabal, V., Alcolea, J., Planesas, P. 1992, A&A 257, 701

Burstein D. and Heiles C. 1982, AJ 87, 1172

Buscombe, W. 1984 in " MK spectral Classification Catalogue " North Western Univ.

Cameron, A.G.W. 1955, ApJ 121, 144

Cameron, A. G. W., Fowler, W.F. 1971, ApJ 164, 111

Cardelli J.A., Clayton G.C. and Mathis J.s. 1989, ApJ 345,245

Castelli, F., Hack, M. 1990, Mem. S. A. It. 61, 595

Chiosi, C. 1992, Ann.Rev. Astron. Astrophys. 30, 235

Conlon, E.S., Dufton, P.L., Keenan, F.P., Mc Causland, R.J.H. 1991, MNRAS 248,
    820

Corbally, C.J., and Gray, R.O. 1992 in " Peculiar Versus Normal Phenomena
    in A-type and Related Stars", IAU Coll., N0. 138, ed. F. Castelli
    and M.M. Dworetsky, p. 432

Draine, B.T., Lee, H.M. 1984, ApJ 285, 89

Drake, J.J., Smith, V.V., Suntzeff, N.B. 1994, ApJ 430, 610

Eder, J., Lewis, B.M., Terzian, Y. 1988, ApJS 66, 183

Eggen, O.J. 1969, PASP 81, 553

Eggen, O.J. 1974, PASP 86, 162

Eggen, O.J. 1977, ApJ 215, 812

Feltz,K. 1972, PASP 84, 497

Ferrow, A.A., Mendoza, V.E.E. 1993, AJ 106, 2516

Field, G.B. 1974, ApJ 187, 453

Flower, J.J. 1977, A&A 54, 31

Fuhr, J.R., Martin, G.A., & Wiese, W.L. 1988, J.Phys. Chem. Ref.Data, 17, No.4

Fuhrmann, K., Axer, M., Gehren, T. 1995, A&A 301, 492

Garcia-Laria P., Manchado A., Pottasch S.R., Suso J. and Olling R. 1990, A&A. Suppl. Ser. 82, 497

Garcia-Laria, P., Parthasarathy, M. 1996, in preparation

Geballe T.R. and van der Veen W.E.c.J. 1990, A&A 235, L9

Geballe T.R., Tielens A.G.G.M., Kwok S. and Hrivnak B.J. 1992, ApJ.Letts 387,89

Gilroy, K.K. 1989, ApJ 347, 835

Glaspey, W.J. 1982, ApJ 258, L71

Gonzalez, G., Wallerstein, G. 1992, MNRAS 254, 343

Gratton, R.G. 1990, Mem. S. A. It. 61, 647

Gustaffsson B., Bell R.A., Eriksson K., Nordlund A 1975, A&A 42, 407

Habing H.J., van der Veen W.E.C.J. and Geballe T. 1987, in: Late stages of Stellar evolution, eds. S. Kwok and S.R. Pottasch, Dordrecht, Reidel Publ., p. 91

Habing H.J., 1990, in " From Miras to Planetary Nebulae", eds. M.O. Mennessier and A. Omont, Editions Frontiers, p. 16

Heise, C., Kock, M. 1990, A&A 230, 244

Hannaford, E., Whaling, W. 1982, ApJ 261, 736

Hardie, R.H. 1962, In " Astronomical Techniques", ed. W.A. Hiltner

Chicago: Univ. of Chicago press, Chapter 8. Hawkins, G.W., Skinner, C.J., Meixner,

M.M., Jernigan, J.G., Arens, J.F., Keto, E.,

Graham, J.R. 1995, ApJ 452, 314

Hibbert, A., Biemont, E., Godefroid, M., Vaeck, N. 1991, A&AS 88, 505

Hibbert, A., Biemont, E., Godefroid, M., Vaeck, N. 1993, A&AS 99, 179

Hilderbrand, R.H. 1983, QJRAS 24, 267

Hollowell, D 1987 in " Late Stages of Stellar Evolution", Reidel, Dordrecht, P. 239

Hollowell, D., Iben, I. Jr. 1988, ApJ. Letts. 333, L25

Holweger, H., Heise, C., Kock, M. 1990, A&A 232, 510

Holweger, H., Bard, A., Kock, A., & Kock, M. 1991, A&A 249, 545

Hrivnk B.J., Kwok S., Volk K.M., 1988, ApJ 331, 832

Hrivnak B.J., Kwok S., Volk K.M., 1989, ApJ 346, 265

Hrivnak B.J. and Kwok S. 1991, ApJ 368, 564

Hrivnak B.J., Kwok S. and Geballe T.R. 1994, ApJ 420, 783

Hrivnak B.J. 1995, ApJ 438, 341

Hu J.Y., Bibo E. 1990, A&A 234, 435

Hu J.Y., Slijkuis S., De Jong T. and Jiang B.W. 1993a, A&AS 100,413

Hu J.Y., Slijkuis S., Ngugen-Q-Reiu and de Jong T. 1993b, A&A 273,185

Iben, I.Jr. 1965, ApJ 141, 993

Iben, I. Jr., Renzini, A. 1982. ApJ. Letts. 263, L188

Iben, I. Jr. 1983, ApJ. Letts. 275, L65

Iben, I. Jr., Renzini, A. 1983, Annv. Rev. Astron. Astrophys. 21, 271

Iben, I. Jr., Renzini, A. 1984, Phys. Rep. 105, 329

Iben, I. Jr. 1991, ApJS 76, 55

Iyengar, K.V.K. 1986, A&A 158, 89

Jacoby G.H., Hunter D.A., Christian C.A. 1984, ApJS 56, 257

Jenkins, E.B. 1989, in " Interstellar Dust " , IAU Symp. 135,
    eds. Allamandola and Tielens, p.23

Johnson,H.R., Milkey, R.W., Ramsey, L.W. 1974, ApJ 187, 147

Jones J.B., Wyse R.F.G. and Gilmore G. 1995, PASP 107, 632

Jura, M. 1986, ApJ 309, 732

Justtanont, K., Barlow, M.J., Skinner, C.J., Tielens, A.G.G.M. 1992
    ApJ.Letts 392, 75

Kastner, J.H., Weintraub, D.A. 1995, ApJ 452, 833

Kipper, T., Kipper M. 1993, A&A 276, 389

Kipper, T., Jørgensen, U.G. 1994, A&A 290, 148

Kipper T., Jørgensen U.G., Klochkova V.G., Panchuk V. E. 1996, A&A 306, 489

Klochkova, V.G., Panchuk, V.E. 1987, Sov. Astron. 31 (1)

Klochkova, V.G. 1995, MNRAS 272, 710

Knapp, G.R., Phillips, T.G., Leifgton, R.B., Lo, K.Y., Wannier, P.G., Wootten, H.A.,
    Huggins, P.J. 1982, ApJ 252, 616

Knapp, G.R. 1991, in "Frontiers of Stellar Evolution"., ASP Conference Series, 20,
    P. 229

Kodaira, K. 1973, A&A 22, 273

Kurucz, L.R., Peytremann, E. 1975, SAO Spec.Rep. No. 362

Kurucz, L.R. 1979, ApJS 40, 1

Kurucz, L.R. 1987, in " The Second Conference on Fain Blue stars", IAU Coll. 95,
P. 129 ed. A.G. Davis Philip, D.S. Hayes, J.W. Liebert and L. Davis

Kurucz, L.R. 1988, in " Transations of the International Astronomical Union" , XXB,
p. 168 ed. M. McNally., Dordrecht: Kluwer.

Kwok S., Volk K.M. and Hrivnak B.J. 1989, ApJ 345, L51

Kwok, S. 1993, Ann. Rev. Astron. Astrophys. 31, 63

Kwok, S., Hrivnak, B.J., Geballe, T.R. 1995, ApJ 454, 394

Lambert, D.L., Ries, L.M. 1981, ApJ 248, 228

Lambert, D.L., Roby, S.W., Bell, R.A. 1982, ApJ 254, 664

Lambert, D.L. 1991, in "Evolution of stars: the Photospheric
Abundance Connection" IAU symposium 145, eds. G. Michaud and
A.V. Tutukov, Kluwer, Dordrecht, P.4

Lambert, D.L., McWilliam, A., Smith, V.V. 1992, ApJ 386, 685

Lambert, D.L., Smith, V.V., Heath, J. 1993, PASP 105, 568

Lamers, H.J.G.L.M., Water, L.B.F.M., Garmany, C.D., Perez, M.R. and Waelkens,
C. 1986, A&A 154, L20

Landolt, 1983, ApJ 88, 439

Landolt and Börstein 1982, " Numerical data and fundamental relationships in science
and technology" ., Vol. 2 Astronomy and Astrophysics., ed. Schaifers K
and Voigt H.H

Langer, G.E., Kraft, R.P. 1984, PASP 96, 339

Lattanzio, J.C. 1989, ApJ 344, L25

Lattanzio, J.C. 1992, Proc. Astron. Soc. Aust. 10, 120

Lattanzio, J.C. 1993, IAU Symposium 155 on "Planetary Nebulae", P. 235, edited by
R. Weinberger and A.Acker

Lattanzio, et al 1996, IAU Symposium 177 on " The Carbon Star Phenomenon"
edited by R. Wing (in press)

Lester,J.B., Gray, R.O., Kurucz, R.L. 1986, ApJS 61, 509

Likkel, L., Omont, A., Morris, M., Forveille, T. 1987, A&A 173 , L11

Likkel L., Morris M., Omont R., Forveille T. 1987, A&A 173, 11

Likkel, L. 1989, ApJ 344, 350

Likkel L., Forveille T., Omont A. and Morris M. 1991, A&A 246, 153

Loup, C., Forveille, T., Omont, A., Paul, J.F. 1993,A&AS 99, 291

Luck, R.E., Lambert, D.L., Bond, H.E. 1983, PASP 95, 413

Luck, R.E., Bond, H.E. 1984, ApJ 279, 729

Luck, R.E., Lambert, D.L. 1985, ApJ 298, 782

Luck, R.E., Bond, H.E. 1989, ApJ 342, 476

Luck, R.E., Bond, H.E., Lambert, D.L. 1990, ApJ 357, 188

Luck, R.E., Bond, H.E., Lambert, D.L. 1990, ApJ 357, 188

Luck, R.E. 1993 in " Luminous High-Latitude Stars", ASP Conference Series 45, ed.
D.D. Sasselov, p. 87

Malaney, R.A. 1987, Astrophysics and Space Science 137, 251

Manchado A., Pottasch S.R., Garcia-Lario P., Esteban C. and Mampaso A. 1989,
A&A 214, 139

Mc Causland, R.J.H., Conlon, E.S., Dufton, P.L., Keenan, F.P. 1992, ApJ 394, 298

Martin, G.A., Fuhr, J.R., Wiese, W.L. 1988, J. Phys. Chem. Ref. Data, 17 (S3), 1

Mathis, J.S., Lamers, H.J.G.L.M. 1992, A&A 259, L39

Mayya Y.D, 1991, JAA 12, 319

McCausland, R.J.H., Conlon, E.S., Dufton, P.L., Keenan, F.P. 1992, ApJ 394, 298

McCarthy, J.K., Sandiford, B.A., Boyd, D., Booth, J. 1993, PASP 105, 881

Mendoza,E.E.V. 1989, AJ 97, 1147

Mowlavi, N., 1995, In Proc. ESO/EIPC Workshop " The Light elements
Abundances " Springer, P. 297

Nassau J.J., Stephonson C.B., MacConnell D.J 1965, " Luminous stars in the Milky
Way VI (Hamburg: Hamburg Sternwarte and Warner and Swasey observatory)

Neckel Th. and Klare G. 1980, A&AS 42, 251

Nercessian, E., Omont, A., Benayoun, J.J., Guilloteau, S. 1989, A&A 210, 225

Ney, E.P., Merrill, K.M., Becklin, E.E., Neugebauer, G., Wynn-Williams, C.G. 1975,
ApJ. Letts 198, 129

Nyman L.A., Booth R.S., Carlstrom U., Habing H.J., Heske A., Sahai R., Stark R.,
van der Veen W.E.C.J. and Winnberg A. 1992, A&AS 93, 121

O'Brian, T.R., Wickloffe, M.E., Lawler, J.E., Whaling, W., Brault, J.W. 1991, J. Opt. Soc. Am. B. 8, 1185

Odenwald, S.F. 1986, ApJ 307, 711

Omont A., Loup C., Forveille T., Te Lintel Hekkert P., Habing H and Sivagnanam P. 1993, A&A 267, 515

Oudmaijer, R.D., van der Veen, W.E.C.J., Waters, L.R.F.M., Trams, N.R., Waelkens, C., Engelsman, E. 1992, A&AS 96, 625

Parthasarathy, M., Pottasch, S.R. 1986, A&A 154, L16

Parthasarathy M. and Pottasch S.R. 1988, A&A 192, 182

Parthasarathy M. and Pottasch S.R. 1989, A&A 225, 521

Parthasarathy, M., Garcia Lario, P., Pottasch, S.R. 1992, A&A 264, 159

Parthasarathy, M. 1993, ApJ. Letts 414, 109

Parthasarathy, M. 1993, in " Luminous High Latitude Stars ", ASP Conf. Ser 45, on P. 173, ed. D. Sasselov

Parthasarathy, M. 1994 in " The MK Process at 50 years", ASP Conference Series 60, ed., C.J. Corbally, R.O. Gray, and R.F. Garrision, p. 261

Perinotto, M, 1989, IAU Symp. No 131 Planetary Nebulae, ed. S. Torres-Peimbert, Reidel, Dordrecht, p. 293

Pottasch, S.R., Baud, B., Beintema, D., Emerson, J., Habing, H.J., et al 1984, A&A 138, 10

Pottasch S.R. 1987,in" Planetary Nebulae", Dordrecht, reidel Publ. P. 1

Pottasch, S.R., Parthasarathy M. 1988, A&A 192, 182

Pottasch, S.R., Olling, R., Bignell, C., Zijlstra, A.A. 1988, A&A 205, 248

Pottasch, S.R., Ratag, M.A., Olling, R. 1990, in " From Miras to Planetary Nebulae", eds. M.O. Mennessier and A. Omont, Editions Frontiers, P. 381

Preite-Martinez A. 1988, A&AS 76, 317

Preston, G.W., Krzeminski, W., Smak, J., Williams, J.A. 1963, ApJ 137, 401

Ratag, M.A., Pottasch. S.R. 1991, A&AS 91, 481

Reddy B.E., Parthasarathy M. 1996, AJ, (in press)

Reddy B.E., Parthasarathy, M., Sivarani, T. 1996, A&A, (in press)

Reimers, D. 1975, in " Problems in Stellar Atmospheres and Envelopes ",

Ed. B. Baschek., W.H. Kegel., G. Traving; Springer, Berlin, p. 229

Relyea, L.J., Kurucz, L.R.1978, ApJS 37, 45

Renzini, A. 1981, in " physical processes in Red Giants", ed. I. Iben Jr., A. Renzini, p. 165 Dordrecht: Reidel

Sackmann I.-J., Boothroyd A.I. 1992, ApJ. Letts. 392, 71

Sasselov, D.D. 1984, Ap. Space Sci 102, 161

Scalo, J.M., Despain, K.H., Ulrich, R.K. 1975, ApJ 196, 805

Schönberner D. 1983, ApJ 272, 708

Schönberber, D. 1990, in " From Miras to Planetary Nebulae", eds. M.O. Mennessier and A. Omont, Editions Frontiers, p. 355

Sedlmayr. E. 1994, in " Molecules in the stellar environment", ed. U.G. Jorgensen, Springer, Berline p. 163

Smith, V.V., Lambert, D.L. 1989, ApJ. Letts. 345, 75

Smith, V.V., Lambert, D.L. 1990, ApJS. 72, 387

Sneden,C. 1973, Ph.D. thesis, University of Texas

Sneden, C., Pilachowski, C.A., VandenBerg, D.A. 1986, ApJ 311, 826

Sneden, C., Parthasarathy, M. 1983, ApJ 267, 757

Spite, M., Spite, F. 1982, A&A 115, 357

Sorvari, J.M. 1974, AJ 79, 1416

Stetson, P.B. 1991, AJ 102, 589

Sun J. and Kwok S, 1987, A&A 185, 258

Takeda, Y. 1994, PASJ 46, 53

te Lintel Hekkert, p., Caswell, J.L., Habing, H.J., Haynes, R.F., Norris, R.P. 1991, A&AS 90, 327

Thevenin, F. 1989, A&AS 77, 137

Thevenin, F. 1990, A&AS 82, 179

Torres Dodgen Ana.A. and Weaver Wm.B. 1993, PASP 105, 693

Torres C.A.O., Quast, G., De La Reza, R., Gregorio-Hetem, J., Lepine, J.R.D. 1995, AJ 109, 2146

Trams, N.R., Waters, L.B.F.M., Waelkens, C., Lamers, H.J.G.L.M., Geballe, T.R., The, P.S. 1991 A&AS 87, 361

Van De Steene G.C.M. and Pottasch S.R. 1993, A&A 274, 895

van der Veen W.E.C.J. and Habing H.J, 1988, A&A 194, 125

van der Veen W.E.C.J., Habing H.J., Geballe T.R, 1989, A&A 226, 108

van der Veen, W.E.C.J., Waters, L.B.F.M., Trams, N.R., Matthews, H.E. 1994, A&A
    285, 551

Van Winckel, H., Mathis, J.S., Waelkens, C. 1992, Nature 356, 500

Van Winckel, H., Waelkens, C., Waters, L.B.F.M. 1995, A&A 293, L25

Van Winckel, H. 1995, Phd. Thesis, Katholieke Universiteit Leuven, Belgium

Van Winckel, H., Waelkens, C., Waters, L.B.F.M. 1996, A&A 306, L37

Venn, K.A., Lambert, D.A. 1990, ApJ 363, 234

Volk, K., Kwok, S. 1987, ApJ 315, 654

Waelkens, C., Engelsman, E., Waters, L.B.F.M., van der Veen, W.E.C.J. 1989 in
    " From Miras tp planetary nebulae: which path for stellar evolution ?",
    eds. M.O. Mennessier, A. Omont, Edition Frontiers, P. 470

Waelkens C., Waters L.B.F.M., Cassatella A., Le Bertre T. and Lamers H.J.G.L.M.
    1987, A&A 181, L5

Waelkens, C., Van Winkel H., Bogaert E., Trams N.R.1991, A&A 251, 495

Waelkens, C., Van Winckel H., Bogaert E., Trams N.R. 1992,A&A 264, 159

Wahlgren, G.M. 1993, in " Luminous High-Latitude Stars" ASP Conference Series,
    45, .D. Sasselov (ed), P. 270

Ward, L.1985, MNRAS 213, 71

Westbrook, W.E, et al., 1975, ApJ 202, 407

Waters, L.B.F.M., Trams, N.R., Waelkens, C. 1992, A&A 262, L37

Wheeler, J.C., Sneden, C., Truran, J.W. 1989, Ann. Rev. Astron. Astrophy. 27, 279

Wood P.R., Zaro D.M. 1981, ApJ 247, 247

Woodsworth A.W., Kwok s. and Chen S.J. 1990, A&A 228, 503

Wilson, R.E. 1953, General Catalogue of Stellar Radial Velocities Washing ton.D.C.:
    Carnegie Institution), Carnegie Inst. Washington Pub.

Young, R.K. 1942, Publ. David Dunlap Obs., 1, 251 346, 265.

Zuckerman, B., Dyck, H.M. 1986, ApJ 311, 345

List of Publications

1. Reddy. B.E, Parthasarathy. M and Sivarani. T, 1996 A&A. (in press)
   "HD 105262: a high galactic latitude post-AGB A supergiant with large proper motion"

2. Reddy. B.E, Parthasarathy.M, 1996, AJ (in press)
   "CCD photometry and spectroscopy of IRAS sources with colours similar to planetary nebulae"

3. Reddy, B.E., Parthasarathy, M., Gonzalez, G. 1996, submitted to
   ApJ. Letts.
   "Chemical composition of IRAS 05341+0852 a post-AGB star with 21μm emission"

4. Parthasarathy, M., Garcia-Lario, P., de Martino, D., Pottasch, S.R., Kilkenny, D., Martinez, P., Sahu, K.C., Reddy, B.E., Sewell, B.T. 1995, A&A 300, L25
   " Fading and variations in the spectrum of the central star of the very young planetary nebula SAO 244567 (Hen 1357)"

5. Parthsarathy, M., Reddy, B.E. 1993, Bull. Astro. Soc. India 21, 619
   "Variable supergiants Tw Aql, AI CMi, V 925 Sco and related objcets"

6. Parthsarathy, M., Reddy, B.E. 1993, Bull. Astro. Sco. India 21, 609
   "Post-AGB A-F supergiants"